

Thermally Driven Topology in Chiral Magnets:

Author: Wentao Hou

Persistent link: <http://hdl.handle.net/2345/bc-ir:108694>

This work is posted on [eScholarship@BC](#),
Boston College University Libraries.

Boston College Electronic Thesis or Dissertation, 2019

Copyright is held by the author, with all rights reserved, unless otherwise noted.

Thermally Driven Topology in Chiral Magnets

Wentao Hou

A dissertation
submitted to the Faculty of
the department of Physics
in partial fulfillment
of the requirements
for the degree of
Doctor of Philosophy

Boston College
Morrissey College of Arts and Sciences
Graduate School

December 2019

Thermally Driven Topology in Chiral Magnets

Wentao Hou

Advisor: Prof. Ziqiang Wang, Advisor: Prof. Jiadong Zang

ABSTRACT

Magnetism is an old field in condensed matter physics, but it is still vibrant and full of excitement. Regardless of deep fundamental physics therein, it also has broad application in engineering technology, modern hard disk drive as an example. Magnetic skyrmion, a vortex-like structure in two-dimensional magnetic systems, has been discovered in various magnetic materials, among which chiral magnets are a family of candidates. The skyrmions are characterized by nonzero topological charges. The vortex-like structure of skyrmions makes skyrmion materials good candidates of new generation of data storage device. So understanding the transport properties of the skyrmion materials is important for the possible application in the future. The Hall effect is a key aspect of electron transports. The topological Hall effect, which is one component in the total Hall effect, only depends on the magnetic structures, and the topological Hall conductivity is proportional to the topological charge. It thus serves as the transport signature of magnetic skyrmions. The major mission of this thesis is to investigate the topological charge distribution in realistic models and uncover the relationship between the existence of skyrmions and other chiral excitations. The organization of the thesis is the following.

The first chapter is the introduction. A historical survey about magnetic skyrmions and chiral magnets is presented firstly. The magnetic skyrmion is identified by the topological charge. Further, the relationship between the topological

hall effect and topological charge is described by the emergent electrodynamics. The importance of the topological charge in chiral magnets is explained in this part.

Following the importance of the topological charge, the investigation of topological charge in two-dimensional chiral magnets is presented in the second chapter. The Monte Carlo simulation is employed to calculate the topological charge on a square lattice. The results show that the nonzero topological charge is not necessarily correlated to the existence of skyrmions in chiral magnets. To understand the numerical results, simple analysis based on the physical picture of a triangle on the square lattice is performed. Then we calculate the topological charge in continuum model of chiral magnets. At the high temperature limit, the numerical results, picture analysis and the analytic result are consistent. Then, in this chapter, there is a description of the recent experimental work on thin film SrRuO_3 which confirmed our theoretical prediction. A discussion on spin chirality, topological charge and Hall conductivity is presented in the end.

However, no experiment on chiral magnets has been on a perfect monolayer system. So we extend the investigation of topological charge into three-dimensional situation. This work is introduced in the third chapter. The Monte Carlo simulation and the analytical calculation are presented firstly. A special issue in three-dimensional chiral magnets is the thickness dependence. The Monte Carlo simulation is used to address this issue. A combination of analytical calculation and physical picture of magnons is used to explain the numerical results well. Similar as the second chapter, the experiment on finite thickness SrRuO_3 is described. Because the effective Dzyaloshinskii–Moriya interaction is due to the interface effect which cannot be used to judge our numerical results based on homogenous chiral magnets.

The Heisenberg interaction in the system described in the previous two chap-

ters is ferromagnetic interaction. More physical results with antiferromagnetic interaction are expected in different magnetic system. In the fourth chapter, a review of the work on a frustrated magnet with hexagonal lattice is introduced. The direction of the DM interaction of the hexagonal lattice is perpendicular to the bonds of nearest magnetic atoms. The topological charge is calculated numerically. A similar thermally driven topology as found in chiral magnets is achieved by investigating the topological charge. Following that, the system with staggered DM interaction is discussed. The study of the topological charge in this system not only gives the evolution of thermally driven topology of the system, but also distinguishes the topological charge and spin chirality based on the antiferromagnetic interaction.

Not only thermally driven topology in chiral magnets but also the driven motion of skyrmions are interesting to us. Inspired by the similarity of the vortex state in the Type-II superconductor and skyrmion crystal phase, we investigate the proximity effect between the skyrmion material and non-centrosymmetric s-wave superconductor. The method is to calculate the effective interaction between the Cooper pairs and skyrmions. A field-theoretical approach is employed to this end.

To my parents

ACKNOWLEDGEMENTS

I would first, and foremost thank to my advisors, Professor Ziqiang Wang and Professor Jiadong Zang. Without the help and support from Professor Ziqiang Wang, this thesis would never have been possible. Being a professor who truly cares about his students, Professor Zang taught me not only how to do the research, but also how to think critically, manage time and make plans. The things I learned from him can make me face future challenges more confidently. I would also like to thank my committee members of thesis defense and proposal, Professor Ying Ran, Professor Fazel Tafti and Professor David Broido of their invaluable comments and guidance.

Also, I would like to thank all past and current members of Professor Jiadong Zang's group for building such a good research environment. I was extremely lucky to spend years of time with such smart, hardworking, helpful, and fun people. I would like to thank Dr. Hang Li, Dr Yizhou Liu, Dr. Alexander Booth, Christopher Libby, Domenico Andreoli Jr and Morgan Daly, especially to Dr Jie-Xiang Yu who taught me a lot on the numerical simulations.

I am thankful to Professor Michael Graf, Prof Baldassare Di Bartolo, Professor Gabor Kalman, Professor Kenneth Bruch and Professor Andrzej Herczynski in Boston College. Also, I would like to thank Professor Karsten Phol, Professor Echt Olof, Professor Shawna Hollen and Adam Dukehart in University of New Hampshire for their hospitality.

I would like to thank my colleagues in Boston College, Albert Shi, Shang Gao,

Wenping Cui, Dr. Nakib Protik, Gavin Osterhoudt and Gavin Mayer, with the same year we entered into department of physics in Boston College, and also to Dr Yun Peng, Dr Jiantao Kong, Dr. Kun Jiang, Dr. Mengliang Yao, Dr Bolun Chen, Dr Shenghan Jiang, Dr Aaron Rose, Dr Wuxuan Wu, Tong Yang, Xu Yang, Hung-Yu Yang, Joshua Heath, Mason Gray and Yiping Wang. I am thankful to the services from Jane Carter, Nancy Chevry, Sile Power, Scott Bortolotto in physics department of Boston College, Wei Qiu and Dr. Barry Schaudt for the technique support, and Katie Makem at UNH.

TABLE OF CONTENTS

ACKNOWLEDGEMENTS	vi
LIST OF FIGURES	x
CHAPTER	
I. Introduction	1
1.1 Magnetic skyrmions an topological charge	2
1.2 Skyrmion phases in chiral magnets	4
1.3 Topological Hall effect in chiral magnets	8
II. Topological charge in 2D chiral magnets	12
2.1 Monte Carlo simulation	13
2.1.1 Methodology	13
2.1.2 Results	15
2.2 Analysis on the physical picture of one triangle in the square lattice	19
2.3 The field-theory approach	23
2.3.1 Hamiltonian in the continuum model	23
2.3.2 CP^1 formalism	25
2.3.3 Effective Hamiltonian in CP^1 model	26
2.3.4 Mean field approximation	27
2.3.5 Cut-off Λ and correlation length	30
2.3.6 The effective action of the emergent gauge field	31
2.4 Experimental evidence	39
2.5 Spin chirality, topological charge and Hall resistivity	41
2.6 Conclusion	47
III. Topological charge in 3D chiral magnets	48
3.1 Monte Carlo simulation	48
3.1.1 Methodology	48

3.1.2	Results	49
3.1.3	Finite size scaling	51
3.2	The field theory approach	52
3.2.1	The model and Hamiltonian	53
3.2.2	Mean field approximation	56
3.2.3	Perturbative Calculation	57
3.3	Thickness dependence	63
3.3.1	Mean field approximation	64
3.3.2	Thickness dependence of $\langle b_z \rangle$	65
3.4	Conclusion	66
IV. Topological charge in antiferromagnetic system with different kinds of DM interaction		68
4.1	Topological charge in frustrated magnetic system	69
4.2	Topological charge in antiferromagnets with staggered DM interaction.	73
4.2.1	Model	73
4.2.2	Ground state	75
4.2.3	Spin chirality at high temperature	78
4.2.4	Topological charge in antiferromagnetic square lattice with staggered DM interaction	81
V. Proximity effect between skyrmion material and Type-II superconductor		86
5.1	Model	87
5.2	Effective action and Its Expansion	89
5.2.1	Second Order Calculation of Free Energy	91
5.2.2	The Third Order Calculation	95
5.2.3	The fourth order perturbation	101
5.3	Ginzburg-Landau equations	102
5.4	Discussion	103
VI. Summary and future directions		104
APPENDICES		107

LIST OF FIGURES

Figure

1.1	(a)The stereographic pojection of a hedge spin texture and a Néel type skyrmion. (b) The projection of one spin the spherical hedgehog.	2
1.2	(a) Bloch type magnetic skyrmion. (b)Néel type magnetic skyrmion[23].	3
1.3	The crystallographic structure of MnSi	4
1.4	(a)Phase Diagram of MnSi(Ref[10]). (b)Configuration of SkX phase in real space. (c)The helical, conical, field-polarized spin structures[10].	7
1.5	Phase diagram of $\text{Fe}_{0.5}\text{Co}_{0.5}\text{Si}$. (a)-(c) Magnetic field dependence of Lorentz TEM images. (d) Temperature versus magnetic field phase diagram from experiments. (e)-(g) Magnetic field dependence of numerical snapshots. (h) Temperature versus magnetic field phase diagram from numerical simulationcite[39].	8
1.6	The crystal structure and the phase diagram of Cu_2OSeO_3 [15]. . .	9
2.1	Solid angle of the three nearest spins	14
2.2	(a) $B - T$ diagram of the topological charges in 2D with $D/J = 0.3$. (b)The size dependence of topological charge.	15
2.3	Snapshots and corresponding reciprocal space plots by Fast Fourier Transform (FFT) at points on the $B - T$ diagram of the topological charges shown in top figure. (a) $B = 0.20J$ and $T = 1.02J$, (b) $B = 0.20J$ and $T = 0.80J$, (c) $B = 0.06J$ and $T = 0.02J$, (d) $B = 0.06J$ and $T = 0.66J$, (e) $B = 0.08J$ and $T = 0.02J$ and (f) $B = 0.02J$ and $T = 0.02J$. In real space snapshots, red (blue) contour represent the positive (negative) value of size and the arrows represent the directions of in-plane component. For (c) and (d), the density of the topological charge is also shown at right panel respectively.	17
2.4	(a) The topological charge versus T/J with fixed $D/J = 0.3$. (b) The topological charge versus T/J with fixed $B/J = 0.12$. The lattice size is 60×60 . The two intersecting panels on (a) and (b) shows the relationship of the absolute value of the topological charge $ Q_T $ between magnetic field and DM interaction at $T = 2.0J$.	19

2.5	The sphere figure shows the net the topological charge is zero in absence of magnetic field. The triangle shows the energy degeneracy of the two triangle with opposite spins lifted by the external magnetic field.	20
2.6	Feynman rules and diagrams.	31
2.7	(a) Total Hall resistivity. (b) Anomalous Hall resistivity is subtracted. (c) Topological Hall effect. (d) The relationship between topological resistivity and temperature. Right top is the thickness dependence of the topological Hall resistivity[103].	39
2.8	(a) The thickness dependence of the topological Hall resistivity. (b) The theoretical results of the topological charge.	40
2.9	Left is the 3×3 square lattice. Right shows the periodical boundary condition.	44
2.10	The relationship between Hall resistivity, topological charge and spin chirality, (a) low field, (b) high field.	46
3.1	Triangulation of the cubic lattice	50
3.2	(a) Q_T vs T/J , fixed $B/J = 0.2$.(b) Q_T vs T/J , fixed $D/J = 0.3$	51
3.3	Topological charge versus T/J	52
3.4	(a) Specific heat c_v versus T/J . (b) Average Topological charge versus T/J	53
3.5	Rescaling specific heat $c_v L_z^{-\frac{\zeta}{\nu}}$ versus $[(T - T_c)L_z^{1/\nu} + T_c]$ (b) Average Topological charge versus $[(T - T_c)L_z^{1/\nu} + T_c]$	54
3.6	Feynman rules and Feynman diagrams	57
3.7	(a) The relationship between $\langle b_z \rangle$ and T/J . (b)The relationship between $\langle b_z \rangle$ and T/J	66
4.1	(a)Top view and side view of the Top view and side view for the crystal structure of a 2D hexagonal lattice with A and B sublattices. (b)The relationship between topological charge density and temperature with $D = 0.40J$, $K_u = 0.20J$ and $B = 0.40J$	69
4.2	Relationship between topological charge, and DM interaction as well as external magnetic field.	71
4.3	Relationship between topological charge and uniaxial magnetic anisotropy.	72
4.4	(a)The unit cell and primitive vectors. (b)The smallest cell of staggered DM situation.	74
4.5	The topological charge of antiferromagnetic system with staggered DM interaction	82
4.6	(a) Three spins on one triangle.(b)The projection fo the three spins on the shpere.(c)The value of solid angle Ω_Δ by Berg formula.	83
4.7	$B - T$ diagram of topological charge in staggered DM system.	84
4.8	Snapshots of spin textures(a) $T = 0.0176J$. (b) $T = 0.1998J$.(c) $T = 0.3947J$.(d) $T = 0.5912J$.(e) $T = 0.7845J$.(f) $T = 0.9998J$. And $D = 0.2J, B = 0.1J$	85

CHAPTER I

Introduction

Geometry is a mature tool describing the physical world. From the vector representation of force and to curvature description of gravity, the applications of geometry in physics have been successful. Topology, a branch in geometry which studies the geometric properties and spatial structures invariant under the continuous change, has recently become popular in the research of condensed matter physics. Many novel phenomena and elegant theories relevant to topology appeared, such as Berry phase[1], quantum Hall effect(QHE)[2] topological insulator[3, 4] and anomalous Hall effect(AHE)[5]. Magnetism is a long living field in condensed matter physics. In magnetic systems, there are a few topology related structures, such as magnetic monopole[6], magnetic vortex[7], magnetic domain wall[8] and magnetic skyrmions[9, 10]. Topology does not only make physicists understand the universe well, but also motives the revolution of techniques. Magnetic skyrmion is a good example of the application on a topological object in physics to electric engineering. The magnetic skyrmion materials are predicted as good candidates for constructing the next generation data storage devices[11].

Skyrmion, firstly proposed by Tony Skyrme[12] in 1960s, was used to explain the stability of the hadrons from the view of the topological defects in three dimensional(3D) non-linear sigma model. Magnetic skyrmions, as the topologi-

cal defects, have been found in various magnetic materials, such as chiral magnets[10, 13, 14, 15] which are non-centrosymmetric, the centrosymmetric magnets with easy-axis anisotropy[8, 16, 17, 18, 19, 20], and the interface of ferromagnets with automatic breaking of spatial inversion symmetry[21, 22]. The magnetic skyrmion, which has a vortex-like spin texture gives nontrivial topological structure comparing to the common ordered spin textures such as ferromagnetic and antiferromagnetic phases.

1.1 Magnetic skyrmions and topological charge

The magnetic skyrmion is a vortex-like magnetic structure in a two-dimensional (2D) plane. The spin structure of magnetic skyrmions can be viewed as a stereographic projection from a spherical hedgehog onto a 2D plane. The spins locating on the spherical surface of the hedgehog are pointing radially away from the center of the sphere, which is described as $\mathbf{n}(\mathbf{r}) = \hat{r}$. As Figure 1.1(b) shows, the south pole of the sphere sits on the origin of the 2D plane. The north pole is mapped to point at the infinity. Any other spin on the sphere is projected at the intersecting point of the connecting line between north pole and the point on the sphere onto the 2D plane by a straight line that goes through the north pole. A Néel type skyrmion is achieved by this projection. If

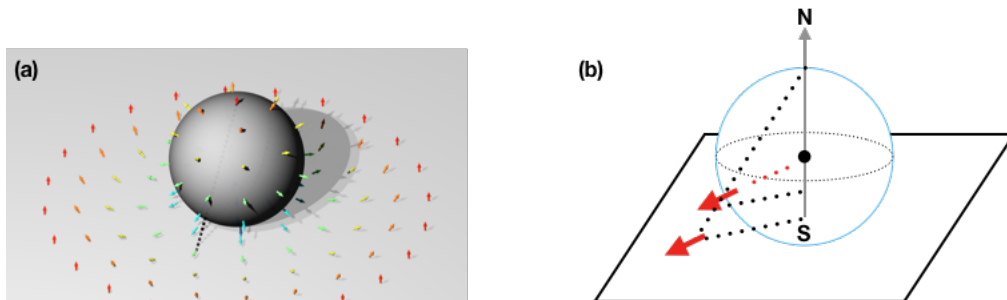


Figure 1.1: (a) The stereographic projection of a hedge spin texture and a Néel type skyrmion. (b) The projection of one spin the spherical hedgehog.

all the spins of a Néel type skyrmion are rotated around the axis perpendicular to the plane by 90° at the same direction, a Bloch type skyrmion is achieved. The magnetic structures of Néel type skyrmion and Bloch type skyrmion are shown in Figure 2. The spins at the edge of the skyrmions are upward and spins at core are

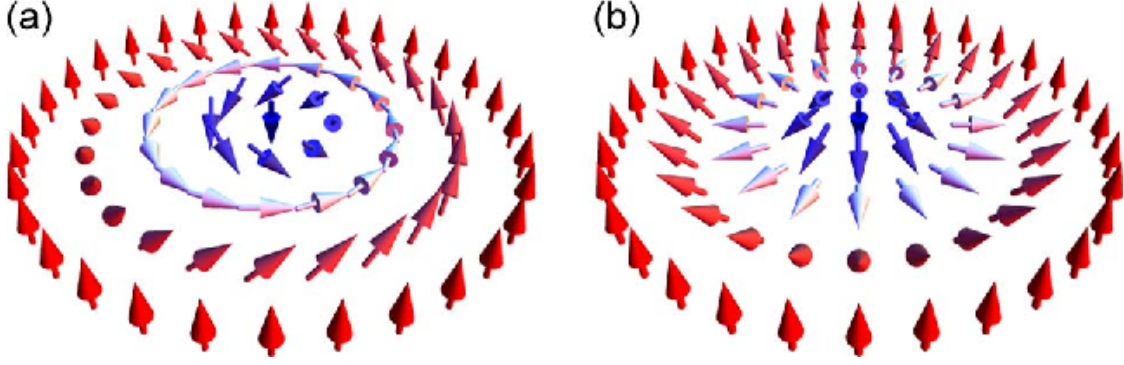


Figure 1.2: (a) Bloch type magnetic skyrmion. (b) Néel type magnetic skyrmion[23].

downward. The spins between edge and core vary gradually. If the radius of the sphere is R , from the stereographic projection, the spin configuration of the Néel type skyrmion can be parameterized as[24]

$$\mathbf{n}_{Néel} = \left(\frac{2Rx}{r^2 + R^2}, \frac{2Ry}{r^2 + R^2}, \frac{r^2 - R^2}{r^2 + R^2} \right), \quad (1.1)$$

where $r^2 = x^2 + y^2$. The spin configuration of Bloch type skyrmion is

$$\mathbf{n}_{Bloch} = \left(-\frac{2Ry}{r^2 + R^2}, \frac{2Rx}{r^2 + R^2}, \frac{r^2 - R^2}{r^2 + R^2} \right). \quad (1.2)$$

As mentioned in last paragraph, the two kinds of skyrmions can exchange to each other by rotation which means they are topologically identical. The topological charge is the winding number of the spins on the sphere. It is defined as

$$Q = \frac{1}{4\pi} \int d^2r \mathbf{n} \cdot (\partial_x \mathbf{n} \times \partial_y \mathbf{n}), \quad (1.3)$$

where $\mathbf{n} = \mathbf{n}(\mathbf{r})$ is the normalized local magnetization.

To skyrmions, The non-zero value of the topological charge is used to point out the skyrmions when $Q = 1$ means the magnetization at skyrmion core is upward ($+z$ direction) and $Q = -1$ means downward ($-z$ direction). More generally, the nontrivial topology in the magnetic system is identified by the non-zero value of the topological charge.

1.2 Skyrmion phases in chiral magnets

The magnetic skyrmions are observed in many various magnetic materials with distinctive properties. The chiral magnet is typically one of them. The crystal structures of chiral magnetic materials are non-centrosymmetric, such as B20 compounds(MnSi[10, 25, 26, 27, 28], FeGe[29], MnGe[13, 30, 31],etc.). Here, using MnSi as an example, the crystal structure is shown in Figure 1.3. If an inversion operation is performed on this crystal structure, the positions of Manganese atoms and Silicon atoms will be exchanged. The structure is no longer the same. This kind of crystallographic structures lacks an inversion center.

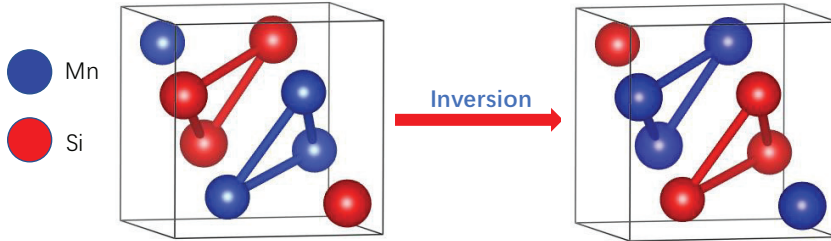


Figure 1.3: The crystallographic structure of MnSi

The study of the chiral magnets can be traced back to 1970s. Neutron scattering experiments identified the helical spin structures in non-centrosymmetric metallic ferromagnets such as MnSi[10] and FeGe[29]. In year 1980, Bak and Jensen[32] constructed a theoretical description of the chiral magnets based on

the Ginzburg-Landau theory. In their works, the Dzyaloshinskii-Moriya(DM) interaction plays a crucial role to understand the helical spin structures in non-centrosymmetric magnets. This antisymmetric interaction is expressed as

$$H_{DM} = \sum_{\langle ij \rangle} \mathbf{D}_{ij} \cdot (\mathbf{S}_i \times \mathbf{S}_j), \quad (1.4)$$

in a discrete spin model, where $\langle ij \rangle$ means nearest neighbor. The vector \mathbf{D}_{ij} has $\mathbf{D}_{ij} = -\mathbf{D}_{ji}$ and $|\mathbf{D}_{ij}|$ is finite. The DM interaction is achieved by Dzyaloshinskii[33] through a phenomenal model and by Moriya[34] through a microscopic model. The microscopic mechanism of DM interaction is based on the spin-orbit coupling. From Eqn.(1.4), H_{DM} gets its minimum requires \mathbf{S}_i is perpendicular to \mathbf{S}_j . In no non-centrosymmetric metallic ferromagnets, there is Heisenberg interaction between nearest spins,

$$H_J = -J \sum_{\langle ij \rangle} \mathbf{S}_i \cdot \mathbf{S}_j, \quad (1.5)$$

where $J > 0$. H_J gets its minimum requires the nearest spins should be parallel to each other. The competition between Heisenberg interaction and DM interaction leads the helical magnetic ground state. In Bak and Jensen's work, they employed the continuum model for the chiral magnets. By minimizing the energy, they achieved the general solution of the ground state,

$$\mathbf{S}(\mathbf{r}) = \frac{1}{\sqrt{2}} [\mathbf{S}_q \exp(i\mathbf{q} \cdot \mathbf{r}) + \mathbf{S}_{-q}^* \exp(-i\mathbf{q} \cdot \mathbf{r})], \quad (1.6)$$

which is just the helical state. The \mathbf{q} , the magnetic modulation vector, is determined by the Heisenberg interaction, the DM interaction and the anisotropy in the system. Then Bogdanov and his collaborators[35] extended the theoretical description of chiral magnetism by introducing the Zeeman coupling which is between

the local magnetization and the external magnetic field. A saddle-point solution with a vortex-like magnetic structure was found, which is the magnetic skyrmion. Moreover, inspired by the formation of Abrikosov vortex lattice in Type-II superconductor, they predicted there would be a skyrmion crystal structure with a triangular arrangement at a certain temperature and external magnetic field region.

On the other hand, there was a curious phase in MnSi which locates just below the Curie temperature. For a long time, it was called A-phase. The letter A means anomalous[36, 37, 38], because at that early time, the phase could not be understood completely. Through small angle neutron scattering experiments done on the bulk MnSi, Pfleiderer's group discovered the skyrmion configuration and finally identified the A phase as the skyrmion crystal phase(SkX)[10]. The phase diagram is shown in Figure 1.4(a). The spin configuration in real space is shown in Figure 1.4(b). Figure 1.4(c) shows the helical, conical and field-polarized spin structure from left to right, \mathbf{q} is the magnetic modulation vector parallel to the external magnetic field \mathbf{H} . M is the component of spin parallel to the external magnetic field \mathbf{H} . M_0 is the module of spins.

Meanwhile, an experiment from Tokura's group on the thin-film of chiral magnetic $\text{Fe}_{1-x}\text{Co}_x\text{Si}$ [39] revealed the skyrmion phases at a broad range of the temperature extending almost zero. In this work, a Monte Carlo simulation was employed to accomplish explaining the experimental results. The phase diagrams(in Figure 1.4) from both experiment and numerical simulation show there is mixture between skyrmion and other magnetic phases, the helical and ferromagnetic phases. The skyrmion phases can be stabilized in the thin-film system makes the thin-film chiral magnets as a good candidate to test the quantum transport properties, like anomalous Hall effect(AHE), excepted for 2D SkX state.

In the year 2012, the magnetic phase diagram of chiral magnet Cu_2OSeO_3 has

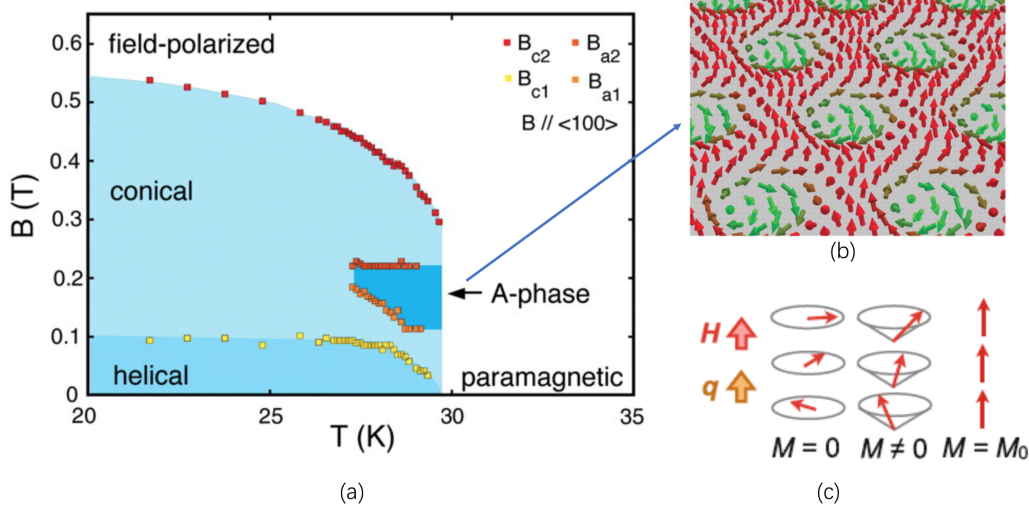


Figure 1.4: (a)Phase Diagram of MnSi(Ref[10]). (b)Configuration of SkX phase in real space. (c)The helical, conical, field-polarized spin structures[10].

been investigated by Tokura's group[15]. The space group of the crystal structure is $P2_13$ which is as the same as B20 compounds. The crystal structure is in Figure 5 and the phase diagram. The crystal structure of Cu_2OSeO_3 shares the same space group as B20 compounds, but it is an insulator, unlike the B20 compounds. Without the itinerant electrons, there is no charge carrier. Only the thermal carriers, such as magnons and phonons contribute to thermal conductivity. The magnon hall effect is proposed in this kind of systems[40, 41, 42, 43]. This material is a good candidate to study how the chiral magnetism affects the thermal conductivity because there is no interruption from the conduction electrons. Also, Cu_2OSeO_3 is ferrimagnetic material[44, 45] which may has broad application on techniques and engineerings. Several chiral magnets which host the skyrmion textures have been listed in Table 1.1.

The skyrmions with zero-field[46, 47, 48] and room temperatures[49, 50] are more likely to be applied to the data storage devices and logic gates[51, 52, 53, 54, 55, 56, 57, 58]. Many other magnetic systems, such as the magnetic thin films[59, 60, 61, 62, 63, 64, 65, 66, 67, 68, 69] and artificial magnetic structures[70, 71, 72,

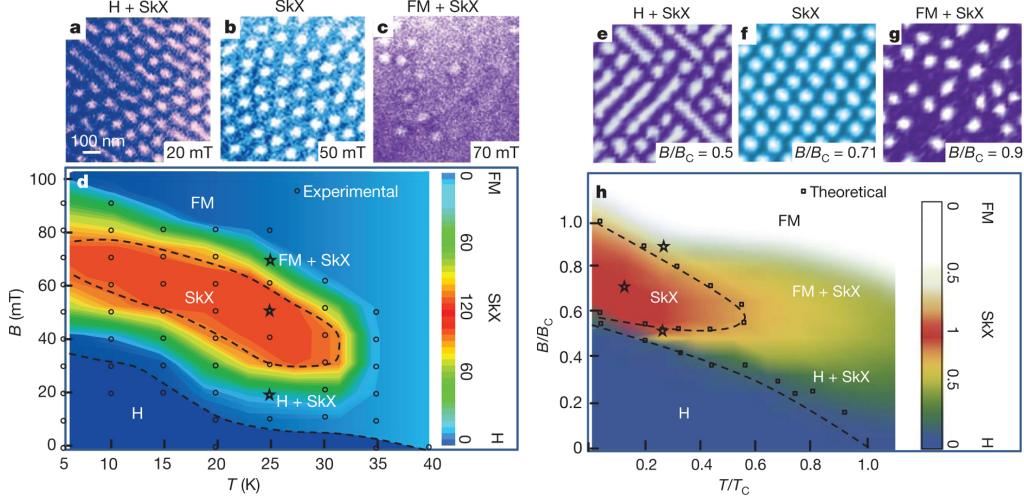


Figure 1.5: Phase diagram of $\text{Fe}_{0.5}\text{Co}_{0.5}\text{Si}$. (a)-(c) Magnetic field dependence of Lorentz TEM images. (d) Temperature versus magnetic field phase diagram from experiments. (e)-(g) Magnetic field dependence of numerical snapshots. (h) Temperature versus magnetic field phase diagram from numerical simulationcite[39].

Material	$T_C(K)$	$\lambda_m(nm)$	Conductivity	Ref.
MnSi	30	18	Metal	[10, 25, 26, 27, 28]
$\text{Fe}_{1-x}\text{Co}_x\text{Si}$	36	40~250	Semiconductor	[39]
MnGe	170	3	Metal	[13, 30, 31]
FeGe	278	70	Metal	[29]
Cu_2OSeO_3	59	62	Insulator	[15, 44]

Table 1.1: The chiral magnets which host the skyrmion structure.

73, 74, 75, 76]. So understanding the transport properties of skyrmion materials is important to the future possible usages in engineering.

1.3 Topological Hall effect in chiral magnets

Understanding the transport properties of the chiral magnets is an important aspect for the future applications. Topological Hall effect (THE)[77, 78, 79, 80, 81, 82, 83, 84] would occur in some magnetic metals when there are the non-coplanar spin textures. THE can be simply described as non-coplanar spin textures acts on the electrons an effective magnetic field and deflects the electron sided away. It is

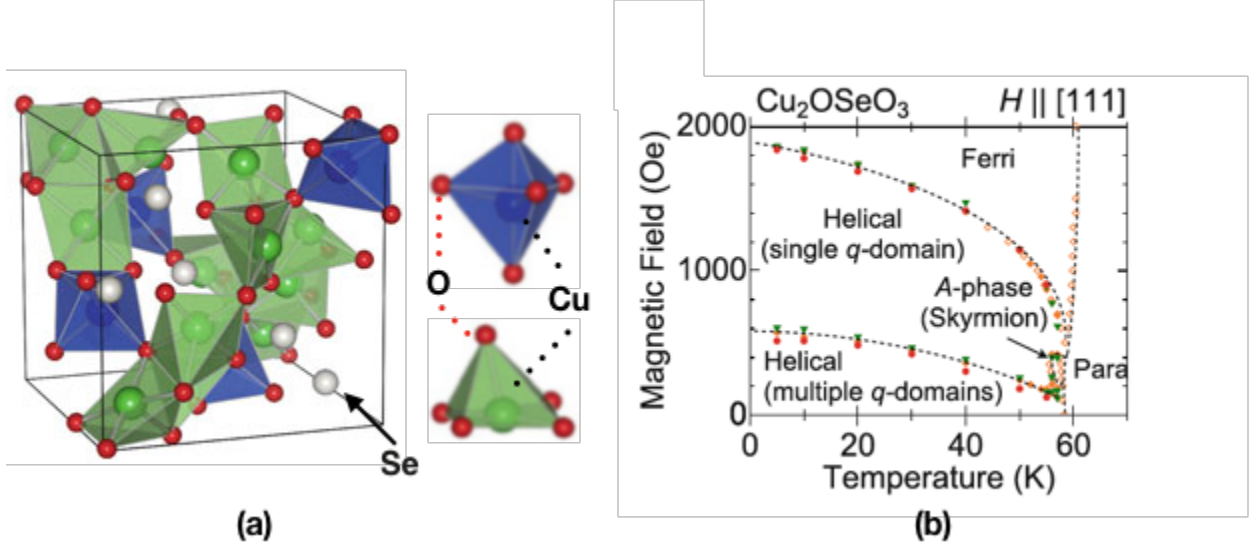


Figure 1.6: The crystal structure and the phase diagram of Cu_2OSeO_3 [15].

distinguished with the ordinary Hall effect(OHE)[85], which requires the external magnetic field and anomalous Hall effect(AHE)[5, 86], which has been discovered in uniform magnetic structure. The mechanism of THE can be explained by the emergent electrodynamics[87, 88, 89, 90, 91].

The Hamiltonian of the conductive electrons in a magnetic system is

$$\hat{H} = \frac{1}{2m}(-i\hbar\nabla)^2 - J_H\mathbf{M} \cdot \hat{\sigma}, \quad (1.7)$$

where m is the effective mass of the electrons, J_H is Hund's coupling and $\mathbf{M} = \mathbf{M}(\mathbf{r})$ is the local magnetization. The normalized magnetization is

$$\mathbf{n}(\mathbf{r}) = \frac{\mathbf{M}(\mathbf{r})}{|\mathbf{M}(\mathbf{r})|}, \quad (1.8)$$

and $M = |\mathbf{M}(\mathbf{r})|$. If the Hund's coupling J_H is strong enough, the motion of electrons can be treated adiabatically, which means the spins of electrons will be parallel to the local magnetization at each point of the space. The spin eigenstates will be $\mathbf{n} \cdot \hat{\sigma}|n\rangle = |n\rangle$. Defining the projection operator $\hat{P} = |n\rangle\langle n|$, the effective

Hamiltonian which makes a rotation in the Hilbert space to make the Hund's coupling term simply,

$$\hat{H}_{eff} = \hat{P}\hat{H}\hat{P} = \frac{1}{2m}(-i\hbar\nabla - \frac{e}{c}\mathbf{a})^2 - J_H\mathbf{M}, \quad (1.9)$$

where $\mathbf{a} = \frac{i\hbar c}{2e}\langle n|\nabla|n\rangle$ is the emergent gauge field. In 2D, $\nabla = (\partial_x, \partial_y, 0)$, the corresponding effective magnetic field[92] is

$$\mathbf{b} = \nabla \times \mathbf{a} = \frac{i\hbar c}{2e}\hat{\mathbf{n}} \cdot (\partial_x\mathbf{n} \times \partial_y\mathbf{n}). \quad (1.10)$$

where the effective magnetic field is perpendicular to plane. $\mathbf{n} \cdot (\partial_x\mathbf{n} \times \partial_y\mathbf{n})$ has appeared in the definition of the topological charge. So this effect depends on the topology of the spin textures. The magnetic flux of the emergent field is

$$\Phi = \int b_z dA = \frac{\hbar c}{e}Q \quad (1.11)$$

which corresponds to the topological charge. In the square lattice, $\mathbf{n} \cdot (\partial_x\mathbf{n} \times \partial_y\mathbf{n})$ can be approximated as $\mathbf{n}_i \cdot (\mathbf{n}_{i+\hat{x}} \times \mathbf{n}_{i+\hat{y}})$ which is the mixing product of three nearest spins. It is also called spin chirality.

The Hall resistivity is

$$\rho_{xy} = R_o H + R_s M + \rho_{xy}^{THE}, \quad (1.12)$$

where R_o is the OHE coefficient, R_s is the conventional AHE coefficient and ρ_{xy}^{THE} is the contribution from THE. The contribution of the AHE is mainly from the Berry phase of electrons in momentum phase[93, 94, 95], skew scattering[96, 97, 98] and side jump effect[99, 100, 101]. Studying the topological charge or spin chirality is directly relevant to Hall effect of chiral magnets. Another question

needs to be answered is does nonzero topological charge correspond the existence of skyrmions in chiral magnets. The importance of the topological charge to the Hall effect and the relationship with the existence of skyrmions motivate us to investigate how it evolves thermally. We performed both numerical and analytical method to calculate the thermal average of the topological charge in 2D chiral magnetic system[102] which will be presented in Chapter 2. We found the nonzero topological charge exists even above the Curie temperature at which the spin textures are disordered. Experiments have been done to measure the signal of THE on thin film magnetic metals SrRuO_3 and V-doped Sb_2Te_3 [103]. The THE signals are significant above the Curie temperature which means the topological charge or the spin chirality is nonzero above the Curie temperature. The results from the experiments confirmed our theoretical prediction in the 2D thin film. Our investigation of the topological charge goes to the 3D chiral magnets because all the experiments have been mentioned above were performed on the thin films with finite thicknesses or in bulk samples. No sample can be treated as a perfect 2D system[10, 39, 15]. The calculation of the topological charge in 3D is presented in Chapter 3 with a discussion of the thickness dependence. Then in Chapter 4, the systems with antiferromagnetic Heisenberg interaction are discussed. Motivating by the similarity of the vortices in Type-II superconductor and magnetic skyrmion, we study the proximity effect of Type-II superconductor and skyrmion material by a field-theoretical calculation. It will be presented in Chapter 5.

CHAPTER II

Topological charge in 2D chiral magnets

The $B - T$ phase diagrams of several chiral magnetic materials have been studied experimentally[10, 15] and theoretically[39]. In the skyrmion crystal phase(SkX), the topological charge is identical to the skyrmion number. The definition of the topological charge in Eqn.(1.1) respects the rotational symmetry so that it is not proper to be selected as the order parameter. But the topological charge of magnetic systems is directly relevant to the transport properties. Therefore, it is interesting to study how the topological charge distributes in the $B - T$ diagram. The theoretical study of the topological charge in 2D chiral magnets will be elaborated in this chapter. This chapter is organized as following. The first section is about the Monte Carlo simulation of the topological charge in 2D chiral magnets. For the purpose to understand the numerical results well, an analysis on a three-spin picture is performed in the second section. In third section, a field-theoretical method is employed to calculate the topological charge in 2D chiral magnets. Then there is a comparison and discussion of the numerical and analytical results at the end this chapter.

2.1 Monte Carlo simulation

2.1.1 Methodology

The Monte Carlo simulation is performed on a 2D square lattice of classical spin model. The Hamiltonian of the chiral magnet with external magnetic field is

$$H = \sum_{\langle lm \rangle} (-J \mathbf{S}_l \cdot \mathbf{S}_m + \mathbf{D}_{lm} \cdot \mathbf{S}_l \times \mathbf{S}_m) - g\mu_B H \sum_l S_l^z, \quad (2.1)$$

where $\mathbf{S}_l = S\mathbf{n}_l$ is the spin vector on site l and $|\mathbf{n}_l| = \frac{|\mathbf{S}_l|}{S} = 1$. $\langle lm \rangle$ means site l and m are the nearest neighbors. In this model, the 2D square lattice lays on the $x - y$ plane, and the external magnetic field is perpendicular to this plane, along z direction. The first term is Heisenberg interaction, $J > 0$ for ferromagnetic exchange coupling. The second term is the DM interaction term. In this square lattice, $\mathbf{D}_{l,l+\hat{x}} = D\hat{x}$ and $\mathbf{D}_{l,l+\hat{y}} = D\hat{y}$. $|\mathbf{D}_{lm}| = D$ is the amplitude of DM interaction. The last term is the Zeeman coupling term, μ_B is the magnetic momentum. For simplicity, $g\mu_B H$ is defined as B and we choose the natural units ($k_B = \hbar = c = 1$).

To calculate the thermal average of the topological charge, the square lattice need to be triangulated. Summation over all the solid angle Ω of three spins on each triangle divided by 4π gives the total the topological charge for each spin configuration. The solid angle Ω can be achieved by a projecting method as Figure 2.1 shows.

After moving the ends of the three normalized spin vectors without changing the directions the at a same point, the solid angle Ω can be easily achieved from the area they surround on the sphere. The solid angle Ω is calculated by the Berg

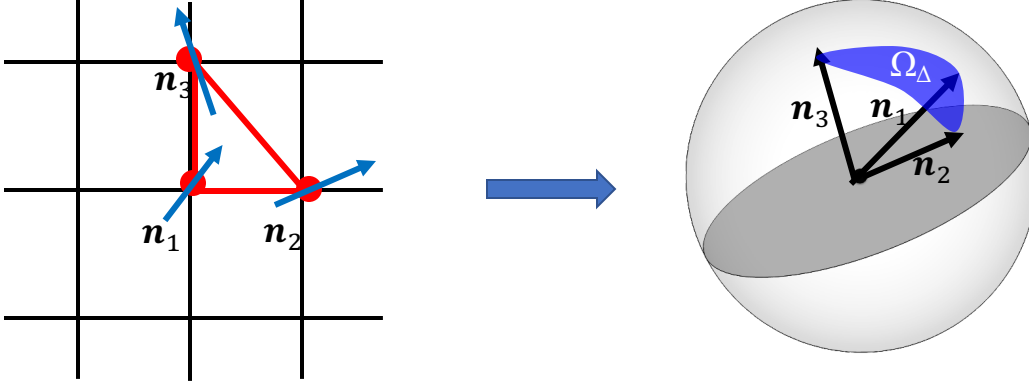


Figure 2.1: Solid angle of the three nearest spins

formula[104]:

$$\exp\left(\frac{i\Omega}{2}\right) = \rho^{-1}[1 + \mathbf{n}_1 \cdot \mathbf{n}_2 + \mathbf{n}_2 \cdot \mathbf{n}_3 + \mathbf{n}_3 \cdot \mathbf{n}_1 + i\mathbf{n}_1 \cdot (\mathbf{n}_2 \times \mathbf{n}_3)], \quad (2.2)$$

$$\rho = 2[(1 + \mathbf{n}_1 \cdot \mathbf{n}_2)(1 + \mathbf{n}_2 \cdot \mathbf{n}_3)(1 + \mathbf{n}_3 \cdot \mathbf{n}_1)]^{\frac{1}{2}}. \quad (2.3)$$

where \mathbf{n}_1 , \mathbf{n}_2 and \mathbf{n}_3 are the three spins on triangle. The Metropolis and over-relaxation algorithm are employed iteratively to generate a Markov chain of spin configurations[105], averaging over which thermal average of the topological charge was derived. The procedure of Metropolis algorithm is

1. It starts from an an arbitrary spin lattice.
2. After flipping one spin on the lattice, The new energy H_{new} is compared to H_{old} . If $\delta H = H_{new} < H_{old}$, the change is accepted.
3. Otherwise, the random number $z(0 < z < 1)$ is generated to compare with the probability $p = \exp(-\frac{\delta H}{T})$ where T is the temperature. If $p > z$, the change is accepted.

By repeating the steps above, the most probable spin lattice is achieved at the given temperature T . We imposed periodic boundary conditions and performed

average over 2.4×10^6 ensembles at each temperature. Also, the lattices with different sizes have been employed to study the size dependence issue.

2.1.2 Results

The results are shown in Figure 2.2. Figure 2.2(a) shows the color plot of the

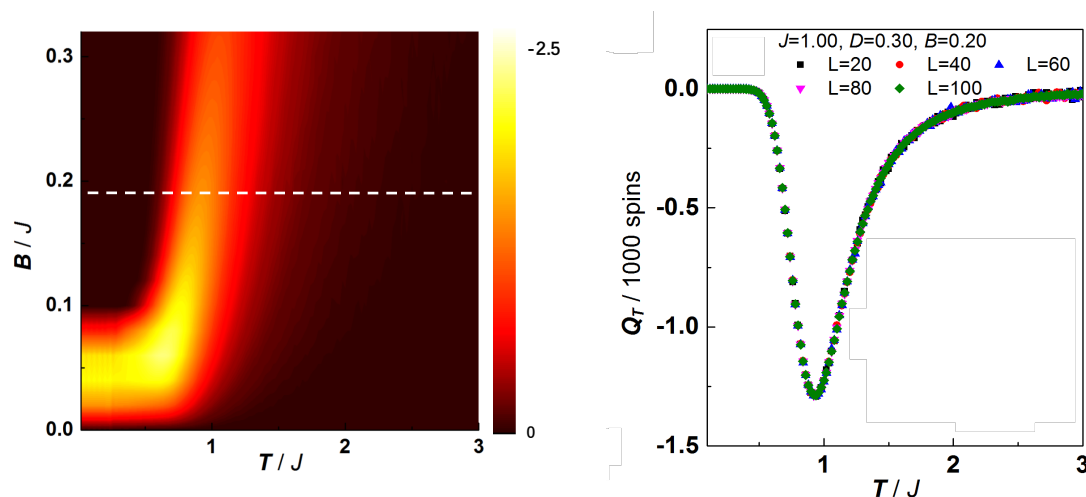


Figure 2.2: (a) $B - T$ diagram of the topological charges in 2D with $D/J = 0.3$. (b) The size dependence of topological charge.

average the topological charge in the $B - T$ diagram with the fixed DM interaction as $D/J = 0.3$. A dramatic upturn of the the topological charge is addressed along a ridge in the $B - T$ diagram. The value of the the topological charge is significant in areas greatly extended to the skyrmion phase, which is located at small B and low T in the bottom region of the ridge. Special attention need to be paid to the high field region, where is no skrymion excepted. As a typical example, we fix $B/J = 0.2$ to study the relationship between value of average the topological charge and the temperature T/J , which is shown in Figure 2.2(b). At very low temperature, the topological charge is equal to zero, as all spins are nearly polarized. At very high temperature, the topological charge converges to zero due to the topological triviality of a completely random phase. In between,

the topological charge becomes significantly elevated at finite temperatures. A deep dip of the the topological charge is witnessed around $T/J = 1.0$, the Cuire temperature of the corresponding Heisenberg model. The negative of the topological charge is consistent with the fact that spin at the skrymion core is opposite to the external magnetic field. The same calculations were performed for lattices with sizes varying from 20×20 to 100×100 . No difference could be found between different lattice sizes. This immunity to the nite size effect suggests robustness of the the topological charge upturn, which might be related to the scaling-free atomic scale physics.

This emergent topology at finite temperatures does not correspond to any ordered phase such as the skyrmion crystal phase (SkX) or meron-helix composite. The snapshots at several unique points with different temperatures and fields have been taken to look into the spin textures in different situations. For the purpose to show the corresponding points of the snapshots in the $B - T$ diagram of the topological charges(Figure 2.2(a)), the $B - T$ diagram of the topological charges is put at the top of Figure 2.3. Below the $B - T$ diagram of the topological charges are the snapshots from the different temperatures and fields.

Two snapshots of spin states around the ridge were taken, as shown in .3(a) and (b). Location of their corresponding parameters are labeled by the same letter in the B-T diagram on the top. At point A to the right of the ridge, $B = 0.2J$ and $T = 1.02J$, and the total the topological charge is about -12 in a 100×100 lattice. However, the real space image shown in Figure 2.3(a) is completely random. Fast Fourier transformation(FFT) of the image provides only one peak at Γ point in the reciprocal space. This indicates the uniform randomness and absence of any spin ordering at this point. For point B to the left, where the temperature $T = 0.8J$ is relatively lower, the corresponding real space snapshot in Figure 2.3(b) shows similar randomness with a single peak at the Γ point of the reciprocal space.

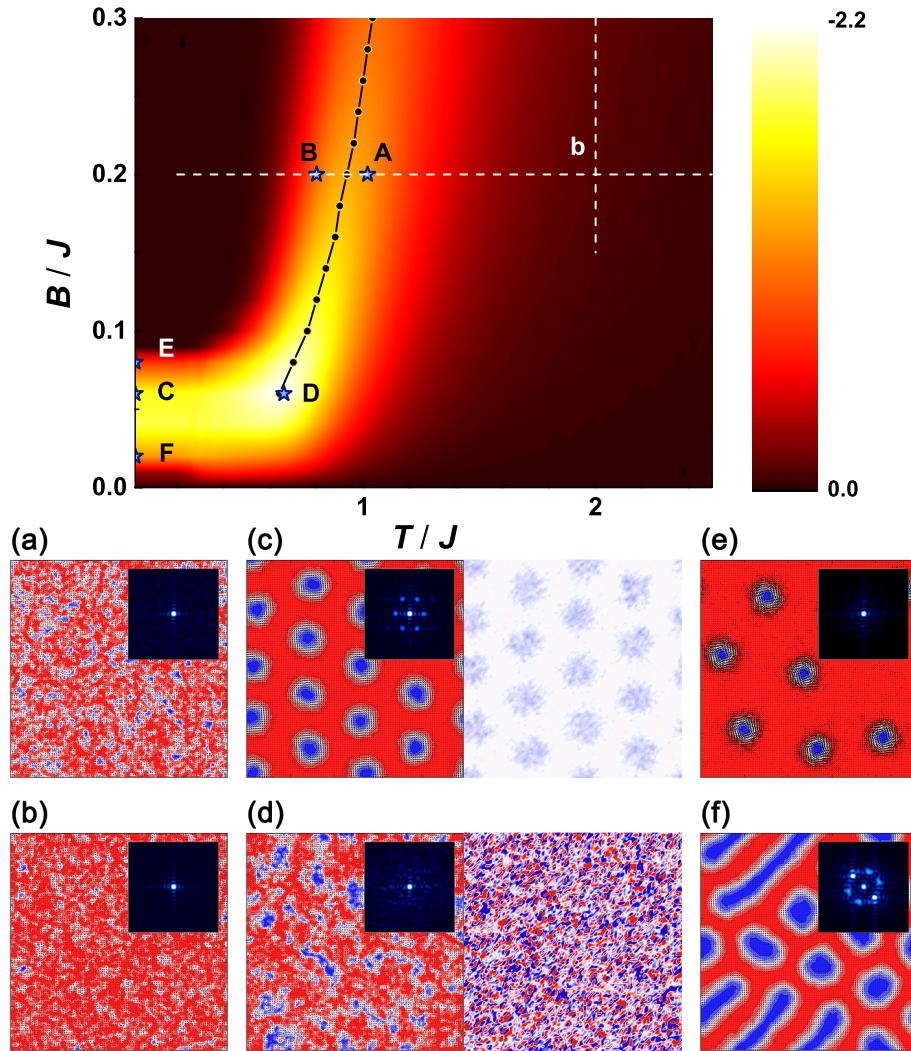


Figure 2.3: Snapshots and corresponding reciprocal space plots by Fast Fourier Transform (FFT) at points on the $B - T$ diagram of the topological charges shown in top figure. (a) $B = 0.20J$ and $T = 1.02J$, (b) $B = 0.20J$ and $T = 0.80J$, (c) $B = 0.06J$ and $T = 0.02J$, (d) $B = 0.06J$ and $T = 0.66J$, (e) $B = 0.08J$ and $T = 0.02J$ and (f) $B = 0.02J$ and $T = 0.02J$. In real space snapshots, red (blue) contour represent the positive (negative) value of size and the arrows represent the directions of in-plane component. For (c) and (d), the density of the topological charge is also shown at right panel respectively.

Compared to point A, a higher spin polarization parallel with the field is achieved here. From zero temperature to points A or B of interest, no phase transition occurs. The emergence of the topological charge is thus purely a consequence of the thermal fluctuation.

In contrast, the topological charges at low field, especially at low temperatures, have distinct origin. The Monte Carlo simulation shows that the the topological charge grows significantly around $T = 0.25J$ during the annealing procedure and remains stable to zero temperature. It is attributed to the formation of the skyrmion crystal phase. A typical snapshot was taken at point C with $B = 0.06J$ and $T = 0.02J$. The real space image shows a well aligned skyrmion lattice, and the reciprocal space shows the hexagonal pattern as expected. At the same field, if the temperature is elevated to point D, the snapshot in Figure 2.3(d) does not present any ordering, although the the topological charge remains significant. Densities of the topological charge for C and D points are plotted in Figure 2.3(c) and Figure 2.3(d) for comparison. Nonzero topological charge emerges only near the skyrmion in the ordered skyrmion phase, while it is evenly distributed in the high temperature state. At a relatively higher field at point E shown in Figure 2.3(e), the skyrmion crystal is melted and sparse skyrmions are observed. While at a lower field at point F, the transition from skyrmion crystal phase to the helical phase takes place, and a meron-helix composite appears at this first order phase transition. In all these regions at low temperatures, the the topological charge is consistent with the number of skyrmions in the lattice. Thermal fluctuation induced the topological charge is suppressed. These low-field and low-temperature results are consistent with previous studies[106, 107].

The dependence of the topological charges on DM interactions and fields are also investigated by the Monte Carlo simulation. The the topological charge versus temperature figures with fixed DM interaction and several values of fields and

the one with fixed magnetic field with several values of DM interactions have been plotted in Figure 2.4. At fixed temperature $T = 2.0J$, curve fittings are

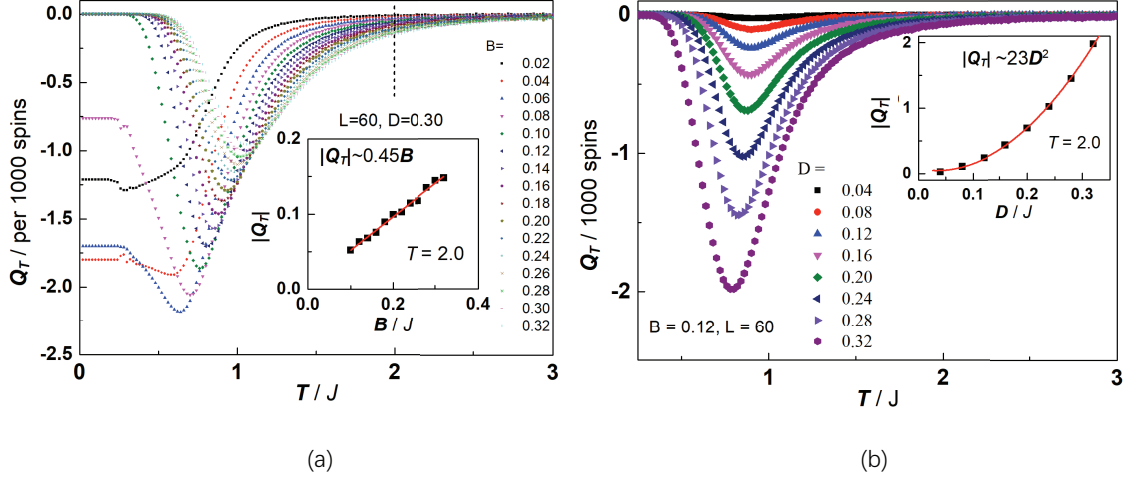


Figure 2.4: (a) The topological charge versus T/J with fixed $D/J = 0.3$. (b) The topological charge versus T/J with fixed $B/J = 0.12$. The lattice size is 60×60 . The two intersecting panels on (a) and (b) shows the relationship of the absolute value of the topological charge $|Q_T|$ between magnetic field and DM interaction at $T = 2.0J$.

applied for the absolute value of the topological charge $|Q_T|$ with fields and DM interaction independently. The results show that at relative high temperature $|Q_T|$ is proportional to the magnetic field with fixed DM interaction. And it is quadratic on the DM interaction with fixed magnetic field.

2.2 Analysis on the physical picture of one triangle in the square lattice

As indicated by its scaling-free property, origin of the thermally driven topology can be understood by a simple physical picture on the atomic scale. As defined earlier, the topological charge is the summation of solid angles of all triangles in the lattice. Due to the presence of the DM interaction, these three spins in each triangle are canted and contribute a solid angle of Ω . If we reverse all three spins,

the new configuration cants an opposite solid angle Ω . In the absence of the field, these two configurations share the same energy, as both the Heisenberg and DM interactions are quadratic spin interactions. These two configurations thus have the same probability of appearance at any temperature, and the average of the topological charge is zero, which can be shown in Figure 2.5(a). However, these two

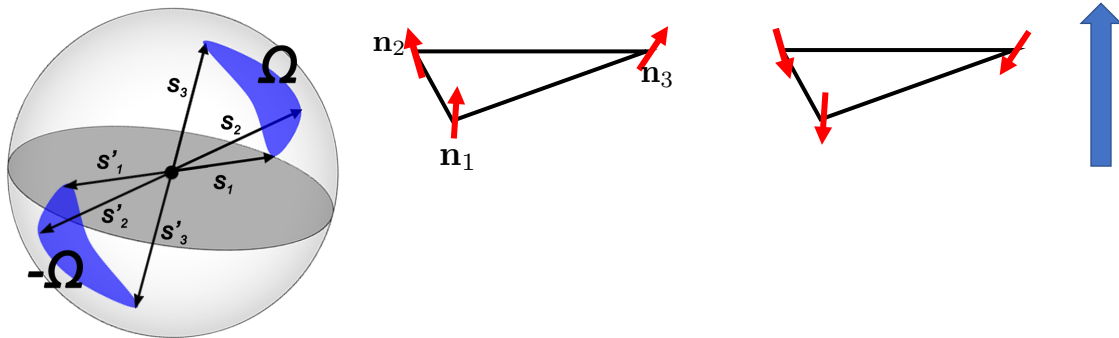


Figure 2.5: The sphere figure shows the net the topological charge is zero in absence of magnetic field. The triangle shows the energy degeneracy of the two triangle with opposite spins lifted by the external magnetic field.

configurations, being time reversal to each other, share opposite magnetizations. An external magnetic field can thus lift the degeneracy and induce a net the topological charge after thermal averaging. One needs to be aware that under large enough field, canting of spin takes place only when the temperature approaches the Curie temperature, far below which the polarized state is robust and the average the topological charge is zero. On the other hand, a very high field, the energy difference induced by the field is no longer relevant, and average the topological charge decays to zero as well.

Quantitatively, one triangle in the square lattice can be employed to explain these relationships. From the lattice shown in Figure 2.1. The spins at the vertices of the selected triangle is $\mathbf{n}_1, \mathbf{n}_2$ and \mathbf{n}_3 . Notice that \mathbf{n}_2 and \mathbf{n}_3 are not the nearest neighbors, so there is no direct interaction between them. By the definition in

Eqn.(1.1), the topological charge of the triangle can be simplified as the solid angle $Q = \mathbf{n}_1 \cdot (\mathbf{n}_2 \times \mathbf{n}_3)$ without the constant $\frac{1}{4\pi}$. The energy of the triangle can be expressed as

$$E = -J(\mathbf{n}_1 \cdot \mathbf{n}_2 + \mathbf{n}_1 \cdot \mathbf{n}_3) - D(n_{1y}n_{2z} - n_{1z}n_{2y} + n_{1z}n_{3x} - n_{1x}n_{3z}) - B(n_{1z} + n_{2z} + n_{3z}). \quad (2.4)$$

The thermal average the topological charge of this triangle is

$$\langle Q \rangle = \frac{1}{\mathcal{Z}} \int \prod_i d\mathbf{n}_i \mathbf{n}_1 \cdot (\mathbf{n}_2 \times \mathbf{n}_3) \exp(-\frac{E}{T}), \quad (2.5)$$

where $\mathcal{Z} = \int \prod_i d\mathbf{n}_i \exp(-\frac{E}{T})$ is the partition function. At the high temperature limit which means $E/T \ll 1$, we can expand the average of topological charge as

$$\langle Q \rangle = \frac{1}{\mathcal{Z}} \int \prod_i d\mathbf{n}_i \mathbf{n}_1 \cdot (\mathbf{n}_2 \times \mathbf{n}_3) [1 - \frac{E}{T} + \frac{1}{2!}(\frac{E}{T})^2 - \frac{1}{3!}(\frac{E}{T})^3 + \mathcal{O}((\frac{E}{T})^4)]. \quad (2.6)$$

\mathbf{n}_i can be parameterized as $\mathbf{n}_i = (\sin \theta_i \cos \phi_i, \sin \theta_i \sin \phi_i, \cos \theta_i)$. The integral $\int \prod_i d\mathbf{n}_i$ is replaced by $\int \prod_i d\Omega_i$ where $\int d\Omega_i = \int_0^{2\pi} d\phi_i \int_0^\pi \sin \theta_i d\theta_i$. It requires the nonzero terms in polynomial expansion in Eqn.(2.6) should include \mathbf{n}_i and their components with even powers. The leading two orders of E/T vanish because one cannot pair up \mathbf{n}_i and their components into even powers. The nonzero contribution emerges at the order of $\frac{1}{T^3}$. They are

$$-\frac{(-D)^2(-B)}{T^3} n_{1y}n_{2z}n_{1z}n_{3x}n_{1z}(n_{1y}n_{2z}n_{3x}) = \frac{D^2B}{T^3} (n_{1y}n_{2z}n_{3x})^2 n_{1z}^2, \quad (2.7)$$

$$-\frac{(-D)^2(-B)}{T^3} n_{1z}n_{2y}n_{3z}n_{1x}n_{1z}(n_{1x}n_{2y}n_{3z}) = \frac{D^2B}{T^3} (n_{1x}n_{2y}n_{3z})^2 n_{1z}^2, \quad (2.8)$$

$$-\frac{(-D)^2(-B)}{T^3} (-n_{1z}n_{2y})n_{1z}n_{3x}n_{1z}(-n_{1z}n_{2y}n_{3x}) = \frac{D^2B}{T^3} (n_{1z}n_{2y}n_{3x})^2 n_{1z}^2. \quad (2.9)$$

The contribution from above all together is proportional to $\frac{D^2B}{T^3}$. Further, the

contribution of the order $\frac{1}{T^4}$ is nonzero. All the terms are listed below:

$$\begin{aligned}
\frac{(-D)^2(-J)(-B)}{T^4}n_{1y}n_{2z}n_{1z}n_{3x}n_{1z}n_{2z}n_{2z}(n_{1y}n_{2z}n_{3x}) &= \frac{D^2JB}{T^4}(n_{1y}n_{2z}n_{3x})^2n_{1z}^2n_{2z}^2, \\
\frac{(-D)^2(-J)(-B)}{T^4}n_{1y}n_{2z}n_{1z}n_{3x}n_{1y}n_{2y}n_{2z}(-n_{1z}n_{2y}n_{3x}) &= -\frac{D^2JB}{T^4}(n_{1z}n_{2y}n_{3x})^2n_{1y}^2n_{2z}^2, \\
\frac{(-D)^2(-J)(-B)}{T^4}n_{1z}n_{2y}n_{3z}n_{1x}n_{1z}n_{3z}n_{1z}(n_{1x}n_{2y}n_{3z}) &= \frac{D^2JB}{T^4}(n_{1x}n_{2y}n_{3z})^2n_{1z}^2n_{3z}^2, \\
\frac{(-D)^2(-J)(-B)}{T^4}n_{1z}n_{2y}n_{3z}n_{1x}n_{1x}n_{3x}n_{3z}(-n_{1z}n_{2y}n_{3x}) &= -\frac{D^2JB}{T^4}(n_{1z}n_{2y}n_{3x})^2n_{1x}^2n_{3z}^2, \\
\frac{(-D)^2(-J)(-B)}{T^4}n_{1y}n_{2z}(-n_{3z}n_{1x})n_{1y}n_{2y}n_{2z}(n_{1x}n_{2y}n_{3z}) &= -\frac{D^2JB}{T^4}(n_{1x}n_{2y}n_{3z})^2n_{1y}^2n_{2z}^2, \\
\frac{(-D)^2(-J)(-B)}{T^4}n_{1y}n_{2z}(-n_{3z}n_{1x})n_{1x}n_{3x}n_{3z}(n_{1y}n_{2z}n_{3x}) &= -\frac{D^2JB}{T^4}(n_{1y}n_{2z}n_{3x})^2n_{3z}^2n_{1x}^2, \\
\frac{(-D)^2(-J)(-B)}{T^4}n_{1y}n_{2z}(-n_{3z}n_{1x})n_{1y}n_{2y}n_{2z}(n_{1x}n_{2y}n_{3z}) &= -\frac{D^2JB}{T^4}(n_{1x}n_{2y}n_{3z})^2n_{1y}^2n_{2z}^2, \\
\frac{(-D)^2(-J)(-B)}{T^4}n_{1y}n_{2z}(-n_{3z}n_{1x})n_{1x}n_{3x}n_{3z}(n_{1y}n_{2z}n_{3x}) &= -\frac{D^2JB}{T^4}(n_{1y}n_{2z}n_{3x})^2n_{3z}^2n_{1x}^2, \\
\frac{(-D)^2(-J)(-B)}{T^4}(-n_{1z}n_{2y})n_{1z}n_{3x}n_{1z}n_{2z}n_{2z}(-n_{1z}n_{2y}n_{3x}) &= \frac{D^2JB}{T^4}(n_{1z}n_{2y}n_{3x})^2n_{1z}^2n_{2z}^2, \\
\frac{(-D)^2(-J)(-B)}{T^4}(-n_{1z}n_{2y})n_{1z}n_{3x}n_{1z}n_{3z}n_{3z}(-n_{1z}n_{2y}n_{3x}) &= \frac{D^2JB}{T^4}(n_{1z}n_{2y}n_{3x})^2n_{1z}^2n_{3z}^2, \\
\frac{(-D)^2(-J)(-B)}{T^4}(-n_{1z}n_{2y})n_{1z}n_{3x}n_{1x}n_{3x}n_{3z}(n_{1x}n_{2y}n_{3z}) &= -\frac{D^2JB}{T^4}(n_{1x}n_{2y}n_{3z})^2n_{1z}^2n_{3x}^2, \\
\frac{(-D)^2(-J)(-B)}{T^4}(-n_{1z}n_{2y})n_{1z}n_{3x}n_{1y}n_{2y}n_{2z}(n_{1y}n_{2z}n_{3x}) &= -\frac{D^2JB}{T^4}(n_{1y}n_{2z}n_{3x})^2n_{1z}^2n_{2y}^2.
\end{aligned} \tag{2.10}$$

They have the same absolute value after integration. The contributions to $\langle Q \rangle$ is positive and negative are determined by the sign as Eqn.(2.10) shows. There are 8 “-” and 4 “+” which means the total contribution is negative in contrast of positive contribution at the order $\frac{1}{T^3}$. Moreover, it is proportional to $\frac{D^2BJ}{T^4}$.

The results from the analysis on a triangle is reasonable. the topological charge respects to the spatial inversion symmetry and breaks the time reversal symmetry. Respecting to the spatial inversion symmetry requires the topological charge to be proportional to D squared, which is spatial inversion odd. It can be predicted at higher order, the DM interaction D would emerge with the even order. Breaking

time reversal symmetry leads the linear relationship between the topological charge and B at the nonzero lowest order of $\frac{1}{T}$ because B is time reversal odd. The results are consistent with the curve fitting in Figure 2.4.

2.3 The field-theory approach

The argument in the last section is only based on one triangle. To the many spin system, a continuous field theory can be applied to calculate the average of the topological charge.

2.3.1 Hamiltonian in the continuum model

The energy in Eqn.(2.1) can be expanded to the form, here, for simplicity, the Zeeman coupling part is set to zero,

$$H = -J \sum_{\langle lm \rangle} \mathbf{S}_l \cdot \mathbf{S}_m - D \sum_l [(\mathbf{S}_l \times \mathbf{S}_{l+\hat{x}}) \cdot \hat{x} + (\mathbf{S}_l \times \mathbf{S}_{l+\hat{y}}) \cdot \hat{y}], \quad (2.11)$$

where $\langle lm \rangle$ means the nearest neighbor. In real materials, the ration $\frac{D}{J} < 1$ means the Heisenberg ferromagnetic exchange coupling dominates. The lattice constant a is much shorter than the periodical length of the helical ground state so we can treat this model in continuum limit. $\mathbf{S} = \hbar S \mathbf{n}$, in natural units, $\hbar = 1$.

$$\begin{aligned} \mathbf{S}_l \cdot \mathbf{S}_{l+nearest} &= S^2 + a \hat{r} \mathbf{S}_l \cdot \vec{\nabla} \mathbf{S}_l + \frac{a^2}{2} \mathbf{S}_l \cdot \nabla^2 \mathbf{S}_l + \mathcal{O}(a^3) \\ &= S^2 + \frac{a^2 S^2}{2} \mathbf{n} \cdot \nabla^2 \mathbf{n} + \mathcal{O}(a^4) \end{aligned} \quad (2.12)$$

$$\rightarrow S^2 - \frac{a^2 S^2}{2} (\partial_i \mathbf{n}) \cdot (\partial_i \mathbf{n}) + \mathcal{O}(a^4), \quad (2.13)$$

where $i = x, y$. The odd order of a is zero because of the symmetry in the square lattice system. The DM interaction term can be expanded as

$$\begin{aligned}
(\mathbf{S}_l \times \mathbf{S}_{l+\hat{x}}) \cdot \hat{x} + (\mathbf{S}_l \times \mathbf{S}_{l+\hat{y}}) \cdot \hat{y} &\approx a[(\mathbf{S}_i \times \partial_x \mathbf{S}_i) \cdot \hat{x} + (\mathbf{S}_i \times \partial_y \mathbf{S}_i) \cdot \hat{y}] \\
&= aS^2 \left(\begin{array}{ccc} 1 & 0 & 0 \\ n_x & n_y & n_z \\ \partial_x n_x & \partial_x n_y & \partial_x n_z \end{array} \right) \\
&\quad + \left(\begin{array}{ccc} 0 & 1 & 0 \\ n_x & n_y & n_z \\ \partial_y n_x & \partial_y n_y & \partial_y n_z \end{array} \right) \\
&= aS^2 (n_y \partial_x n_z - n_z \partial_x n_y + n_z \partial_y n_x - n_x \partial_y n_z) \\
&= -aS^2 \mathbf{n} \cdot (\nabla \times \mathbf{n}). \tag{2.14}
\end{aligned}$$

Here, $\nabla = (\partial_x, \partial_y, 0)$. Turning to continuum limit, the summation $\sum_l H_l \rightarrow \frac{1}{a^d} \int d^d r \mathcal{H}$. The Hamiltonian is

$$\begin{aligned}
H &= \frac{1}{a^2} \int d^2 r \left[\frac{JS^2 a^2}{2} (\partial_i \mathbf{n})(\partial_i \mathbf{n}) + DS^2 a \mathbf{n} \cdot (\nabla \times \mathbf{n}) \right] \\
&= \int d^2 r \left[\frac{JS^2}{2} (\partial_i \mathbf{n})(\partial_i \mathbf{n}) + \frac{DS^2}{a} \mathbf{n} \cdot (\nabla \times \mathbf{n}) \right]. \tag{2.15}
\end{aligned}$$

The Zeeman coupling term can be added to the continuum model simply,

$$H_{Zeeman} = \frac{-BS}{a^d} \int d^d r n_z \tag{2.16}$$

So, the Hamiltonian of the continuum model of chiral magnet in 2D is

$$H = \int d^2 r \left[\frac{\bar{J}}{2} (\partial_i \mathbf{n})(\partial_i \mathbf{n}) - \bar{\mathbf{D}} \mathbf{n} \cdot (\nabla \times \mathbf{n}) - \bar{B} n_z \right], \tag{2.17}$$

where $i = x, y$, $\bar{J} = JS^2$, $\bar{D} = \frac{DS}{a}$, $\bar{B} = \frac{BS}{a^2}$ and $\mathbf{n}(\mathbf{r})$ is the normalized spin. Calculating the thermal average of topological charge need to be performed in a statistical physics framework. So,

$$\langle Q \rangle = \frac{1}{\mathcal{Z}} \int \prod_i \mathcal{D}n_i(r) Q \exp\left(-\frac{H}{T}\right) \delta(|\mathbf{n}| - 1) \quad (2.18)$$

where $\mathcal{Z} = \int \prod_i \mathcal{D}n_i(r) \exp\left(-\frac{H}{T}\right) \delta(|\mathbf{n}| - 1)$. It is not easy to do the functional integration over field $\mathbf{n}(\mathbf{r})$ because the Zeeman coupling term is linear. More steps need to be applied to make it Gaussian integrable.

2.3.2 CP^1 formalism

CP^1 formalism[108, 109, 110] is a suitable method for the path integral approach, because the projection

$$\mathbf{n} = \mathbf{z}^\dagger \boldsymbol{\sigma} \mathbf{z} \quad (2.19)$$

makes the Zeeman term bilinear, where $\boldsymbol{\sigma} = (\sigma_x, \sigma_y, \sigma_z)$ is the vector of Pauli matrices. \mathbf{z} is a two component complex spinor which is unimodular $\mathbf{z}^\dagger \mathbf{z} = 1$. The degrees of freedom of spin vector \mathbf{n} are two, because \mathbf{n} has three components which means it has three degrees of freedom and the constraint condition $|\mathbf{n}| = 1$ makes the degrees of freedom subtract one. After CP^1 projection, \mathbf{z} is a two component complex spinor, the degrees of freedom is four, also with the condition $|\mathbf{z}| = 1$, the final degrees of freedom is three. That means there is one residue degree of freedom after CP^1 projection. To spinor, the chosen of \mathbf{z} is arbitrary in some sense. If $\mathbf{z} \rightarrow e^{i\theta(\mathbf{r})} \mathbf{z}$, the spin \mathbf{n} is invariant. The residue degree of freedom corresponds to a local gauge symmetry.

2.3.3 Effective Hamiltonian in CP^1 model

The density of the Hamiltonian is

$$\mathcal{H} = 2\bar{J}(\partial_i \mathbf{z})^\dagger (\partial_i \mathbf{z}) - 4\bar{J}A_i^2 - 2\bar{D}\mathbf{n} \cdot \mathbf{A} - i\bar{D}\mathbf{z}^\dagger (\boldsymbol{\sigma} \cdot \mathbf{A})\mathbf{z} + i\bar{D}(\nabla \mathbf{z}^\dagger) \cdot \boldsymbol{\sigma} \mathbf{z} - \bar{B}\mathbf{z}^\dagger \sigma_z \mathbf{z} \quad (2.20)$$

where $A_i = -\frac{i}{2}[\mathbf{z}^\dagger (\partial_i \mathbf{z}) - (\partial_i \mathbf{z})^\dagger \mathbf{z}]$. We perform the Hubbard-Stratonovich[111, 112, 113] to decouple the quartic terms of field \mathbf{z} . In CP^1 representation, the partition function is

$$\mathcal{Z} = \int \prod_{i=1,2} \mathcal{D}a_i \mathcal{D}\mathbf{z}^\dagger \mathcal{D}\mathbf{z} \exp\left\{-\frac{1}{T} \int d^2r [2\bar{J}|(\partial_i - ia_i + i\kappa\sigma_i)\mathbf{z}|^2 - \bar{B}\mathbf{z}^\dagger \sigma_z \mathbf{z}]\right\} \delta(\mathbf{z}^\dagger \mathbf{z} - 1)\} \quad (2.21)$$

where \mathbf{a} is the emergent $U(1)$ gauge and $\kappa = \frac{\bar{D}}{2\bar{J}}$. We can transform the partition function with quadratic terms of a_i ,

$$\begin{aligned} \mathcal{Z} &= \int \mathcal{D}a_i \mathcal{D}\mathbf{z}^\dagger \mathcal{D}\mathbf{z} \\ &\times \exp\left\{-\frac{1}{T} \int d^2r [2\bar{J}(a_i - A_i - \kappa\mathbf{z}^\dagger \sigma_i \mathbf{z})^2 + 4\bar{J}\kappa^2 - \bar{B}\mathbf{z}^\dagger \sigma_z \mathbf{z} - 2\bar{D}\mathbf{z}^\dagger \sigma_i \mathbf{z} A_i \right. \\ &\left. + 2\bar{J}[(\partial_i \mathbf{z})^\dagger (\partial_i \mathbf{z}) - A_i^2] + i\bar{D}(\partial_i \mathbf{z}^\dagger \sigma_i \mathbf{z} - \mathbf{z}^\dagger \sigma_i \partial_i \mathbf{z})]\right\} \delta(\mathbf{z}^\dagger \mathbf{z} - 1). \end{aligned} \quad (2.22)$$

After integrating the fields a_i out, the partition function is

$$\begin{aligned} \mathcal{Z} &= \mathcal{C} \int \mathcal{D}\mathbf{z}^\dagger \mathcal{D}\mathbf{z} \exp\left\{-\frac{1}{T} \int d^2r [2\bar{J}[(\partial_i \mathbf{z})^\dagger (\partial_i \mathbf{z}) - A_\mu^2 - \bar{B}\mathbf{z}^\dagger \sigma_z \mathbf{z} \right. \\ &\left. + i\bar{D}(\partial_\mu \mathbf{z}^\dagger \sigma_\mu \mathbf{z} - \mathbf{z}^\dagger \sigma_\mu \partial_\mu \mathbf{z}) - 2\bar{D}\mathbf{z}^\dagger \sigma_\mu \mathbf{z} A_\mu + 4\bar{J}\kappa^2]\right\} \delta(\mathbf{z}^\dagger \mathbf{z} - 1) \end{aligned} \quad (2.23)$$

Where \mathcal{C} is a constant from the integral. The effective Hamiltonian is

$$\begin{aligned} H_{eff} &= \int d^2r [2\bar{J}[(\partial_\mu \mathbf{z})^\dagger (\partial_\mu \mathbf{z}) - A_\mu^2] + i\bar{D}(\partial_\mu \mathbf{z}^\dagger \sigma_\mu \mathbf{z} - \mathbf{z}^\dagger \sigma_\mu \partial_\mu \mathbf{z}) \\ &\quad - 2\bar{D}\mathbf{z}^\dagger \sigma_\mu \mathbf{z} A_\mu - \bar{B}\mathbf{z}^\dagger \sigma_z \mathbf{z}] \end{aligned} \quad (2.24)$$

which is as same as Eqn.(2.20). So the effective Hamiltonian in CP^1 model is

$$H = \int d^2r [2J|(\partial_i - ia_i + i\kappa\sigma_i)\mathbf{z}|^2 - h\mathbf{z}^\dagger\sigma_z\mathbf{z}] \quad (2.25)$$

where $i = x, y$, $\kappa = \frac{\bar{D}}{2J}$ and $h = \frac{\bar{B}}{2J}$. Under the gauge transformation

$$\mathbf{z} \rightarrow e^{i\theta(\mathbf{r})}\mathbf{z}, \quad a_i \rightarrow a_i + \partial_i\theta(\mathbf{r}), \quad (2.26)$$

the Hamiltonian is invariant. Another important relationship is

$$\mathbf{n} \cdot (\partial_x \mathbf{n} \times \partial_y \mathbf{n}) = (\nabla \times \mathbf{a})_z. \quad (2.27)$$

In 2D, the curl of the emergent gauge field is the density of topological charge without the constant $\frac{1}{4\pi}$, we define $b = (\nabla \times \mathbf{a})_z$. So in CP^1 model, the simp way to study the topological charge is to solve the emergent gauge field \mathbf{a} .

2.3.4 Mean field approximation

In path integral,

$$\mathcal{Z} = \int \mathcal{D}\mathbf{z}^\dagger \mathcal{D}\mathbf{z} \prod_{i=1,2} \mathcal{D}a_i \exp\left(-\frac{H}{T}\right) \delta(\mathbf{z}^\dagger\mathbf{z} - 1), \quad (2.28)$$

delta function can be replaced by

$$\delta(\mathbf{z}^\dagger\mathbf{z} - 1) = \int \mathcal{D}\lambda \exp\left\{\int d^2r [i\lambda(\mathbf{z}^\dagger\mathbf{z} - \mathbf{1})]\right\}, \quad (2.29)$$

where the auxiliary field λ is introduced to fix the module of the field \mathbf{z} . A rescaling $\mathbf{z} \rightarrow \sqrt{\frac{2J}{T}}\mathbf{z}$ and $\lambda \rightarrow \frac{T}{2J}\lambda$ [108] has been performed to make the Hamiltonian

simpler,

$$\begin{aligned} \mathcal{Z} = \int \mathcal{D}\mathbf{z}^\dagger \mathcal{D}\mathbf{z} \prod_{i=1,2} \mathcal{D}\lambda \exp\{ \int d^2r (-[(\partial_i - ia_i + i\kappa\sigma_i)\mathbf{z}]^2 \\ - h\mathbf{z}^\dagger \sigma_z \mathbf{z} + i\lambda(\mathbf{z}^\dagger \mathbf{z} - \frac{2}{f})) \}, \end{aligned} \quad (2.30)$$

where $f = \frac{T}{J}$. The mean field approximation[113] is to deal with the auxiliary field λ . We extend the CP^1 model to the $CP^{\mathcal{N}-1}$ model in which the field \mathbf{z} has \mathcal{N} flavors and $|\mathbf{z}^\dagger \mathbf{z}| = \frac{\mathcal{N}}{2}$. The fields can be rescaled as $\mathbf{z} \rightarrow \sqrt{\frac{2J}{T}}\mathbf{z}$ and define $h = \frac{\bar{B}}{2J}$, $f = \frac{T}{J}$, and $\lambda \rightarrow \frac{f}{2}\lambda$. The partition function transforms into

$$\mathcal{Z} = \int \mathcal{D}\mathbf{z}^\dagger \mathcal{D}\mathbf{z} \mathcal{D}a_i \mathcal{D}\lambda \exp\{ \int d^2r (-[(\partial_i - ii + i\kappa\sigma_i)\mathbf{z}]^2 - h\mathbf{z}^\dagger \sigma_z \mathbf{z} - i\lambda(\mathbf{z}^\dagger \mathbf{z} - \frac{\mathcal{N}}{f})) \}. \quad (2.31)$$

After integrating out the field \mathbf{z} , the partition function has a more concise form

$$\mathcal{Z} = \int \mathcal{D}a_i \mathcal{D}\lambda \exp(-S_{eff}[a_i, \lambda]).$$

$$S_{eff}[i, \lambda] = C' + Tr \log[-(\partial_i - ii + i\kappa\sigma_i)^2 + h\sigma_z + i\lambda] - \frac{\mathcal{N}i}{f} \int d^2r \lambda, \quad (2.32)$$

where C' is a constant. When we consider $\mathcal{N} \rightarrow \infty$, the effective action can be approximated by the quadratic fluctuation around the saddle point. The saddle point is $i\langle \lambda \rangle = \bar{\lambda}$, $\langle a_i \rangle = 0$. Because of $h \ll |\frac{\mathcal{N}\bar{\lambda}}{f}|$ when $\mathcal{N} \rightarrow \infty$ with a finite temperature, we can ignore the Zeeman coupling term in large \mathcal{N} approximation. The effective action around saddle point in momentum space is

$$S_{eff}[0, \bar{\lambda}] = C'' + \sum_k \log[(k^2 + \bar{\lambda} + 2\kappa^2)^2 - 4\kappa^2 k^2] - \frac{\mathcal{N}L^2 \bar{\lambda}}{f} \quad (2.33)$$

where L^2 is the area of the space. Here, we use to relationship of $\sigma_3 \sigma_i \sigma_3 = -\sigma_i$ and $Tr \log(ABC) = Tr \log(CAB)$ to work out the trace. By replacing \sum_k by

$L^2 \int \frac{d^2k}{(2\pi)^2}$, we can obtain

$$\frac{1}{2} \int_{-A}^A \frac{d^2k}{(2\pi)^2} \frac{2(k^2 + \bar{\lambda} + 2\kappa^2)}{(k^2 + \bar{\lambda} + 2\kappa^2)^2 - 4\kappa^2 k^2} - \frac{\mathcal{N}}{f} = 0. \quad (2.34)$$

The momentum in the integral has a cutoff $A \sim \frac{1}{a}$ due to the correlation length.

The saddle point equation can be transformed into

$$\log \frac{A^2 + \bar{\lambda} + 2\kappa^2}{\bar{\lambda} + 2\kappa^2} + \frac{2\kappa}{\sqrt{\bar{\lambda} + \kappa^2}} \arctan \frac{\kappa}{\sqrt{\bar{\lambda} + \kappa^2}} \approx \frac{2\pi\mathcal{N}}{f} \quad (2.35)$$

based on the assumption $\kappa^2 \ll \bar{\lambda} < A^2$. Also, the second term on the left side can be neglected. Turning back to $CP^1(\mathcal{N} = 2)$ mode, the solution has a simple form

$$\log \frac{A^2 + m_0^2}{m_0^2} \approx \frac{4\pi}{f}, \quad (2.36)$$

where $m_0^2 = \bar{\lambda} + 2\kappa^2$. This scheme is the hard cutoff scheme. Also we can employ the Pauli-Villars regularization[114, 115, 116] which can protect the gauge symmetry and translational symmetry. We integrate over k from $-\infty$ to ∞ , and replace $\int_{-\infty}^{\infty} \frac{d^2k}{(2\pi)^2} \frac{2(k^2 + \bar{\lambda} + 2\kappa^2)}{(k^2 + \bar{\lambda} + 2\kappa^2)^2 - 4\kappa^2 k^2}$ by $\frac{1}{2} \int_{-\infty}^{\infty} \frac{d^2k}{(2\pi)^2} \frac{2(k^2 + \bar{\lambda} + 2\kappa^2)}{(k^2 + \bar{\lambda} + 2\kappa^2)^2 - 4\kappa^2 k^2} - \int_{-\infty}^{\infty} \frac{d^2k}{(2\pi)^2} \frac{1}{k^2 + \Lambda_{PV}^2}$ where Λ_{PV} is the cutoff. The solution in Pauli-Villars regularization is

$$\log \frac{\Lambda_{PV}^2}{m_0^2} \approx \frac{4\pi}{f}. \quad (2.37)$$

In hard cut-off scheme, there is no need to assume $m_0^2 \ll A^2$, we can perform this model when m_0 is comparable with the cut-off A . Also, in very low temperature region, ($f \ll 1$) we can get $m_0^2 \ll A^2$ in both schemes which means at low temperature, $\log \frac{A^2}{m_0^2} \approx \frac{4\pi}{f}$ works for both schemes. One problem left to be clarified is why the cut-off A has the scale as $\frac{1}{a}$, where a is the lattice constant

2.3.5 Cut-off Λ and correlation length

In eqn.(37), $m_0^2 = \Lambda^2 \exp(-\frac{4\pi}{f})$. for the purpose to clarify the problem simplify, the κ term is neglected because $\kappa \ll \Lambda$, $H = \int d^2r 2J |(\partial_i - ia_i)\mathbf{z}|^2$, and the propagator is

$$\begin{aligned} G(x) &= \frac{1}{\mathcal{Z}} \int \mathcal{D}\mathbf{z}^\dagger \mathcal{D}\mathbf{z} \mathbf{z}^\dagger(0)\mathbf{z}(x) \exp[-\frac{2}{f} \sum_k \mathbf{z}_k^\dagger (k^2 + m_0^2)\mathbf{z}_k - \sum_k \frac{2m_0^2}{f}] \\ &= \frac{1}{2} \sum_k \frac{e^{-i\mathbf{k}\cdot\mathbf{x}}}{k^2 + m_0^2} \sim \frac{1}{|\mathbf{x}|} \exp(-|\mathbf{x}|m_0). \end{aligned} \quad (2.38)$$

The two-point correlation function can be defined as

$$\begin{aligned} S^{+-}(x) &= \langle [n_x(0) + in_y(x)][n_x(x) - in_y(x)] \rangle \\ &\rightarrow \langle z_m^*(0)z_{m'}(0)z_m^*(x)z_m(x) \rangle \\ &= S^{m \neq m'}(x) = |G(x)|^2 \sim \frac{1}{|\mathbf{x}|^2} \exp(-|x|/(1/2m_0)) \end{aligned}$$

So we define the correlation length ξ ,

$$\xi = \frac{1}{2m_0} = \frac{1}{2\Lambda} \exp(\frac{2\pi}{f}). \quad (2.39)$$

Going back to the square lattice model, the separation of the two nearest neighbors is lattice constant a . If the correlation length is less than a , the nearest spins are no longer correlated. It means below the energy scale Λ , the spins will correlate to others. But above Λ , the energy of local spin vibration will increase, but cannot propagate to others. The continuum model does not work any longer above the energy scale Λ . That is the reason why we choose $\Lambda \sim \frac{1}{a}$ as the cut-off.

2.3.6 The effective action of the emergent gauge field

The basic idea in what follows is to integrate out the \mathbf{z} field, and get the effective action theory in terms of the gauge field \mathbf{a} . The gauge invariant requirement gives rise to only two possible terms up to the second order of the emergent gauge field \mathbf{a} in the effective action. The procedure for finding them two begins with the antisymmetric tensor $f_{ij} = \partial_i a_j - \partial_j a_i (i, j = x, y)$, which is easy to prove gauge invariant. One is $\sum_{ij} f_{ij} f_{ij}$ which corresponds to the quadratic term b^2 . Another one is $\sum_{ij} \varepsilon_{zij} h_z f_{ij}$ which is the term hb . A perturbative calculation in field theory is employed to work out the effective action of emergent gauge field \mathbf{a} . In momentum space, the unperturbed part of the action is

$$\mathbf{S}_0 = L^2 \int \frac{d^2 k}{(2\pi)^2} \mathbf{z}_k^\dagger (k^2 + m_0^2 - 2\kappa k_i \sigma_i) \mathbf{z}_k, \quad (2.40)$$

where L^2 is the area of the 2D film. The corresponding Feynman diagram is shown in Figure 2.6(a).

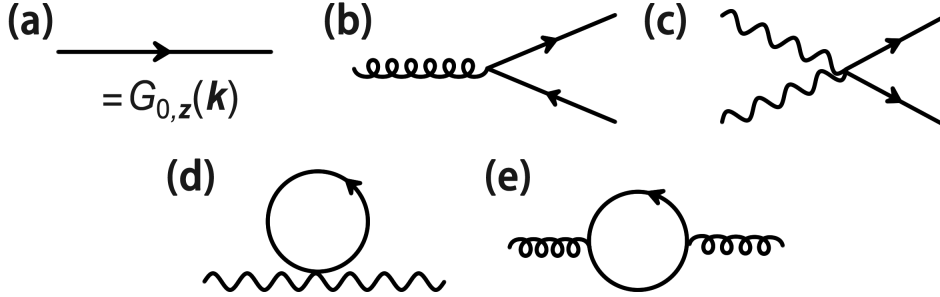


Figure 2.6: Feynman rules and diagrams.

The perturbative part of the action is divided into two terms which are

$$S_{i1} = L^4 \int \frac{d^2 k d^2 q}{(2\pi)^4} \mathbf{z}_{k+\frac{q}{2}}^\dagger (-2k_i a_{i,q} - 2\kappa a_{i,q} \sigma_i - h\sigma_z) \mathbf{z}_{k-\frac{q}{2}}, \quad (2.41)$$

$$S_{i2} = L^4 \int \frac{d^2 k d^2 q}{(2\pi)^4} \mathbf{z}_k^\dagger \mathbf{z}_q a_{i,p} a_{i,k-q-p} \quad (2.42)$$

The Feynman diagram Figure 2.6(b) corresponds to S_{i1} , where the spring line represents the part $-2(k_i a_{i,q} + \kappa a_{i,q} + \frac{\hbar}{2} \sigma_z)$ in the three-point vertex. Figure 2.6(c) is four point interaction in S_{i2} . The tilde line represents the pure emergent gauge field a_i .

The Green's function of field \mathbf{z} is $G_{0,z}(k) = \langle \mathbf{z}_k \mathbf{z}_k^\dagger \rangle = \frac{1}{k^2 + m_0^2 - 2\kappa k_i \sigma_i}$. As discussed Figure 2.6(b) corresponds to the interaction described by S_{i1} . The action described by the process in Figure 2.6(d) is

$$\begin{aligned} S_d &= L^4 \text{Tr} \int \frac{d^2 k d^2 q}{(2\pi)^4} \frac{a_{i,q} a_{i,-q}}{k^2 + m_0^2 - 2\kappa k_i \sigma_i} \\ &= L^4 \int \frac{d^2 k d^2 q}{(2\pi)^4} \left[\frac{2i, q_i, q}{k^2 + m_0^2} + \frac{4\kappa^2 k^2 a_{i,q}^2}{(k^2 + m_0^2)^4} + \mathcal{O}(\kappa^4) \right]. \end{aligned} \quad (2.43)$$

Because of $\frac{\kappa^2}{\Lambda^2} \ll 1$, the terms of κ^2 and higher order can be neglected. The Pauli-Villars regularization is applied to the divergent integral,

$$\begin{aligned} \int \frac{d^2 k}{(2\pi)^2} \frac{1}{k^2 + m_0^2} &\rightarrow \int \frac{d^2 k}{(2\pi)^2} \left(\frac{1}{k^2 + m_0^2} - \frac{1}{k^2 + \Lambda_{PV}^2} \right) \\ &= \frac{1}{4\pi} \log \frac{\Lambda_{PV}^2}{m_0^2}. \end{aligned} \quad (2.44)$$

So

$$S_d = \frac{L^4}{2\pi} \log \frac{\Lambda_{PV}^2}{m_0^2} \int \frac{d^2 q}{(2\pi)^2} a_{i,q} a_{i,-q}. \quad (2.45)$$

The process in Figure 2.6(e) corresponds to the action

$$\begin{aligned}
S_e &= -\frac{L^4}{2!} \int \frac{d^2k d^2q}{(2\pi)^4} \\
&\quad \times \langle 2\mathbf{z}_{k+\frac{q}{2}}^\dagger (-k_i a_{i,q} - \kappa a_{i,q} \sigma_i - \frac{h_q}{2} \sigma_z) \mathbf{z}_{k-\frac{q}{2}} \\
&\quad \times 2\mathbf{z}_{k-\frac{q}{2}}^\dagger (-k_j a_{j,-q} - \kappa a_{j,-q} \sigma_j - \frac{h_{-q}}{2} \sigma_z) \mathbf{z}_{k+\frac{q}{2}} \rangle \\
&= -2L^4 \text{Tr} \int \frac{d^2k d^2q}{(2\pi)^4} \frac{1}{(k+\frac{q}{2})^2 + m_0^2 - 2\kappa(k+\frac{q}{2})_{i'} \sigma_{i'}} (k_i a_{i,-q} + \kappa a_{i,-q} \sigma_i + \frac{h_{-q}}{2} \sigma_z) \\
&\quad \times \frac{1}{(k-\frac{q}{2})^2 + m_0^2 - 2\kappa(k-\frac{q}{2})_{j'} \sigma_{j'}} (k_j a_{j,q} + \kappa a_{j,q} \sigma_j + \frac{h_q}{2} \sigma_z) \\
&= -2L^4 \int \frac{d^2k d^2q}{(2\pi)^4} \left[\frac{1}{(k+\frac{q}{2})^2 + m_0^2} + \frac{2\kappa(k+\frac{q}{2})_{i'} \sigma_{i'}}{[(k+\frac{q}{2})^2 + m_0^2]^2} + \mathcal{O}(\kappa^2) \right] \\
&\quad \times (k_i a_{i,-q} + \kappa a_{i,-q} \sigma_i + \frac{h_{-q}}{2} \sigma_z) \left[\frac{1}{(k-\frac{q}{2})^2 + m_0^2} \right. \\
&\quad \left. + \frac{2\kappa(k-\frac{q}{2})_{j'} \sigma_{j'}}{[(k-\frac{q}{2})^2 + m_0^2]^2} + \mathcal{O}(\kappa^2) \right] (k_j a_{j,q} + \kappa a_{j,q} \sigma_j + \frac{h_q}{2} \sigma_z) \\
&= -2L^4 \text{Tr} \int \frac{d^2k d^2q}{(2\pi)^4} \left[\frac{k^2 a_q^2 + \kappa^2 a_q^2 + \frac{h_q^2}{4}}{[(k+\frac{q}{2})^2 + m_0^2][(k-\frac{q}{2})^2 + m_0^2]} \right. \\
&\quad \left. + \frac{(k_i a_{i,-q} + \kappa a_{i,-q} \sigma_i + \frac{h_{-q}}{2} \sigma_z)}{(k+\frac{q}{2})^2 + m_0^2} \frac{2\kappa(k-\frac{q}{2})_{j'} \sigma_{j'}}{[(k-\frac{q}{2})^2 + m_0^2]^2} (k_j a_{j,q} + \kappa a_{j,q} \sigma_j + \frac{h_q}{2} \sigma_z) \right. \\
&\quad \left. + \frac{2\kappa(k+\frac{q}{2})_{i'} \sigma_{i'}}{[(k+\frac{q}{2})^2 + m_0^2]^2} (k_i a_{i,-q} + \kappa a_{i,-q} \sigma_i + \frac{h_{-q}}{2} \sigma_z) \frac{(k_j a_{j,q} + \kappa a_{j,q} \sigma_j + \frac{h_q}{2} \sigma_z)}{(k-\frac{q}{2})^2 + m_0^2} \right. \\
&\quad \left. + \mathcal{O}(\kappa^2) \right]. \tag{2.46}
\end{aligned}$$

?s?? We do not consider the $\kappa^2 a_i^2$ term with the same reason in S_b . Also h^2 term is neglected because it decouples with a_i . We employ Feynman parametrization to work out the integrals

$$S_{e1} = -4L^4 \int \frac{d^2q d^2k}{(2\pi)^4} \int_0^1 dx \frac{(k_i a_i)^2}{\{x[(k+\frac{q}{2})^2 + m_0^2] + (1-x)[(k-\frac{q}{2})^2 + m_0^2]\}^2} \tag{2.47}$$

with

$$\begin{aligned}
A &= \int \frac{d^2k}{(2\pi)^2} \int_0^1 dx \frac{(k_i a_i)^2}{[k^2 + \frac{q^2}{4} + m_0^2 + 2(x - \frac{1}{2})k \cdot q]^2} \\
&= \int_0^1 dx \int \frac{d^2k}{(2\pi)^2} \frac{(k_i a_i)^2}{\{[k + (x - \frac{1}{2})q]^2 + \frac{q^2}{4} + m_0^2 - (x - \frac{1}{2})^2 q^2\}^2} \\
&= \int_0^1 dx \int \frac{d^2l}{(2\pi)^2} \frac{\{[l - (x - \frac{1}{2})q]_i a_i\}^2}{[l^2 + m_0^2 + x(1-x)q^2]^2}, \tag{2.48}
\end{aligned}$$

where $l = k + (x - \frac{1}{2})q$ and define $\Delta = m_0^2 + x(1-x)q^2$. A is divided into two parts

$$\begin{aligned}
A &= A_1 + A_2 \\
A_1 &= \int_0^1 dx \int \frac{d^2l}{(2\pi)^2} \frac{(l_i a_i)^2}{(l^2 + \Delta)^2} \\
&= \int_0^1 dx \int_0^{2\pi} d\theta \int_0^\infty \frac{ldl}{(2\pi)^2} \frac{(l|\mathbf{a}|\cos\theta)^2}{(l^2 + \Delta)^2} \\
&= \frac{1}{4\pi^2} \int_0^{2\pi} d\theta \cos^2\theta \int_0^1 dx \int_0^\infty \frac{dl^2}{2} \frac{l^2}{(l^2 + \Delta)^2} a^2 \\
&= \frac{1}{8\pi^2} \int_0^1 dx \int_0^{2\pi} d\theta \left(\frac{1 + \cos 2\theta}{2}\right) \int_0^\infty dl^2 \frac{l^2 a^2}{(l^2 + \Delta)^2} \\
&= \frac{1}{8\pi} \int_0^1 dx \int_0^\infty dl^2 \frac{l^2 a^2}{(l^2 + \Delta)^2} \tag{2.49}
\end{aligned}$$

$$\begin{aligned}
A_2 &= \frac{1}{4\pi} \int_0^1 dx \int \frac{d^2l}{(2\pi)^2} \frac{(x - \frac{1}{2})^2 (q_i a_i)^2}{(l^2 + \Delta)^2} \\
&= \frac{1}{4\pi} \int_0^1 dx \int_0^\infty dl^2 \frac{(x - \frac{1}{2})^2 (q_i a_i)^2}{(l^2 + \Delta)^2} \\
&= \frac{1}{4\pi} \int_0^1 dx \left[-\frac{(x - \frac{1}{2})^2 (q_i a_i)^2}{l^2 + \Delta} \right]_{l^2=0}^{l^2=\infty} \\
&= \frac{1}{4\pi} \int_0^1 dx \frac{(x - \frac{1}{2})^2 (q_i a_i)^2}{m_0^2 + x(1-x)q^2} \\
&= \frac{1}{4\pi} \frac{(q_i a_i)^2}{q^2} \left[-1 + \frac{1}{2} \sqrt{\frac{q^2 + 4m_0^2}{q^2}} \log\left(\frac{\sqrt{q^2 + 4m_0^2} + q}{\sqrt{q^2 + 4m_0^2} - q}\right) \right] \quad (2.50)
\end{aligned}$$

The integral in A_1 is divergent. As the same as above, Pauli-Villars regularization is applied to deduct the divergent part,

$$\begin{aligned}
A_1 \rightarrow A'_1 &= \frac{1}{8\pi} \int_0^1 dx \int_0^\infty dl^2 \left\{ \frac{l^2 a_i^2}{[l^2 + m_0^2 + x(1-x)q^2]^2} - \frac{l^2 a_i^2}{(l^2 + \Lambda_{PV}^2)^2} \right\} \\
&= \frac{1}{8\pi} \int_0^1 dx \left(\log \frac{\Lambda_{PV}^2}{m_0^2 + x(1-x)q^2} \right) a_i^2 \\
&= \frac{1}{8\pi} \int_0^1 dx \{ \log \Lambda_{PV}^2 - \log [m_0^2 + x(1-x)q^2] \} a_i^2 \\
&= \frac{1}{8\pi} \left[\log \frac{\Lambda_{PV}^2}{m_0^2} + 2 - \sqrt{\frac{q^2 + 4m_0^2}{q^2}} \log\left(\frac{\sqrt{q^2 + 4m_0^2} + |q|}{\sqrt{q^2 + 4m_0^2} - |q|}\right) \right] a_i^2, \quad (2.51)
\end{aligned}$$

where $a_i^2 = a_{i,q} a_{i,-q}$.

$$\begin{aligned}
S_{e1} &= -\frac{L^4}{2\pi} \int \frac{d^2q}{(2\pi)^2} \left[2 - \sqrt{\frac{q^2 + 4m_0^2}{q^2}} \log\left(\frac{\sqrt{q^2 + 4m_0^2} + |q|}{\sqrt{q^2 + 4m_0^2} - |q|}\right) \right] \\
&\quad \times a_i (\delta_{ij} - \frac{q_i q_j}{q^2}) a_j - \frac{1}{2\pi} \log \frac{\Lambda_{PV}^2}{m_0^2} \int \frac{d^2q}{(2\pi)^2} a_i^2 \quad (2.52)
\end{aligned}$$

and

$$\begin{aligned}
S_{a^2} = S_d + S_{e1} &= \frac{L^4}{\pi} \int \frac{d^2q}{(2\pi)^2} \left[\frac{1}{2} \sqrt{\frac{q^2 + 4m_0^2}{q^2}} \log\left(\frac{\sqrt{q^2 + 4m_0^2} + |q|}{\sqrt{q^2 + 4m_0^2} - |q|}\right) - 1 \right] \\
&\times a_i \left(\delta_{ij} - \frac{q_i q_j}{q^2} \right) a_j. \tag{2.53}
\end{aligned}$$

The gauge violent terms in S_d and S_{e1} cancel with each other. We expand S_{a^2} by the order of q^2 ,

$$S_{a^2} = \frac{L^4}{\pi} \int \frac{d^2q}{(2\pi)^2} \left[\frac{q^2}{12m_0^2} - \frac{(q^2)^2}{120m_0^4} + \mathcal{O}((q^2)^4) \right] a_{i,q} \left(\delta_{ij} - \frac{q_i q_j}{q^2} \right) a_{j,-q}. \tag{2.54}$$

In the main text, $b = (\nabla \times \mathbf{a})_z$ has been defined. S_{a^2} has another form as S_{b^2}

$$S_{b^2} = \frac{L^4}{\pi} \int \frac{d^2q}{(2\pi)^2} \frac{b_q^2}{12m_0^2} + \mathcal{O}(q^2 b^2), \tag{2.55}$$

where $b_q = i\varepsilon_{zij} q_i a_{j,q}$. By using the result in Eqn.(2.37)

$$S_{b^2} = \frac{L^4}{\pi} \int \frac{d^2q}{(2\pi)^2} \left[\frac{b_q^2}{12\Lambda_{PV}^2} \exp\left(\frac{4\pi}{f}\right) + \mathcal{O}(q^2 b^2) \right]. \tag{2.56}$$

The effective action of hb term in S_e is

$$\begin{aligned}
S_{e2} = S_{hb} &= -4L^4 \int \frac{d^2k d^2q}{(2\pi)^4} \left[\frac{i\kappa^2 \varepsilon_{ijz} (k + \frac{q}{2})_i a_{j,-q} h_q + i\kappa^2 \varepsilon_{izj} (k + \frac{q}{2})_i h_{-q} a_{j,q}}{[(k + \frac{q}{2})^2 + m_0^2]^2 [(k - \frac{q}{2})^2 + m_0^2]} \right. \\
&\quad \left. + \frac{i\kappa^2 \varepsilon_{ijz} a_{i,-q} (k - \frac{q}{2})_j h_q + i\kappa^2 \varepsilon_{zij} h_{-q} (k - \frac{q}{2})_i a_{j,q}}{[(k + \frac{q}{2})^2 + m_0^2] [(k - \frac{q}{2})^2 + m_0^2]^2} \right] \\
&= 4\kappa^2 L^4 \int \frac{d^2k d^2q}{(2\pi)^4} \left\{ \frac{4\mathbf{k} \cdot \mathbf{q} (i\varepsilon_{zij}) k_i (a_{j,-q} h_q - a_{j,q} h_{-q})}{[(k + \frac{q}{2})^2 + m_0^2]^2 [(k - \frac{q}{2})^2 + m_0^2]^2} \right. \\
&\quad \left. + \frac{2(k^2 + \frac{q^2}{4} + m_0^2)(b_q h_{-q} + b_{-q} h_q)}{[(k + \frac{q}{2})^2 + m_0^2]^2 [(k - \frac{q}{2})^2 + m_0^2]^2} \right\}. \tag{2.57}
\end{aligned}$$

$(\mathbf{k} \cdot \mathbf{q}) k_i$ can be replaced by $\frac{1}{2} k^2 q_i$ in the integral. Following the procedure of the

Feynman parametrization used above,

$$\begin{aligned}
S_{hb} &= 8\kappa^2 L^4 \int_0^1 dx \int \frac{d^2 l d^2 q}{(2\pi)^4} \frac{\kappa^2 h_{-q} b_q (\frac{q^2}{4} + m_0^2)}{(l^2 + \Delta)^4} \\
&= 8\kappa^2 L^4 \int_0^1 dx \int \frac{d^2 q}{(2\pi)^2} \int_{-\Lambda}^{\Lambda} \frac{d^2 l}{(2\pi)^2} \frac{(\frac{q^2}{4} + m_0^2) h_{-q} b_q}{(l^2 + \Delta)^4}. \tag{2.58}
\end{aligned}$$

The momentum has bounds in the integral due to the correlation length. The hard cutoff scheme is applied to work out the integral,

$$S_{hb} = \frac{2L^4 \kappa^2}{\pi} \int_0^1 dx \int \frac{d^2 q}{(2\pi)^2} \left[\frac{1}{\Delta^3} - \frac{1}{(\Lambda^2 + \Delta)^3} \right] (\frac{q^2}{4} + m_0^2) h_{-q} b_q. \tag{2.59}$$

Expanding the action by q^2 ,

$$S_{hb} = \frac{2L^4 \kappa^2}{\pi} \int \frac{d^2 q}{(2\pi)^2} \left[\frac{(\Lambda^2 + m_0^2)^3 - m_0^6}{m_0^4 (\Lambda^2 + m_0^2)^3} + \mathcal{O}(q^2) \right] h_{-q} b_q. \tag{2.60}$$

S_{b^2} and S_{hb} are added together. In position space,

$$S_{b^2} + S_{hb} = \frac{1}{\pi} \int d^2 r \left[\frac{b^2(r)}{12\Lambda_{PV}^2} \exp(\frac{4\pi}{f}) + \frac{(\Lambda^2 + m_0^2)^3 - m_0^6}{2m_0^4 (\Lambda^2 + m_0^2)^3} h b(r) + \mathcal{O}(\partial^2 b) \right]. \tag{2.61}$$

Here, we can simply set $\Lambda_{PV} = \Lambda$. Ignoring the fluctuation of the $b(r)$, the average value of $b(r)$ is obtained through the saddle point equation $\frac{\delta(S_{b^2} + S_{hb})}{\delta b(r)} = 0$,

$$\bar{b} = -\frac{3\Lambda^2}{m_0^4} \left[1 - \left(\frac{m_0^2}{\Lambda^2 + m_0^2} \right)^3 \right] \exp\left(-\frac{4\pi}{f}\right) \tag{2.62}$$

. The result in eqn.(23) is applied to obtain \bar{b} as a function of temperature,

$$\begin{aligned}\bar{b} &\approx -\frac{3\kappa^2 h}{\Lambda^2} [\exp(\frac{4\pi}{f}) - 1]^2 [1 - \exp(-\frac{12\pi}{f})] \exp(-\frac{4\pi}{f}) \\ &= -\frac{12\kappa^2 h}{\Lambda^2} \sinh^2(\frac{2\pi}{f}) [1 - \exp(-\frac{12\pi}{f})].\end{aligned}\quad (2.63)$$

At the high temperature ($\frac{1}{f} \ll 1$), we can expand the \bar{b} by the order of $\frac{1}{f}$,

$$\bar{b} = -\frac{9\kappa^2 h}{\Lambda^2} [(\frac{4\pi}{f})^3 - \frac{3}{2}(\frac{4\pi}{f})^4 + \mathcal{O}(\frac{1}{f^5})].\quad (2.64)$$

The average of topological charge is

$$\langle Q \rangle \approx \frac{1}{4\pi} \int d^2\bar{b} \quad (2.65)$$

$$= -\frac{N^2 a^2}{4\pi} \frac{9\kappa^2 h}{\Lambda^2} [(\frac{4\pi}{f})^3 - \frac{3}{2}(\frac{4\pi}{f})^4 + \mathcal{O}(\frac{1}{f^5})].\quad (2.66)$$

.By using the parameters in the lattice Hamiltonian ($\kappa = \frac{\bar{D}}{2J} = \frac{D}{2Ja}$, $h = \frac{\bar{B}}{2J} = \frac{B}{2Ja^2S}$, $f = \frac{T}{J} = \frac{T}{JS^2}$) with $\Lambda = \frac{1}{a}$, we have

$$\langle Q \rangle \approx -\frac{18\pi^2 N^2 D^2 B S^5}{T^3} [1 - \frac{6\pi JS^2}{T} + \mathcal{O}(\frac{1}{T^2})] \quad (2.67)$$

$$= -\frac{18\pi^2 L^2 B S^5}{T^3} (\frac{D}{a})^2 [1 - \frac{6\pi JS^2}{T} + \mathcal{O}(\frac{1}{T^2})], \quad (2.68)$$

where $\frac{D}{a}$ is the DM interaction in the continuum limit. This result matches well with the simple argument based on one triangle in $\frac{1}{T^3}$ and $\frac{1}{T^4}$ order. In one triangles the signs of these two are opposite and proportional to D^2B and D^2BJ respectively.

2.4 Experimental evidence

In Chapter I, we introduced that the topological Hall resistivity is proportional to the topological charge in magnetic systems. Experiments on thin film chiral magnetic metals SrRuO₃ and V-doped Sb₂Te₃ have investigated the topological Hall effect. It has shown that the topological Hall signal is significant above the Curie temperature[103]. They measured the Hall resistivity of the thin film samples and subtract the contribution from OHE and AHE. The thin film SrRuO₃ and V-doped Sb₂Te₃ have different density of carriers. Here, we compared the experimental results of thin film SrRuO₃ and our theoretical results. The ex-

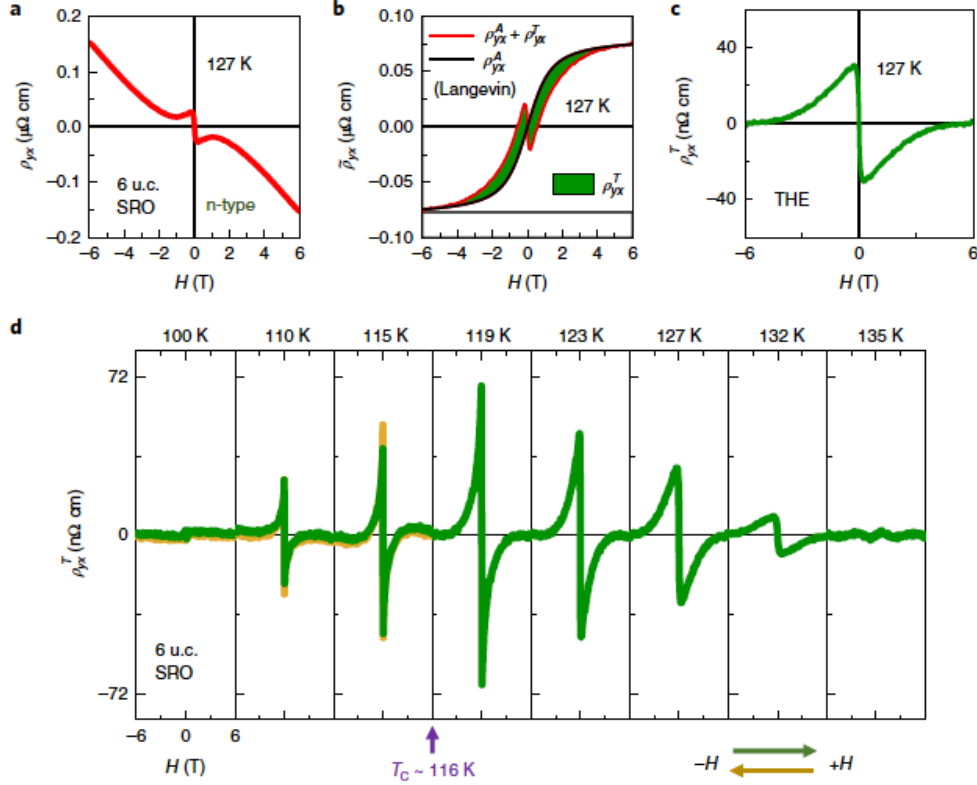


Figure 2.7: (a) Total Hall resistivity. (b) Anomalous Hall resistivity is subtracted. (c) Topological Hall effect. (d) The relationship between topological resistivity and temperature. Right top is the thickness dependence of the topological Hall resistivity[103].

periment was done on a sandwich structure SrTiO₃-SrRuO₃-SrTiO₃. The DM

interaction is due to the interface of SrTiO₃ and SrRuO₃. Figure 2.7(a) is the total Hall resistivity. THE signal is subtracted from the total. By the linear relationship between external magnetic field and ordinary Hall resistivity, they subtracted the OHE signal. (b) shows anomalous Hall resistivity is subtracted by employed the Langevin method, left the topological hall resistivity as Figure 2.7(c) shows. (d) indicates the peak of topological Hall resistivity is above the Curie temperature. The we compare the theoretical results and our theoretical results shown in Figure 2.8. The configuration of topological Hall resistivity in Figure 2.8 (a) has

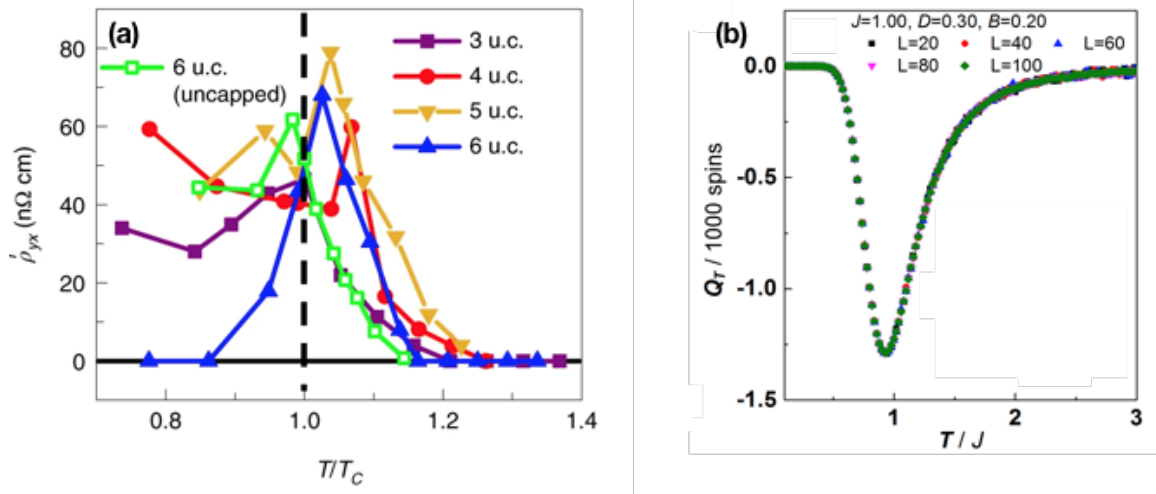


Figure 2.8: (a) The thickness dependence of the topological Hall resistivity. (b) The theoretical results of the topological charge.

matched our theoretical results in Figure 2.8 (b). The peak of the Hall resistivity emerges above the Curie temperature, and in our theoretical results, the valley of the topological charges emerge at the random phase which appears with a higher temperature than the Skyrmion crystal phase. Here are two things need to be mentioned. First there is no stable Skyrmion phase has been discovered in the thin film SrRuO₃. Another, in their work, they used spin chirality in stead of the topological charge. In their work they used spin chirality not the topological charge. We also investigated topological charge and spin chirality. The results

indicate they are not identical.

2.5 Spin chirality, topological charge and Hall resistivity

For the purpose to investigate the Hall effect, the Kubo formula[117, 118, 119, 120] is employed to calculate the Hall conductivity, the form we used is

$$\sigma_{xx}(\omega) = \frac{e^2}{\hbar} \text{Re} \sum_{m \neq n} \frac{[f(\varepsilon_m) - f(\varepsilon_n)] \langle m | \hat{v}_x | n \rangle \langle n | \hat{v}_x | m \rangle}{(\varepsilon_m - \varepsilon_n)^2 - (\omega + i\eta)^2}, \quad (2.69)$$

$$\sigma_{xy}(\omega) = \frac{e^2}{\hbar} \text{Im} \sum_{m \neq n} \frac{[f(\varepsilon_m) - f(\varepsilon_n)] \langle m | \hat{v}_x | n \rangle \langle n | \hat{v}_y | m \rangle}{(\varepsilon_m - \varepsilon_n)^2 - (\omega + i\eta)^2}. \quad (2.70)$$

where ε_m is the energy of the electron's eigenstate $|m\rangle$. The $f(\varepsilon_m)$ is the Fermion distribution function which is

$$f(\varepsilon_m) = \frac{1}{\exp(\varepsilon_m - \mu) + 1}. \quad (2.71)$$

Here, we used the natural unit $\hbar = c = k_B = 1$ for simplicity. When $\omega = 0$, $\sigma_{xx} = \sigma_{yy} = \sigma_{xx}(0)$ and $\sigma_{xy} = \sigma_{xy}(0)$ are we concerned. The conductivity is

$$\sigma_c = \begin{pmatrix} \sigma_{xx} & \sigma_{xy} \\ \sigma_{yx} & \sigma_{yy} \end{pmatrix}. \quad (2.72)$$

The matrix of the resistivity is $\rho = \sigma_c^{-1}$. The Hamiltonian for the electrons within a spin system is

$$H = -t \sum_{\langle ij \rangle, \sigma} c_{i, \sigma}^\dagger c_{j, \sigma} - J_H \sum_i c_{i, \sigma}^\dagger \mathbf{S}_i \cdot \sigma_{\sigma \sigma'} c_{i, \sigma'}, \quad (2.73)$$

where $c_{i, \sigma}^\dagger$ and $c_{i, \sigma}$ are the creation and annihilation operators of the electrons at the i -site. σ and σ' are the spin index which can be \uparrow or \downarrow . \mathbf{S}_i is the local spin

of the i site. t is the hopping constant of the nearest spins and J_H is the Hund's coupling. The position operator is

$$\hat{R} = \sum_{i,\sigma} \mathbf{R}_i c_{i,\sigma}^\dagger c_{i,\sigma}, \quad (2.74)$$

where the vector \mathbf{R}_i indicates the position of the i site. \hat{R} acts on an eigenvector $|j, \sigma'\rangle$ of the electron which lays on the i site

$$\begin{aligned} \hat{R}|j, \sigma'\rangle &= \sum_{i,\sigma} \mathbf{R}_i c_{i,\sigma}^\dagger c_{i,\sigma} |j, \sigma'\rangle \\ &= \sum_{i,\sigma} \mathbf{R}_i c_{i,\sigma}^\dagger c_{i,\sigma} c_{j,\sigma'}^\dagger |0\rangle \\ &= \sum_{i,\sigma} \mathbf{R}_i c_{i,\sigma}^\dagger \{c_{i,\sigma}, c_{j,\sigma'}^\dagger\} |0\rangle - \sum_i R_i c_{i,\sigma}^\dagger c_{i,\sigma}^\dagger c_{j,\sigma'} |0\rangle \\ &= \sum_{i,\sigma} \mathbf{R}_i c_{i,\sigma}^\dagger \delta_{ij,\sigma\sigma'} |0\rangle \\ &= \mathbf{R}_j c_{j,\sigma'}^\dagger |0\rangle = \mathbf{R}_j |j, \sigma'\rangle \end{aligned} \quad (2.75)$$

Here , we define $\hat{R}_i = \sum_{\sigma} \mathbf{R}_i c_{i,\sigma}^{\dagger} c_{i,\sigma}$ for the i -site. The velocity operator is

$$\begin{aligned}
\hat{v}_i &= \dot{\hat{R}}_i = -i[\hat{R}_i, H] \\
&= -i \sum_{\sigma} [\mathbf{R}_i c_{i,\sigma}^{\dagger} c_{i,\sigma}, -t \sum_{\langle lm \rangle, \alpha} c_{l,\alpha}^{\dagger} c_{m,\alpha} - \sum_l J_H c_{l,\alpha}^{\dagger} \mathbf{S}_l \cdot \sigma_{\alpha\beta} c_{l,\beta}] \\
&= it \sum_{\sigma} [\mathbf{R}_i c_{i,\sigma}^{\dagger} c_{i,\sigma}, \sum_{\langle lm \rangle, \alpha} c_{l,\alpha}^{\dagger} c_{m,\alpha}] + iJ_H \sum_{\sigma, l} [c_{i,\sigma} c_{i,\sigma}^{\dagger}, c_{l,\alpha}^{\dagger} c_{l,\beta}] \mathbf{S}_l \cdot \sigma_{\alpha\beta} \\
&= it \sum_{i, \langle lm \rangle, \sigma, \alpha} \mathbf{R}_i [c_{i,\sigma}^{\dagger} c_{i,\sigma}, c_{l,\alpha}^{\dagger} c_{m,\alpha}] + iJ_H \sum_{i, \sigma, l} [c_{i,\sigma} c_{i,\sigma}^{\dagger}, c_{l,\alpha}^{\dagger} c_{l,\beta}] \mathbf{S}_l \cdot \sigma_{\alpha\beta} \\
&= it \sum_{i, \langle lm \rangle, \sigma, \alpha} \mathbf{R}_i (c_{i,\sigma}^{\dagger} \{c_{i,\sigma}, c_{l,\alpha}^{\dagger}\} c_{m,\alpha} - c_{l,\alpha}^{\dagger} \{c_{m,\alpha}, c_{i,\sigma}^{\dagger}\} c_{i,\sigma}) \\
&\quad + iJ \sum_{\sigma, l} \mathbf{R}_i [c_{i,\sigma}^{\dagger} \{c_{i,\sigma}, c_{l,\alpha}^{\dagger}\} c_{l,\beta} - c_{l,\alpha}^{\dagger} \{c_{l,\beta}, c_{i,\sigma}^{\dagger}\} c_{i,\sigma}] S_l \cdot \sigma_{\alpha\beta} \\
&= it \sum_{\langle lm \rangle, \sigma, \alpha} \mathbf{R}_i c_{i,\sigma}^{\dagger} \delta_{il} \delta_{\sigma\alpha} c_{m,\alpha} - \mathbf{R}_i c_{l,\alpha}^{\dagger} \delta_{mi} \delta_{\alpha\sigma} c_{i,\sigma} \\
&\quad + iJ \mathbf{R}_i (c_{i,\alpha}^{\dagger} c_{i,\beta} - c_{i,\alpha}^{\dagger} c_{i,\beta}) S_l \cdot \sigma_{\alpha\beta} \\
&= it \sum_{\sigma} \mathbf{R}_i (c_{i,\sigma}^{\dagger} c_{i+\text{nearest},\sigma} - c_{i+\text{nearest},\sigma}^{\dagger} c_{i,\sigma}). \tag{2.76}
\end{aligned}$$

So the velocity operator is

$$\hat{v} = it \sum_{i,\sigma} (\mathbf{R}_i c_{i,\sigma}^{\dagger} c_{i+\text{nearest},\sigma} - \mathbf{R}_i c_{i+\text{nearest},\sigma}^{\dagger} c_{i,\sigma}). \tag{2.77}$$

In 2D system, the components fo the velocity operator are

$$\hat{v}_x = it \sum_{i,\sigma} R_{i,x} (c_{i,\sigma}^{\dagger} c_{i+\hat{x},\sigma} + c_{i,\sigma}^{\dagger} c_{i-\hat{x},\sigma} - c_{i+\hat{x},\sigma}^{\dagger} c_{i,\sigma} - c_{i-\hat{x},\sigma}^{\dagger} c_{i,\sigma}), \tag{2.78}$$

$$\hat{v}_y = it \sum_{i,\sigma} R_{i,y} (c_{i,\sigma}^{\dagger} c_{i+\hat{y},\sigma} + c_{i,\sigma}^{\dagger} c_{i-\hat{y},\sigma} - c_{i+\hat{y},\sigma}^{\dagger} c_{i,\sigma} - c_{i-\hat{y},\sigma}^{\dagger} c_{i,\sigma}). \tag{2.79}$$

After diagonalizing the Hamiltonian, we can get the eigenvalues ε_m and the corresponding normalized eigenvectors $|m\rangle$. This system can also be described by

another set of complete orthogonal basis $|i, \sigma\rangle$, which is

$$c_{i,\sigma}^\dagger|0\rangle = |i, \sigma\rangle = \begin{pmatrix} 0 \\ \dots \\ 1 \rightarrow (2i + \alpha)th \\ 0 \\ \dots \end{pmatrix} \quad (2.80)$$

when $\sigma = \uparrow$, $\alpha = 1$ and $\sigma = \downarrow$, $\alpha = 2$. So the matrix element of the velocity operator can be rewritten as

$$\langle m|\hat{v}_\alpha|n\rangle = \sum_{ij\sigma\sigma'} \langle m|i, \sigma\rangle \langle i, \sigma|\hat{v}_\alpha|j, \sigma'\rangle \langle j, \sigma'|n\rangle. \quad (2.81)$$

We define a new operator is

$$\hat{V}_\alpha = \sum_{ij\sigma\sigma'} |i\rangle \langle i|\hat{v}_\alpha|j\rangle \langle j|. \quad (2.82)$$

We used a 3×3 square lattice to explain how the new operator works. The lattice is shown in the Figure 2.9. The spin index σ is not considered for a simple

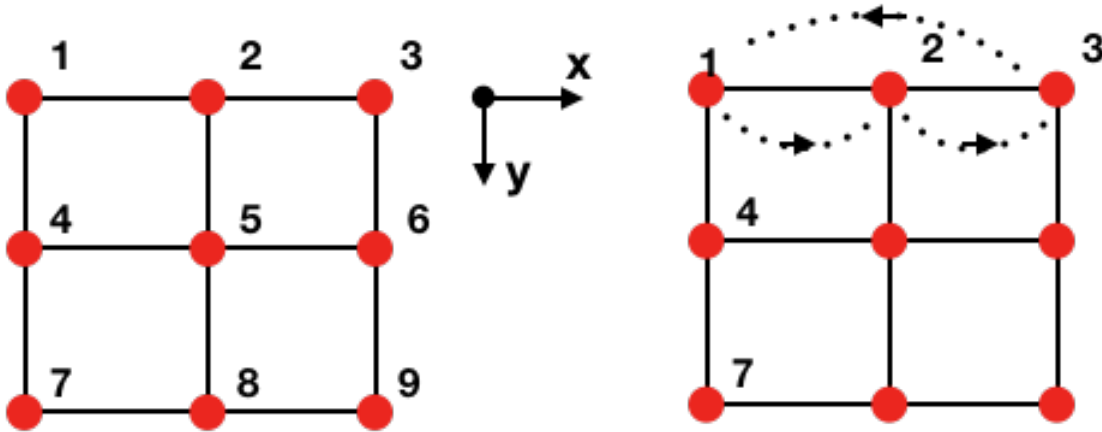


Figure 2.9: Left is the 3×3 square lattice. Right shows the periodical boundary condition.

explanation. The periodical boundary condition is employed, as shown in the right of Figure 2.9. At x -direction, we have $|1+\hat{x}\rangle = |2\rangle$, $|2+\hat{x}\rangle = |3\rangle$ and $|3+\hat{x}\rangle = |1\rangle$. Also at y -direction, we have $|1+\hat{y}\rangle = |4\rangle$, $|4+\hat{y}\rangle = |7\rangle$ and $|7+\hat{y}\rangle = |1\rangle$. The same rules are applied to other rows and columns. To the first row of the lattice,

$$\begin{aligned}
\hat{v}_{x\text{-row}1} &= it[R_{1x}(c_1^\dagger c_2 + c_1^\dagger c_3 - c_2^\dagger c_1 - c_3^\dagger c_1) \\
&\quad + R_{2x}(c_2^\dagger c_3 + c_2^\dagger c_1 - c_3^\dagger c_2 - c_1^\dagger c_2) \\
&\quad + R_{3x}(c_3^\dagger c_1 + c_3^\dagger c_2 - c_1^\dagger c_3 - c_2^\dagger c_3)] \\
&= it\{(R_{1x} - R_{2x})(c_1^\dagger c_2 - c_2^\dagger c_1)\} + [(R_{2x} - R_{3x})(c_2^\dagger c_3 - c_3^\dagger c_2)] \\
&\quad + [(R_{3x} - R_{1x})(c_3^\dagger c_1 - c_1^\dagger c_3)]\} \\
&= it[(R_2 - R_1)c_2^\dagger c_1 + (R_3 - R_2)c_3^\dagger c_2 + (R_1 - R_3)c_1^\dagger c_3] + h.c., \quad (2.83)
\end{aligned}$$

especially $R_{1x} - R_{3x} = -a$ where a is the lattice constant. So,

$$\hat{v}_{x\text{-row}1} = ita(c_2^\dagger c_1 + c_3^\dagger c_2 + c_1^\dagger c_3) + h.c.. \quad (2.84)$$

The operator \hat{V}_x for the 3×3 lattice is

$$\begin{aligned}
\hat{V}_x &= 2ita(|2\rangle\langle 1| + |3\rangle\langle 2| + |1\rangle\langle 3|) \text{ (first row of the lattice)} \\
&\quad + |5\rangle\langle 4| + |6\rangle\langle 5| + |4\rangle\langle 6| \text{ (second row of the lattice)} \\
&\quad + |8\rangle\langle 7| + |9\rangle\langle 8| + |7\rangle\langle 9|. \text{ (third row of the lattice)}. \quad (2.85)
\end{aligned}$$

The matrix form is

$$\hat{V}_x = 2ita \begin{pmatrix} A_{3 \times 3} & 0 & 0 \\ 0 & A_{3 \times 3} & 0 \\ 0 & 0 & A_{3 \times 3} \end{pmatrix}, \quad A_{3 \times 3} = \begin{pmatrix} 0 & 0 & 1 \\ 1 & 0 & 0 \\ 0 & 1 & 0 \end{pmatrix}. \quad (2.86)$$

Also we can achieve the \hat{V}_y of the lattice by the same procedure. Then adding the spin index back, we do numerical calculation with the spin textures in 2D chiral magnet with nonzero topological charge. For the purpose to study the topological Hall effect which just depends on the spin texture, we set a strong Hund's coupling $J_H/t = 1$. With the spin textures we chose, $\sigma_{xx} \gg \sigma_{xy}$ which can lead to $\rho_{xy} = \frac{\sigma_{xy}}{\sigma_{xx}^2}$. The results are shown in Figure 2.10. The low field one Figure 4. (a) shows, at

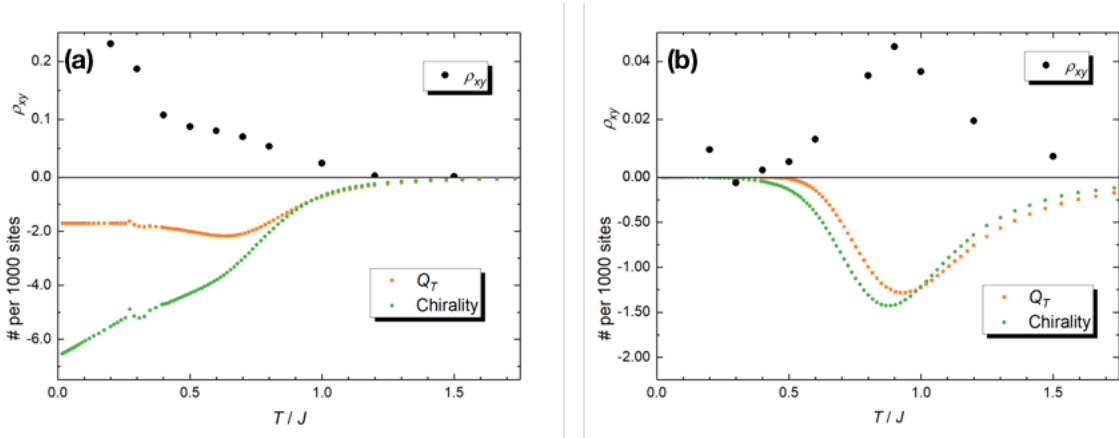


Figure 2.10: The relationship between Hall resistivity, topological charge and spin chirality, (a) low field, (b) high field.

low temperatures, the topological charge is flat and the absolute value of chirality decays with the increasing temperature, and also the Hall resistivity ρ_{xy} . The high field situation shows that the behaviors of topological charge and the chirality are similar. The peak value of ρ_{xy} is very close to the valley values of the spin chirality and topological charge. More work need to be done to distinguish the spin chirality and the topological charge and how they contribute to the Hall effect, especially in the magnetic system with superexchange antiferromagnetic coupling[121]. The program for calculating Hall conductivity written by Python is in the Appendix A.

2.6 Conclusion

In this chapter, the thermal average of topological charge in 2D chiral magnet has been studied through three different methods. In common belief, the paramagnetic phase is a totally random magnetic phase which is topological trivial. But through the discussions above, in thin film chiral magnets, the paramagnetism is not necessarily topologically trivial. In a region of high temperature which is out of the skyrmion crystal phase, the average of topological charge is nonzero although the snapshots show random spin textures. A significant upturn of the topological charge was observed outside the skyrmion crystal phase. This phenomenon is well understood by both analyzing thermal fluctuations in the atomic scales and field theoretical approach based on CP^1 formalism. As has been extensively studied in the skyrmion phase, non-zero topological charge would lead to the topological Hall effect, which was observed in the skyrmion crystal phase only[10, 79, 80]. The discrepancy between the topological Hall signal and distribution of the topological charge observed due to the itinerant nature of the magnetism in most chiral magnets under investigation. Close to or above the Curie temperature, the local magnetic moment in these magnets is significantly reduced. But all the calculation and analysis in this chapter is based on the assumption the local magnetic moment is constant which does not apply to the itinerant magnetism. Only insulating magnets such as Cu_2OSeO_3 , local magnetic moments are persistent at elevated temperatures. The magnon Hall effect has been observed in such insulating chiral magnets[40]. The transport properties of the insulating chiral magnets have a lot of interesting aspects to be discovered, which may be closely relevant to the nontrivial topology in the materials.

CHAPTER III

Topological charge in 3D chiral magnets

In Chapter II, the thermal average of topological charge in 2D chiral magnets has been investigated. There is nonzero topological charge out of the skyrmion crystal phase. If looking into the past experiments about the chiral magnets, there was no one done on a monolayer sample. The small angle neutron scattering(SANS) was performed on the bulk MnSi[10]. The skyrmion crystal phase was detected on the surface of the bulk. The experiments about $\text{Fe}_{1-x}\text{Co}_x\text{Si}$ [39] and Cu_2OSeO_3 [15] were a thin film with tens of nanometers thickness. Even with this thickness, the sample cannot be treated as a 2D system. How does the topological charge behave when there the sample has finite thickness motivates us to do further analysis in this session.

3.1 Monte Carlo simulation

3.1.1 Methodology

The Monte Carlo simulation is performed on a 3D cubic lattice of classical spin model. The Hamiltonian of the chiral magnet with external magnetic field is

$$H = \sum_{\langle lm \rangle} (-J \mathbf{S}_l \cdot \mathbf{S}_m + \mathbf{D}_{lm} \cdot \mathbf{S}_l \times \mathbf{S}_m) - B \sum_l S_l^z, \quad (3.1)$$

where $\mathbf{S}_l = S\mathbf{n}_l$ is the spin vector on site l and $|\mathbf{n}_l| = \frac{|\mathbf{S}_l|}{S} = 1$. $\langle ij \rangle$ means site i and j are the nearest neighbors. In 3D model, the DM interaction is

$$\mathbf{D}_{l,l+\hat{e}} = D\hat{e}, \quad (3.2)$$

where $\hat{e} = \hat{x}, \hat{y}, \hat{z}$. The procedure is similar in 2D situation. Here, we just used Metropolis method[105] to make the Markov chain of spin configurations. The over-relaxation method was not employed here because we used graphics processing unit(GPU) programming[122] to accelerate the calculation. The over-relaxation method was used to make the results converge more rapidly than using many spin configurations for the average value. In GPU programming, the structure of the storage units is very suitable for writing and reading data repeatedly quickly. And GPU can make the summation and average operations much more quickly. It makes employing larger sizes of spin lattices and averaging more data points at unique temperatures become acceptable. With the help of GPU, the over-relaxation method is not required.

Triangulation of the lattice at $x - y$ plane is performed to calculate the solid angle surrounded by the three spins. The Berg formula is used to calculate the solid angle, which has been mentioned in the last chapter. Here, we do summation of all the topological charges at every layer, then get the average, which is depicted in Figure 3.1.

Here, we just focus on the signal of the topological charge. A $16 \times 16 \times 16$ cubic lattice with periodic boundary condition is employed.

3.1.2 Results

With different combinations of DM interactions and external magnetic fields, We have the results shown in Figure 3.2. The similar curve fitting in 2D can be

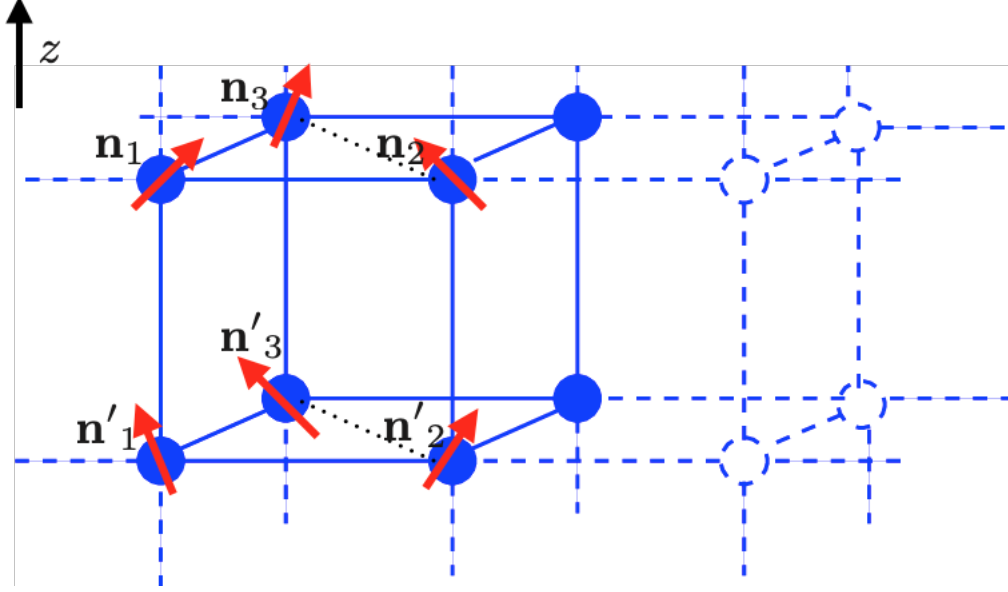


Figure 3.1: Triangulation of the cubic lattice

done to investigate the relation between the thermal average topological charge and DM interaction with fixed magnetic field at a fixed high temperature, as well as the relation between the thermal average topological charge and magnetic field with fixed DM interaction.

Another interesting topic of 3D chiral magnets is the thickness dependence. In the experiment[103], SrRuO₃ thin film samples with different number of layers have been employed to measure the topological Hall effects. It motivates us to investigate the topological charge with different number of layers. We employed the lattice with the sizes $32 \times 32 \times N_z$ ($N_z = 1, 2, 3, 4, 8, 16, 32$), the $x - y$ plane is periodic boundary condition, z direction is open boundary condition which mimics the experimental environment. The results have been shown in Figure 3.3. The valley values of the topological charge decrease and the positions of valleys move from low temperature to high temperature with the increasing number of layers. The positions of the valleys may relate to the finite size effect. We employed the finite size scaling to investigate this effect.

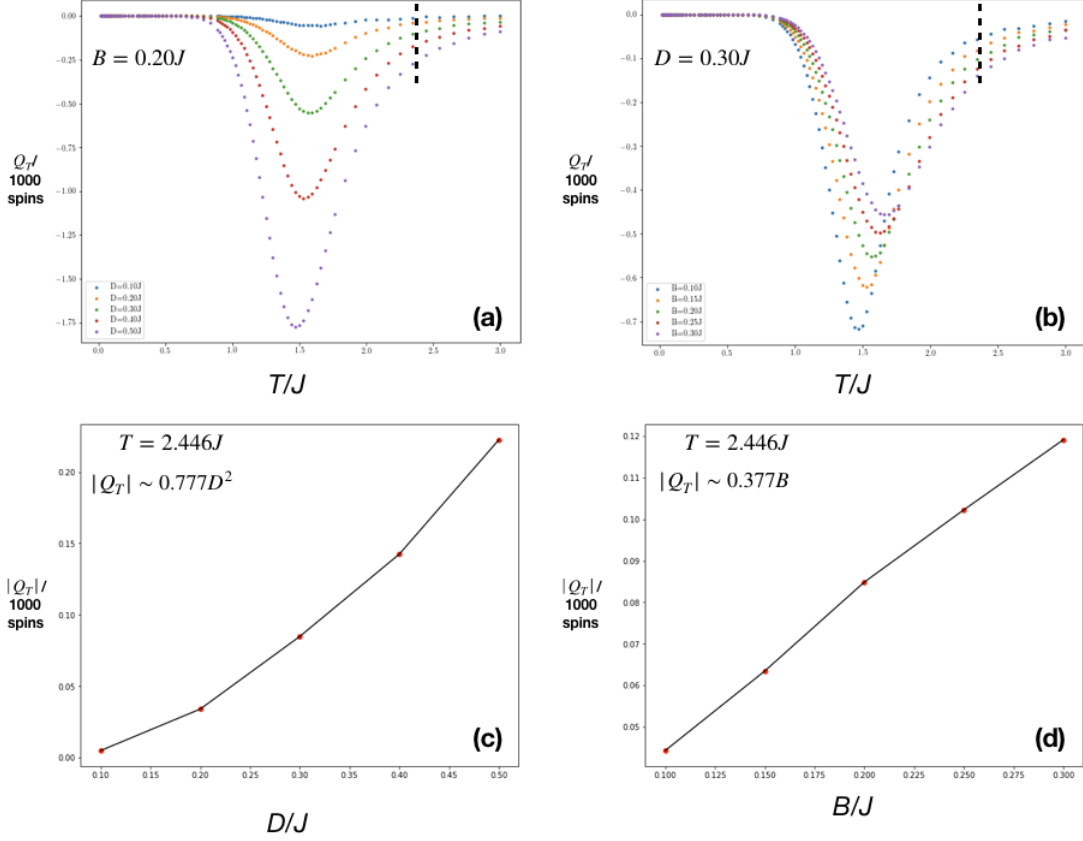


Figure 3.2: (a) Q_T vs T/J , fixed $B/J = 0.2$. (b) Q_T vs T/J , fixed $D/J = 0.3$.
 . (c) At $T = 2.446J$, relationship between Q_T and D . (c) At $T = 2.446J$, relationship between Q_T and B .

3.1.3 Finite size scaling

$B = 0.2J$ and $D = 0.4J$ is chosen to investigate the finite size effect. The specific heats of different layers need to be calculated for the finite size scaling purpose[123]. The Figure 3.4 shows the specific heats (a) and the topological charges (b) with different N_z . The package pyfssa written by Python was used to do the finite size scaling. The finite size scaling makes the curves of the specific heats collapse together. The scaling happens by $c_v L_z^{-\zeta/\nu}$ vs. $[(T - T_c)L_z^{1/\nu} + T_c]/J$ in which T_c is the critical temperature searching by the finite size scaling. The topological charge is size effect free, means no need to rescale. The diagram after finite size scaling has been shown in Figure 3.5. The best values of the rescaling

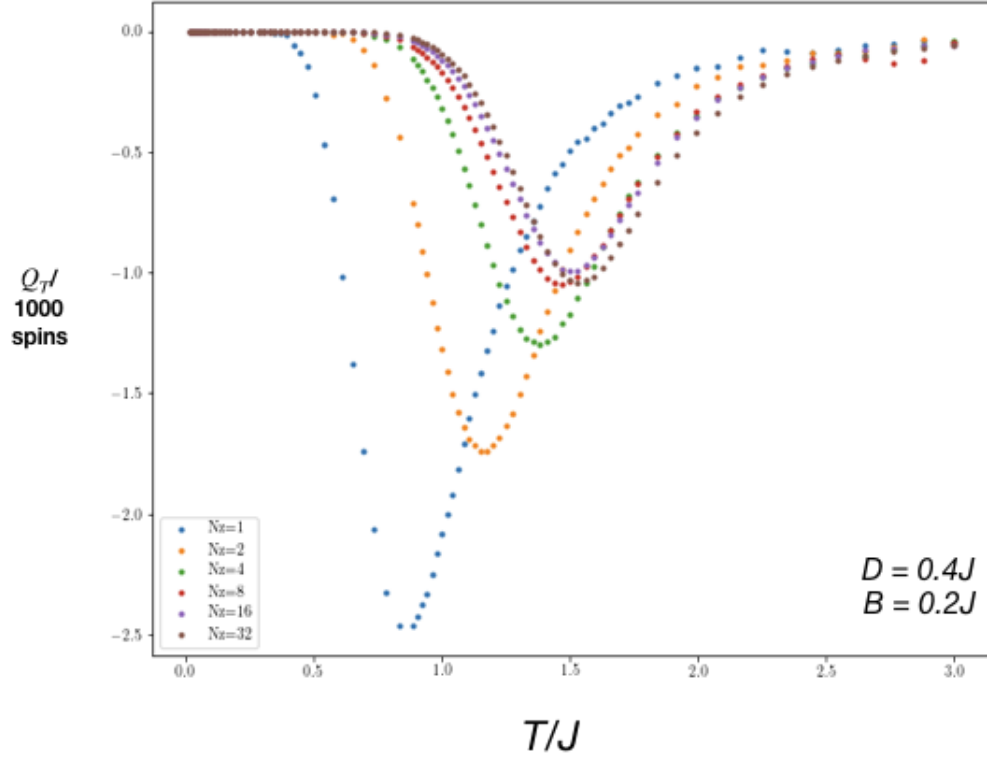


Figure 3.3: Topological charge versus T/J .

parameters are $T_c = 2.455 \pm 0.003$, $\nu = 11.857 \pm 0.014$ and $\zeta = 0.761 \pm 0.001$. The specific heats collapse together well. The valleys are at the same position. It proves the positions of the valleys are affected by the finite size effect. But till now, there is not a good explanation of the finite values of topological charge at high temperature.

3.2 The field theory approach

As the same as 2D situation, the field-theory approach has been performed to calculate topological charge lay on the $x - y$ plane which is perpendicular to the external magnetic field h_z .

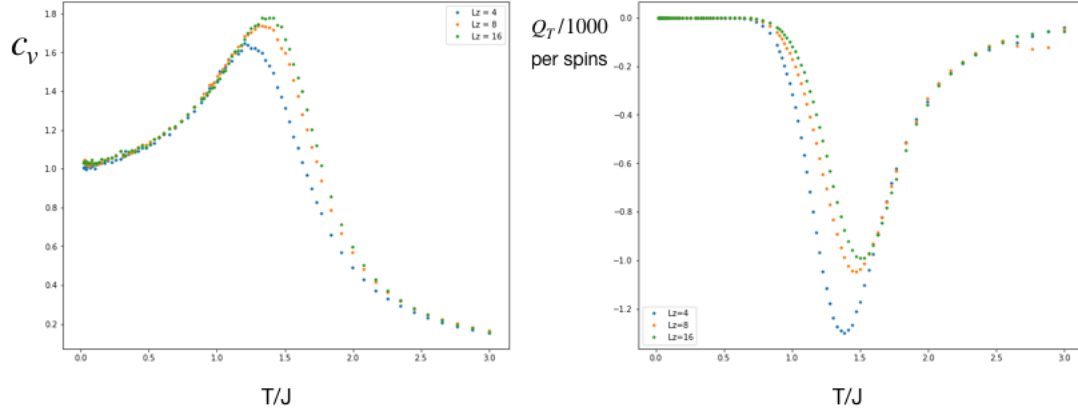


Figure 3.4: (a) Specific heat c_v versus T/J . (b) Average Topological charge versus T/J .

3.2.1 The model and Hamiltonian

The discrete Hamiltonian of cubic spin lattice has been shown in Eqn.(3.1). The Heisenberg interaction term can be expanded as the same as 2D situation but $\nabla = (\partial_x, \partial_y, \partial_z)$. The DM interaction in 3D can be expanded as The DM

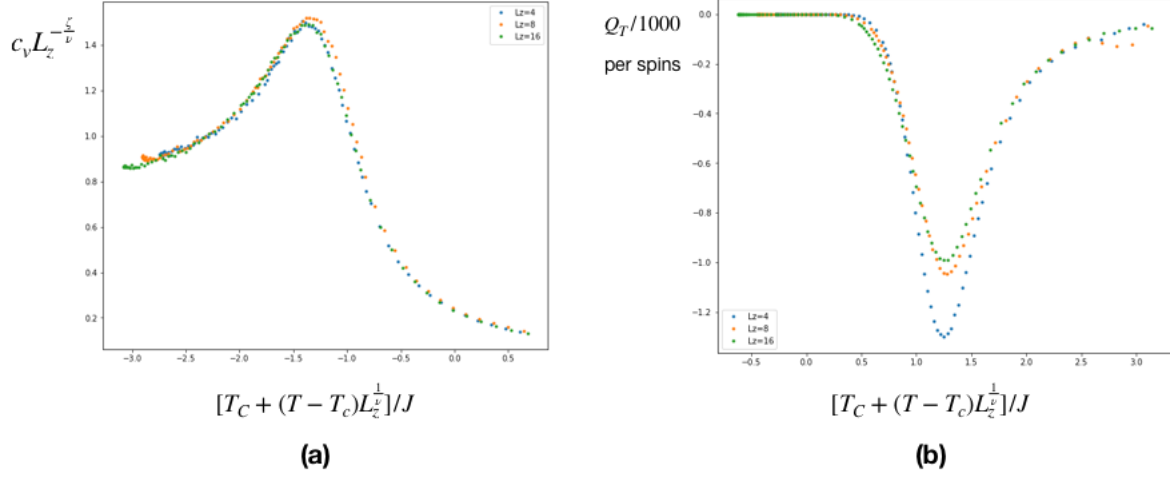


Figure 3.5: Rescaling specific heat $c_v L_z^{-\xi/\nu}$ versus $[(T - T_c)L_z^{1/\nu} + T_c]$ (a) Average Topological charge versus $[(T - T_c)L_z^{1/\nu} + T_c]$.

interaction term is

$$\begin{aligned}
\sum_e (\mathbf{S}_l \times \mathbf{S}_{l+\hat{e}}) \cdot \hat{e} &\approx \sum_e a (\mathbf{S}_l \times \partial_e \mathbf{S}_l) \cdot \hat{e} \\
&= a S^2 \left(\begin{array}{c} \left| \begin{array}{ccc} 1 & 0 & 0 \\ n_x & n_y & n_z \\ \partial_x n_x & \partial_x n_y & \partial_x n_z \end{array} \right| \\ + \left| \begin{array}{ccc} 0 & 1 & 0 \\ n_x & n_y & n_z \\ \partial_y n_x & \partial_y n_y & \partial_y n_z \end{array} \right| \\ + \left| \begin{array}{ccc} 0 & 0 & 1 \\ n_x & n_y & n_z \\ \partial_z n_x & \partial_z n_y & \partial_z n_z \end{array} \right| \end{array} \right) \\
&= a S^2 (n_y \partial_x n_z - n_z \partial_x n_y + n_z \partial_y n_x - n_x \partial_y n_z \\
&\quad + n_x \partial_z n_y - n_y \partial_z n_x) \\
&= a S^2 \mathbf{n} \cdot (\nabla \times \mathbf{n}). \tag{3.3}
\end{aligned}$$

So the Hamiltonian in continuum limit is

$$H = \Lambda \int d^3r \left[\frac{\bar{J}}{2} (\partial_i \mathbf{n}) \cdot (\partial_i \mathbf{n}) + \bar{D} \mathbf{n} \cdot (\nabla \times \mathbf{n}) - \bar{B} n_z \right]. \quad (3.4)$$

where $i = x, y, z$, $\bar{J} = JS^2$, $\bar{D} = \frac{D^2 S}{a}$ and $\bar{B} = \frac{BS}{a^2}$. The parameters are the same as 2D situation. By employing CP^1 projection, we have

$$H_0 = \Lambda \int d^3r \{ 2\bar{J} |(\partial_i - ia_i + i\kappa\sigma_i)\mathbf{z}|^2, \quad (3.5)$$

without the Zeeman coupling term, where a_i is the emergent gauge field and $\frac{\bar{D}}{2J}$.

And

$$H_{Zeeman} = -\Lambda \int d^3r h \mathbf{z}^\dagger \sigma_z \mathbf{z}, \quad (3.6)$$

where $h = \frac{\bar{B}}{2J}$. Extending CP^1 model to $CP^{\mathcal{N}-1}$ model, the partition function is

$$\mathcal{Z} = \int \mathcal{D}\mathbf{z}^\dagger \mathcal{D}\mathbf{z} \prod_{i=1}^3 \mathcal{D}a_i \exp\left(-\frac{H}{T}\right) \delta\left(\mathbf{z}^\dagger \mathbf{z} - \frac{\mathcal{N}}{2}\right). \quad (3.7)$$

By replacing $\delta(\mathbf{z}^\dagger \mathbf{z} - \frac{\mathcal{N}}{2})$ by $\int d\lambda \exp[i\lambda(\mathbf{z}^\dagger \mathbf{z} - 1)]$, the partition function is

$$\begin{aligned} \mathcal{Z} &= \int \mathcal{D}\mathbf{z}^\dagger \mathcal{D}\mathbf{z} \prod_{i=1}^3 \mathcal{D}a_i \mathcal{D}\lambda \\ &\times \exp\left(-\frac{2\bar{J}\Lambda}{T} \int d^3r [(\partial_i - ia_i + i\kappa\sigma_i)\mathbf{z}]^2 - i \int d^3r \lambda (\mathbf{z}^\dagger \mathbf{z} - \frac{\mathcal{N}}{2})\right). \end{aligned} \quad (3.8)$$

After rescaling $\mathbf{z} \rightarrow \sqrt{\frac{2J\Lambda}{T}} \mathbf{z}$, $f = \frac{T}{J}$ and $\lambda \rightarrow \frac{f}{2}\lambda$, The partition function has a simpler form,

$$\begin{aligned} \mathcal{Z} &= \prod_{i=1}^3 \int \mathcal{D}\mathbf{z}^\dagger \mathcal{D}\mathbf{z} \mathcal{D}a_i \mathcal{D}\lambda \exp\left[-\int d^3r [(\partial_i - ia_i + i\kappa\sigma_i)\mathbf{z}]^2 - i\lambda(\mathbf{z}^\dagger \mathbf{z} - \frac{\mathcal{N}\lambda}{f})\right] \\ &\times \exp\left[-\int d^3r [(\partial_i - ia_i + i\kappa\sigma_i)\mathbf{z}]^2 - i\lambda(\mathbf{z}^\dagger \mathbf{z} - \frac{\mathcal{N}\lambda}{f})\right]. \end{aligned} \quad (3.9)$$

3.2.2 Mean field approximation

The partition function has the form $\mathcal{Z} = \prod_{i=1}^3 \int \mathcal{D}a_i \mathcal{D}\lambda \exp(-S_{eff}[a_i, \lambda])$ after integrating out the field \mathbf{z} and

$$S_{eff}[a_i, \lambda] = C' + \text{Tr} \int d^3r \{ \log[-(\partial_i - ia_i + i\kappa\sigma_i)^2 + i\lambda] - \frac{\mathcal{N}\Lambda}{f} i\lambda \}. \quad (3.10)$$

In momentum space, the mean field approximation $i\langle\lambda\rangle = \bar{\lambda}$, $\langle a_i \rangle = 0$,

$$S_{eff}[0, \bar{\lambda}] = C'' + \sum_k \log[(k^2 + \bar{\lambda} + 3\kappa^2)^2 - 4\kappa^2 k^2] - \frac{\mathcal{N}\Lambda L^3 \bar{\lambda}}{f}. \quad (3.11)$$

By replacing \sum_k by $L^3 \int \frac{d^3k}{(2\pi)^3}$ then solving the saddle point equation $\frac{\delta S_{eff}}{\delta \lambda} = 0$.

$$\begin{aligned} L^3 \int \frac{d^3k}{(2\pi)^3} \frac{2(k^2 + \bar{\lambda} + 3\kappa^2)}{(k^2 + \bar{\lambda} + 3\kappa^2)^2 - 4\kappa^2 k^2} &= \frac{\mathcal{N}\Lambda L^3}{f} \\ \int \frac{k^2 dk d\Omega}{(2\pi)^3} \left[\frac{1}{(k^2 - 2\kappa k + \bar{\lambda} + 3\kappa^2)} + \frac{1}{(k^2 + 2\kappa k + \bar{\lambda} + 3\kappa^2)} \right] &= \frac{\mathcal{N}\Lambda}{f} \\ \int \frac{k^2 dk}{2\pi^2} \left[\frac{1}{(k - \kappa)^2 + \bar{\lambda} + 2\kappa^2} + \frac{1}{(k + \kappa)^2 + \bar{\lambda} + 2\kappa^2} \right] &= \frac{\mathcal{N}\Lambda}{f}. \end{aligned} \quad (3.12)$$

Setting $m_0^2 = \bar{\lambda} + 2\kappa^2$, and we assume $\kappa \rightarrow 0$ then use the Pauli-Villars regularization,

$$\begin{aligned} \int \frac{d^3k}{(2\pi)^3} \frac{1}{k^2 + m_0^2} &\rightarrow \int \frac{d^3k}{(2\pi)^3} \frac{1}{k^2 + m_0^2} - \frac{1}{k^2 + \Lambda^2} = \frac{\mathcal{N}\Lambda}{2f} \\ \int_0^\infty dk - m_0^2 \int_0^\infty \frac{dk}{k^2 + m_0^2} - \int_0^\infty dk + \Lambda^2 \int_0^\infty \frac{dk}{k^2 + \Lambda^2} &= \frac{\mathcal{N}\pi^2 \Lambda}{f} \\ \frac{\pi}{2}(\Lambda - m_0) &= \frac{\mathcal{N}\pi^2 \Lambda}{f} \\ m_0 &= \left(1 - \frac{4\pi}{f}\right)\Lambda \\ m_0^2 &= \left(1 - \frac{4\pi}{f}\right)^2 \Lambda^2. \end{aligned} \quad (3.13)$$

We can see at high temperature m_0 is comparable with Λ . With the condition $\kappa \ll 1$, we can neglect it when using the mean field theory to estimate the value of m_0^2 .

3.2.3 Perturbative Calculation

In momentum space, the non-perturbative part S_0 and perturbative parts S_{i1} , S_{i2} are

$$S_0 = \sum_k \mathbf{z}_k^\dagger (k^2 + m_0^2 - 2\kappa k_i \sigma_i) \mathbf{z}_k, \quad (3.14)$$

$$S_{i1} = - \sum_{k,q} \mathbf{z}_{k+\frac{q}{2}}^\dagger (2k_i a_{i,q} + 2\kappa a_{i,q} + h_q \sigma_z) \mathbf{z}_{k-\frac{q}{2}}, \quad (3.15)$$

$$S_{i2} = \sum_{k,q,p} \mathbf{z}_k^\dagger \mathbf{z}_q a_{i,p} a_{i,k-p-q}. \quad (3.16)$$

The propagator of \mathbf{z} field can be read as $\langle \mathbf{z}_k \mathbf{z}_k^\dagger \rangle = \frac{1}{k^2 + m_0^2 - 2\kappa k_i \sigma_i}$. The relevant Feynman diagrams are in Figure 3.6. The propagator is $G_{0,z}(k) = \langle \mathbf{z}_k \mathbf{z}_k^\dagger \rangle = \frac{1}{k^2 + m_0^2 - 2\kappa k_i \sigma_i}$. The relevant Feynman rules and diagrams are in Figure 3.6. The

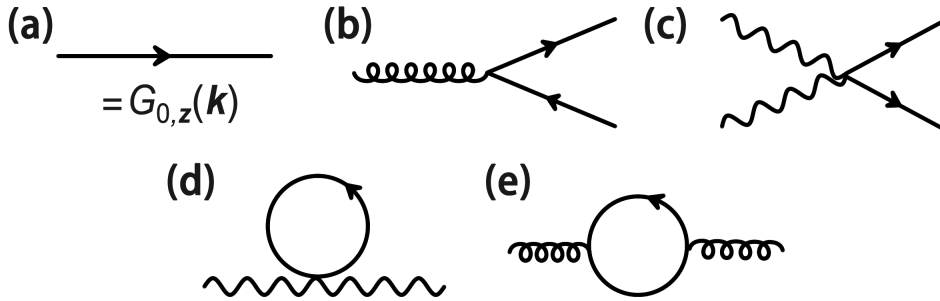


Figure 3.6: Feynman rules and Feynman diagrams

effective action of Figure 3.6(d) diagram is

$$\begin{aligned}
S_d &= L^6 \text{Tr} \int \frac{d^3 k d^3 q}{(2\pi)^3} \frac{a_{i,q} a_{i,-q}}{k^2 + m_0^2 - 2\kappa k_i \sigma_i} \\
&= L^6 \int \frac{d^3 k d^3 q}{(2\pi)^3} \frac{2a_{i,q} a_{i,-q}}{k^2 + m_0^2} + \frac{4\kappa^2 k^2 a_{i,q} a_{i,-q}}{(k^2 + m_0^2)^2} + \mathcal{O}(\kappa^4). \tag{3.17}
\end{aligned}$$

Here we just ignore the κ^2 and higher order, by employing Pauli-Villars regularization,

$$\begin{aligned}
\int \frac{d^3 k}{(2\pi)^3} \frac{1}{k^2 + \bar{\lambda}} &\rightarrow \int \frac{d^3 k}{(2\pi)^3} \left(\frac{1}{k^2 + m_0^2} - \frac{1}{k^2 + \Lambda^2} \right) \\
&= \frac{1}{4\pi} (\Lambda - m_0). \tag{3.18}
\end{aligned}$$

So that,

$$S_d = \frac{L^6}{2\pi} (\Lambda - m_0) \int \frac{d^3 q}{(2\pi)^3} a_{i,q} a_{i,-q}. \tag{3.19}$$

In Fig(e),

$$\begin{aligned}
S_e &= -\frac{L^6}{2!} \int \frac{d^3k d^3q}{(2\pi)^6} \\
&\times \langle 2\mathbf{z}_{k+\frac{q}{2}}^\dagger (-k_i a_{i,q} - \kappa a_{i,q} \sigma_i - \frac{h_q}{2} \sigma_3) \mathbf{z}_{k-\frac{q}{2}} \\
&\times 2\mathbf{z}_{k-\frac{q}{2}}^\dagger (-k_j a_{j,-q} - \kappa a_{j,-q} \sigma_j - \frac{h_{-q}}{2} \sigma_3) \mathbf{z}_{k+\frac{q}{2}} \rangle \\
&= -2L^6 \text{Tr} \int \frac{d^3k d^3q}{(2\pi)^6} \frac{1}{(k+\frac{q}{2})^2 + m_0^2 - 2\kappa(k+\frac{q}{2})_{i'} \sigma_{i'}} \\
&\times [k_i a_{i,-q} + \kappa a_{i,-q} \sigma_i + (\kappa a_{3,-q} + \frac{h_{-q}}{2}) \sigma_3] \\
&\times \frac{1}{(k-\frac{q}{2})^2 + m_0^2 - 2\kappa(k-\frac{q}{2})_{j'} \sigma_{j'}} [k_j a_{j,q} + \kappa a_{j,q} \sigma_j + \sigma_3] \\
&= -2L^6 \int \frac{d^3k d^3q}{(2\pi)^6} \left[\frac{1}{(k+\frac{q}{2})^2 + m_0^2} + \frac{2\kappa(k+\frac{q}{2})_{i'} \sigma_{i'}}{[(k+\frac{q}{2})^2 + m_0^2]^2} + \mathcal{O}(\kappa^2) \right] \\
&\times [k_i a_{i,-q} + \kappa a_{i,-q} \sigma_i + (\kappa a_{3,-q} + \frac{h_{-q}}{2}) \sigma_3] \left[\frac{1}{(k-\frac{q}{2})^2 + m_0^2} \right. \\
&+ \left. \frac{2\kappa(k-\frac{q}{2})_{j'} \sigma_{j'}}{[(k-\frac{q}{2})^2 + m_0^2]^2} + \mathcal{O}(\kappa^2) \right] [k_j a_{j,q} + \kappa a_{j,q} \sigma_j + (\kappa a_{3,q} + \frac{h_q}{2}) \sigma_3] \\
&+ \frac{2\kappa(k+\frac{q}{2})_{i'} \sigma_{i'}}{[(k+\frac{q}{2})^2 + m_0^2]^2} [k_i a_{i,-q} + \kappa a_{i,-q} \sigma_i + (\kappa a_{3,-q} + \frac{h_{-q}}{2}) \sigma_3] \frac{(k_j a_{j,q} + \kappa a_{j,q} \sigma_j + \frac{h_q}{2} \sigma_3)}{(k-\frac{q}{2})^2 + m_0^2} \\
&+ \mathcal{O}(\kappa^2)] \tag{3.20}
\end{aligned}$$

We do not consider the $\kappa^2 a_i^2$ term with the same reason of 2D situation in S_b .

Also h^2 term is neglected because it decouples with a_i . We employ Feynman parametrization to work out the integrals,

$$S_{e1} = -4L^6 \int \frac{d^3q d^3k}{(2\pi)^6} \int_0^1 dx \frac{(k_i a_i)^2}{\{x[(k+\frac{q}{2})^2 + m_0^2] + (1-x)[(k-\frac{q}{2})^2 + m_0^2]\}^2} \tag{3.21}$$

with

$$\begin{aligned}
A &= \int \frac{d^3k}{(2\pi)^3} \int_0^1 dx \frac{(k_i a_i)^2}{[k^2 + \frac{q^2}{4} + m_0^2 + 2(x - \frac{1}{2})k \cdot q]^2} \\
&= \int_0^1 dx \int \frac{d^3k}{(2\pi)^3} \frac{(k_i a_i)^2}{\{[k + (x - \frac{1}{2})q]^2 + \frac{q^2}{4} + m_0^2 - (x - \frac{1}{2})^2 q^2\}^2} \\
&= \int_0^1 dx \int \frac{d^3l}{(2\pi)^3} \frac{\{[l - (x - \frac{1}{2})q]_i a_i\}^2}{[l^2 + m_0^2 + x(1-x)q^2]^2} \tag{3.22}
\end{aligned}$$

$$\tag{3.23}$$

where $l = k + (x - \frac{1}{2})q$ and define $\Delta = m_0^2 + x(1-x)q^2$. A is divided into two parts

$$A = A_1 + A_2 \tag{3.24}$$

$$\begin{aligned}
A_1 &= \int_0^1 dx \int \frac{d^3l}{(2\pi)^3} \frac{(l_i a_i)^2}{(l^2 + \Delta)^2} \\
&= \int_0^1 dx \int d\Omega \int_0^\infty \frac{l^2 dl}{(2\pi)^3} \frac{1}{3} \frac{l^2 a_i a_i}{(l^2 + \Delta)^2} \\
&= \frac{1}{6\pi^2} \int_0^1 dx \int_0^\infty \frac{l^4 dl}{(l^2 + \Delta)^2} \mathbf{a}^2 \tag{3.25}
\end{aligned}$$

$$\begin{aligned}
A_1 \rightarrow A'_1 &= \frac{1}{6\pi^2} \int_0^1 dx \int_0^\infty \left[\frac{l^4 dl}{(l^2 + \Delta)^2} - \frac{l^4 dl}{(l^2 + \Lambda^2)^2} \right] a_i^2 \\
&= -\frac{1}{4\pi^2} \int_0^1 dx \frac{\pi}{2} (\sqrt{\Delta} - \Lambda) a_i^2 \\
&= -\frac{1}{8\pi} \int_0^1 dx (\sqrt{m_0^2 + x(1-x)q^2} - \Lambda_{PV}) a_i^2 \\
&= -\frac{1}{8\pi} \int_0^1 dx \left(m_0 - \Lambda_{PV} - \frac{x(1-x)q^2}{2m_0} \right) a_i^2 + \mathcal{O}(q^4) \\
&= -\frac{1}{8\pi} \left(m_0 - \Lambda + \frac{q^2 \mathbf{a}^2}{12m_0} \right) + \mathcal{O}(q^4) \tag{3.26}
\end{aligned}$$

$$\begin{aligned}
A_2 &= \int_0^1 dx \int \frac{d^3 l}{(2\pi)^3} \frac{(x - \frac{1}{2})^2 (q_i a_i)^2}{(l^2 + \Delta)^2} \\
&= \frac{1}{2\pi^2} \int_0^1 dx \int_0^\infty l^2 dl \frac{(x - \frac{1}{2})^2 (q_i a_i)^2}{(l^2 + \Delta)^2} \\
&= \frac{1}{2\pi^2} \int_0^1 dx \left[\int_0^\infty \left[\frac{dl}{l^2 + \Delta} - \frac{\Delta dl}{(l^2 + \Delta)^2} \right] (x - \frac{1}{2})^2 (q_i a_i)^2 \right] \\
&= \frac{1}{2\pi^2} \int_0^1 dx \frac{\pi}{4} \frac{1}{\sqrt{\Delta}} (x - \frac{1}{2})^2 (q_i a_i)^2 \\
&= \frac{1}{96\pi} \frac{1}{m_0} (q_i a_i)^2 + \mathcal{O}(q^4) \tag{3.27}
\end{aligned}$$

$$A'_1 + A_2 = -\frac{1}{8\pi} (m_0 - \Lambda) \mathbf{a}^2 - \frac{1}{96\pi m_0} [q^2 \mathbf{a}^2 - (q_i a_i)^2] + \mathcal{O}(q^4) \tag{3.28}$$

$$\begin{aligned}
S_{e1} &= \frac{L^3}{2\pi} \int \frac{d^3 q}{(2\pi)^3} (m_0 - \Lambda) + \frac{1}{12m_0} [q^2 \mathbf{a}^2 - (q_i a_i)^2] + \mathcal{O}(q^4) \\
&= \frac{L^6}{2\pi} \int \frac{d^3 q}{(2\pi)^3} (m_0 - \Lambda_{PV}) + \frac{1}{12m_0} [a_i q^2 a_i - q_i a_i q_j a_j] + \mathcal{O}(q^4) \tag{3.29}
\end{aligned}$$

$$\begin{aligned}
S_d + S_{e1} &= \frac{L^6}{24\pi m_0} \int \frac{d^3 q}{(2\pi)^3} [a_i q^2 a_i - q_i a_i q_j a_j] + \mathcal{O}(q^4) \\
&= \frac{L^3}{24\pi m_0} \int d^3 r [-a_i \partial^2 a_i + a_i \partial_i \partial_j a_j] + \mathcal{O}(q^4) \\
&= \frac{L^3}{48\pi m_0} \int d^3 r f_{ij} f_{ij} + \mathcal{O}(\partial^4) = \frac{L^3}{24\pi m_0} \int d^3 r \mathbf{b}^2 + \mathcal{O}(\partial^4) \tag{3.30}
\end{aligned}$$

where $f_{ij} = \partial_i a_j - \partial_j a_i$. Then

$$\begin{aligned}
S_{e2} = S_{hb} &= -4L^6 \int \frac{d^3 k d^3 q}{(2\pi)^6} \left[\frac{i\kappa^2 \varepsilon_{ij3} (k + \frac{q}{2})_i a_{j,-q} h_q + i\kappa^2 \varepsilon_{i3j} (k + \frac{q}{2})_i h_{-q} a_{j,q}}{[(k + \frac{q}{2})^2 + m_0^2]^2 [(k - \frac{q}{2})^2 + m_0^2]} \right. \\
&\quad \left. + \frac{i\kappa^2 \varepsilon_{ij3} a_{i,-q} (k - \frac{q}{2})_j h_q + i\kappa^2 \varepsilon_{3ij} h_{-q} (k - \frac{q}{2})_i a_{j,q}}{[(k + \frac{q}{2})^2 + m_0^2][(k - \frac{q}{2})^2 + m_0^2]^2} \right] + \mathcal{O}(\kappa^3) \\
&= 4\kappa^2 L^6 \int \frac{d^3 k d^3 q}{(2\pi)^6} \left\{ \frac{-4\mathbf{k} \cdot \mathbf{q} (i\varepsilon_{3ij}) k_i (a_{j,-q} h_q - a_{j,q} h_{-q})}{[(k + \frac{q}{2})^2 + m_0^2]^2 [(k - \frac{q}{2})^2 + m_0^2]^2} \right. \\
&\quad \left. + \frac{2(k^2 + \frac{q^2}{4} + m_0^2)(b_q h_{-q} + b_{-q} h_q)}{[(k + \frac{q}{2})^2 + m_0^2]^2 [(k - \frac{q}{2})^2 + m_0^2]^2} \right\} \\
&= 8\kappa^2 L^6 \int_0^1 dx \int \frac{d^3 l d^3 q}{(2\pi)^6} \frac{h_{-q} b_q (\frac{q^2}{4} + m_0^2)}{(l^2 + \Delta)^4} \\
&= 8\kappa^2 L^6 \int_0^1 dx \int \frac{l^2 dl}{2\pi^2} \int \frac{d^3 q}{(2\pi)^3} \frac{(\frac{q^2}{4} + m_0^2) h_{-q} b_q}{(l^2 + \Delta)^4} \\
&\rightarrow 8\kappa^2 L^6 \int_0^1 dx \int \frac{l^2 dl}{2\pi^2} \int \frac{d^3 q}{(2\pi)^3} \left(\frac{1}{(l^2 + \Delta)^4} - \frac{1}{(l^2 + \Lambda^2)^4} \right) \left(\frac{q^2}{4} + m_0^2 \right) h_{-q} b_q \\
&\frac{4\kappa^2 L^6}{\pi^2} \int_0^1 dx \int \frac{d^3 q}{(2\pi)^3} \frac{\pi}{32} \left(\frac{1}{m_0^5} - \frac{1}{\Lambda^5} \right) \left(\frac{q^2}{4} + m_0^2 \right) h_{-q} b_q \\
&= \frac{\kappa^2 L^6}{8\pi} \int \frac{d^3 q}{(2\pi)^3} \left(\frac{1}{m_0^3} - \frac{m_0^2}{\Lambda^5} \right) h_{-q} b_q + \mathcal{O}(q^2) \tag{3.31}
\end{aligned}$$

Here, we also add the term $\frac{1}{l^2 + \Lambda^2}$ even the integral is not divergent because we need to consider in the system there exists the momentum cut-off Λ which is proportional to $1/a$, a is the lattice constant. We use the Pauli-Villars regularization $\int_0^\infty f(k, m_0) - f(k, \Lambda)$ to replace $\int_0^\Lambda f(k, m_0)$. In real space,

$$S_{b^2} + S_{hb} = \frac{L^3}{\pi} \int d^3 r \frac{1}{24m_0} \mathbf{b}^2 + \frac{\kappa^2 h}{8} \left(\frac{1}{m_0^3} - \frac{m_0^2}{\Lambda^5} \right) b_z + \dots \tag{3.32}$$

The saddle point is easy to get $\langle b_z \rangle = -\frac{3}{2}\kappa^2 h (\frac{1}{m_0^2} - \frac{m_0^3}{\Lambda^5})$ and pluge in $m_0 = \Lambda(1 - \frac{4\pi}{f})$ at high temperature . So,

$$\langle b_z \rangle = -\frac{3}{2} \frac{\kappa^2 h}{\Lambda^2} \left[\frac{1}{(1 - \frac{4\pi}{f})^2} - (1 - \frac{4\pi}{f})^3 \right]. \quad (3.33)$$

Then we expand it to the order of $\frac{1}{f^3}$.

$$\begin{aligned} \langle b_z \rangle &= -\frac{3\kappa^2 h}{2\Lambda^2} \left[\frac{20\pi}{f} + \frac{320\pi^3}{f^3} + \mathcal{O}\left(\frac{1}{f^4}\right) \right] \\ &= -\frac{30\pi\kappa^2 h}{\Lambda^2} \left[\frac{1}{f} + \frac{16\pi^2}{f^3} + \mathcal{O}\left(\frac{1}{f^4}\right) \right]. \end{aligned} \quad (3.34)$$

The average of the topological charge in the plane perpendicular to the external magnetic field is

$$\begin{aligned} \langle Q \rangle &= \frac{L^2}{4\pi} \langle b_z \rangle = -\frac{1}{4\pi} a^2 \frac{30\pi}{\Lambda^2} \left(\frac{D}{2Ja}\right)^2 \left(\frac{B}{2Ja^2}\right) \frac{J}{T} \left[1 + \left(\frac{4\pi J}{T}\right)^2\right] + \mathcal{O}\left(\left(\frac{J}{T}\right)^4\right) \\ &= -\frac{15}{16} N^2 \frac{BD^2}{J^2 T} \left[1 + \left(\frac{4\pi J}{T}\right)^2\right] + \mathcal{O}\left(\left(\frac{J}{T}\right)^4\right), \end{aligned} \quad (3.35)$$

where N^2 is the size of the $x - y$ plane. This calculation is for the homogeneous cubic bulk chiral magnets. Roughly, we can compare the absolute value of $\langle Q \rangle$ in 3D and 2D at a unique temperature in high temperature region. It is obvious that, the value of 3D is smaller than 2D.

3.3 Thickness dependence

The deviation of spins \mathbf{n} away from its ground state can be described by the magnon whose dynamic can be described by a plane wave if it is confined in a finite size space. If the layers at z direction is finite, the modes at z direction is no longer treated continuous due to the cut-off of $|k_z|$ as Λ and $\Lambda \sim \frac{1}{a}$ where a is the lattice constant of the cubic lattice. To explain the thickness dependent

problem, Λ is set to be $\frac{\pi}{a}$. If the number of layers is N_z , the modes of magnons has $k_z = \frac{\pi m}{(N_z-1)a}$, in which $N_z \geq 2$ and $m \leq N_z - 1$ is an integer makes $|k_z| \leq \Lambda$. When the number of layers are small, the modes are discrete. When the number of layers increases, the number of modes increases correspondingly in the range of $[0, \Lambda]$ which means the magnon becomes more close to the continuous modes. It can explain why the number of layers get to some point, the topological charge versus temperature figures do not change in configurations.

3.3.1 Mean field approximation

Firstly, the k_z is discretized and $k = \sqrt{k_x^2 + k_y^2}$ is defined for simplicity. Employing Pauli-Villars regularization[114, 115, 116] the mean field approximation is regularization, the mean field approximation is

$$\begin{aligned}
\sum_{k_z} \int \frac{d^2 k}{(2\pi)^2} \frac{1}{k^2 + k_z^2 + m_0^2} &\rightarrow \sum_{k_z} \int \frac{d^2 k}{(2\pi)^2} \frac{1}{k^2 + k_z^2 + m_0^2} - \frac{1}{k^2 + k_z^2 + \Lambda^2} = \frac{\mathcal{N}\Lambda}{2f} \\
&\sum_{k_z} \int \frac{d^2 k}{(2\pi)^2} \frac{1}{k^2 + k_z^2 + m_0^2} - \frac{1}{k^2 + k_z^2 + \Lambda^2} = \frac{\mathcal{N}\Lambda}{2f} \\
\frac{2\pi}{2} \int \frac{dk^2 dk_z}{(2\pi)^2} \frac{1}{k^2 + k_z^2 + m_0^2} - \frac{1}{k^2 + k_z^2 + \Lambda^2} &= \frac{\mathcal{N}\Lambda}{2f} \\
&\sum_{k_z} \frac{1}{4\pi} \log \frac{k_z^2 + \Lambda^2}{k_z^2 + m_0^2} = \frac{\mathcal{N}\Lambda}{2f} \\
&\sum_k \log \frac{k_z^2 + \Lambda^2}{k_z^2 + m_0^2} = \frac{2\pi\mathcal{N}\Lambda}{f}
\end{aligned} \tag{3.36}$$

when $\mathcal{N} = 2$,

$$\sum_{k_z} \log \frac{k_z^2 + \Lambda^2}{k_z^2 + m_0^2} = \frac{4\pi}{f} \tag{3.37}$$

when $N_z = 1$ which means $k_z = 0$, it is

$$\log \frac{\Lambda^2}{m_0^2} = \frac{4\pi}{f} \tag{3.38}$$

When $N_z = 2$,

$$\begin{aligned}
\log \frac{2\Lambda^2}{\Lambda^2 + m_0^2} + \log \frac{\Lambda^2}{m_0^2} &= \frac{4\pi}{f} \\
\log \frac{2\Lambda^4}{(\Lambda^2 + m_0^2)m_0^2} &= \frac{4\pi}{f} \\
\frac{(\Lambda^2 + m_0^2)m_0^2 + \frac{1}{4}\Lambda^4}{2\Lambda^4} &= \exp\left(-\frac{4\pi}{f}\right) \\
(\Lambda^2 + m_0^2)^2 &= 2\Lambda^4 \exp\left(-\frac{4\pi}{f}\right) - \frac{1}{4}\Lambda^4 \\
m_0^2 &= \Lambda^2 \left(\sqrt{2 \exp\left(-\frac{4\pi}{f}\right) - \frac{1}{4}} - 1 \right). \tag{3.39}
\end{aligned}$$

when $N_z = 3$, $|k_z| = 0$, $\frac{\pi}{2a}(\frac{\Lambda}{2})$, $\frac{\pi}{a}(\Lambda)$,

$$\begin{aligned}
\log \frac{\frac{\Lambda^2}{4} + \Lambda^2}{\frac{\Lambda^2}{4} + m_0^2} + \log \frac{2\Lambda^2}{\Lambda^2 + m_0^2} + \log \frac{\Lambda^2}{m_0^2} &= \frac{4\pi}{f} \\
\log \left(\frac{5\Lambda^2}{\Lambda^2 + 4m_0^2} \right) + \log \frac{2\Lambda^2}{\Lambda^2 + m_0^2} + \log \frac{\Lambda^2}{m_0^2} &= \frac{4\pi}{f}. \tag{3.40}
\end{aligned}$$

When $N_z = n$, $k_z = \frac{\pi m}{(n-1)a}$ ($m = \pm(n-1), \pm(n-2), \dots, 0$).

3.3.2 Thickness dependence of $\langle b_z \rangle$

By comparing to the 2D calculation, the effective action is similar to 2D model, just add \sum_{k_z} and replace Λ^2 and m_0^2 by $\Lambda^2 + k_z^2$ and $m_0^2 + k_z^2$,

$$S_{b^2} = \frac{L^4}{\pi} \sum_{k_z} \int \frac{d^2 q}{(2\pi)^2} \frac{b_q^2}{12(m_0^2 + k_z^2)} + \mathcal{O}(q^2 b^2) \tag{3.41}$$

$$S_{hb} = \frac{2L^4 \kappa^2}{\pi} \sum_{k_z} \int \frac{d^2 q}{(2\pi)^2} \left[\frac{(\Lambda^2 + k_z^2)^3 - (m_0^2 + k_z^2)^3}{(m_0^2 + k_z^2)^2 (\Lambda^2 + k_z^2)^3} + \mathcal{O}(q^2) \right] h_{-q} b_q. \tag{3.42}$$

By solving the equation $\frac{\delta(S_{b^2} + S_{hb})}{\delta b} = 0$, we can get

$$\langle b \rangle = 12\kappa^2 h \sum_{k_z} \frac{(\Lambda^2 + k_z^2)^3 - (m_0^2 + k_z^2)^3}{(\Lambda^2 + k_z^2)^3 (m_0^2 + k_z^2)^2} / \sum_{k_z} \frac{1}{m_0^2 + k_z^2}. \tag{3.43}$$

Several N_z has been chosen to do this calculation and the results shown in Figure 3.7. From Figure 3.7(a), the $\langle b_z \rangle$ will decay more quickly and has the larger

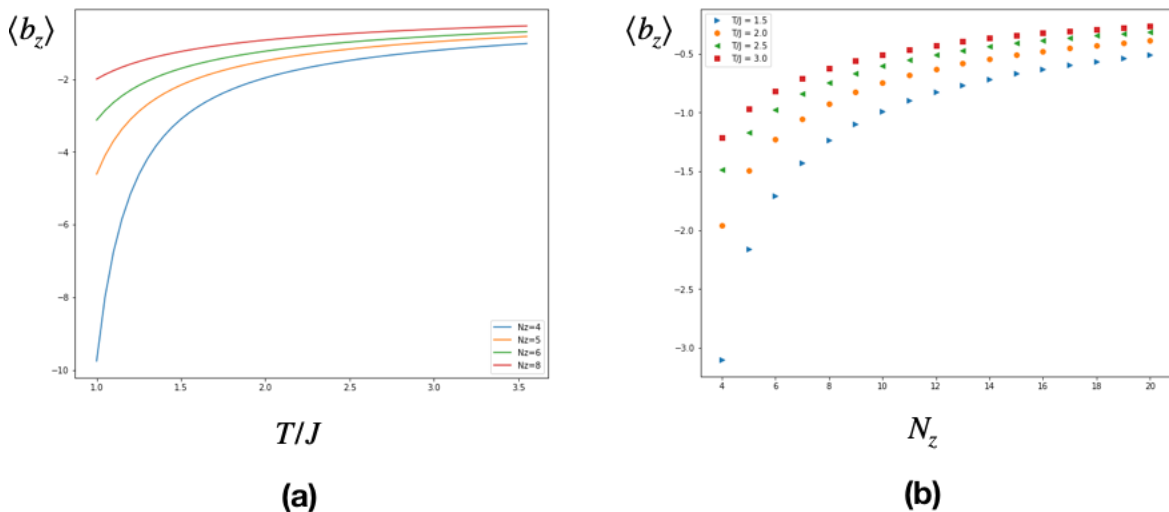


Figure 3.7: (a) The relationship between $\langle b_z \rangle$ and T/J . (b) The relationship between $\langle b_z \rangle$ and T/J .

value with a smaller number of layers. And Figure 3.7(b) shows at each fixed temperature chosen, $\langle b_z \rangle$ will decay with the increasing number of the layers. When the number arrives at some point, the change of the $\langle b_z \rangle$ becomes flat. The analysis from a magnon view is consistent with the numerical results, especially for the invariance of the topological charge when the numbers of layers are larger than some value.

3.4 Conclusion

As an extensive work of the 2D chiral magnets[102], we investigate the topological charge in 3D chiral magnetic system through Monte Carlo simulation and CP^1 field theory calculation. Then thickness dependent phenomenon was also discussed explained by a physical picture of the magnon excitations. Whatever from the numerical or the analytical results, it can be seen that the absolute value of the topological charge at the valley point is smaller with a larger number of the

layers. When the number of layer arrives at some point, the configurations of the of $\langle Q \rangle$ versus T/J figures is invariant, won't change with increasing of the layers.

In the experiments of thin film SrRuO_3 [103], they increased the number of layers to test the variance of the THE signals. When the number of layers is seven, there no THE signal. Because the DM interaction in $\text{SrRuO}_3/\text{SrTiO}_3$ is due to the interface effect. The $D_{eff} \times t = \text{constant}$ where t is the number of layers. Our theoretical calculation is based on the model of homogenous chiral magnets. So we look forward the future experiments to confirm or fight against our results.

CHAPTER IV

Topological charge in antiferromagnetic system with different kinds of DM interaction

The results from chapter II and chapter III have proved that the nonzero topological charge does not respond to the existence of the skyrmions in the magnetic systems[102]. However, the topological charge is very important to the topological Hall effect, as mentioned in previous chapters[77, 87]. In the previous chapters, we just focus on the the spin systems with ferromagnetic interaction and Dzyloshinskii-Moriya(DM) interaction which is parallel to the bonds of two nearest spins. This model describes the non-centrosymmetric ferromagnets. The Heisenberg interaction in the this system is ferromagnetic system. It is natural to think about the situation when the type of Heisenberg interaction changes to the antiferromagnetic interaction. This magnetic system can be found in real materials, for example, the monolayer MnBi[124, 125]. By the results from the previous chapters, the DM interaction plays an important role to produce the nonzero topological charge in non-centrosymmetric system. However, in centrosymmetric magnets, there still can be DM interaction. The staggered DM interaction will respect the inversion symmetry of the whole system and can be found in CaMnO_3 [126, 127, 128], BiFeO_3 [129, 130, 131] and LaFeO_3 [132] . In this chapter, the thermally driven topology in non-centrosymmetric antiferromagnet and centrosymmetric an-

tiferromagnet with staggered DM interactions will be discussed.

4.1 Topological charge in frustrated magnetic system

The thermally driven topology of the 2D Antiferromagnetic frustrated system has been studied in Ref[133]. The model is based on a simple hexagonal lattice which can be regarded as a 2D hexagonal boron nitride structure with buckling, as shown in Figure 4.1(a). There are two sublattices A and B, are in different atomic

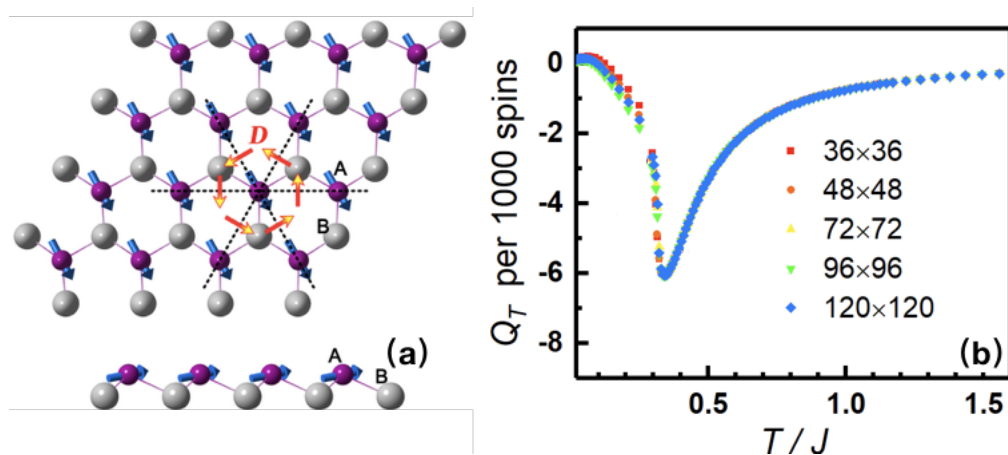


Figure 4.1: (a)Top view and side view of the Top view and side view for the crystal structure of a 2D hexagonal lattice with A and B sublattices. (b)The relationship between topological charge density and temperature with $D = 0.40J$, $K_u = 0.20J$ and $B = 0.40J$.

mono-layers. Magnetic atoms are located at sublattice A and heavy atoms such as 4d or 5d transition metal with strong spin-orbit coupling (SOC) are located at B. A has local magnetic moment. Three dashed lines in Figure 4.1 give six nearest neighbors for one A site. The direction of DM interaction \mathbf{D} is given by six arrows. This system has the point group of C_{3v} without inversion symmetry and it is also a prototype of many non-centrosymmetric magnetic monolayer film systems such as Fe/Ir(111) and Fe/Re(0001)[134, 135, 136]. Then the Hamiltonian in this model is given by

$$H = \sum_{\langle ij \rangle} [J \mathbf{S}_i \cdot \mathbf{S}_j + \mathbf{D}_{ij} \cdot (\mathbf{S}_i \times \mathbf{S}_j)] - \sum_i \left(\frac{1}{2} K_u \mathbf{S}_{iz}^2 + B S_{iz} \right), \quad (4.1)$$

where $\langle ij \rangle$ means nearest neighbors in the first term, $J > 0$ is for antiferromagnetic Heisenberg interaction which originates from the superexchange between two neighboring A sites along A-B-A bond as well as direct exchange along A-A bond. The direction of DM interaction is shown in Figure 4.1 which is perpendicular to the bond connecting the nearest magnetic sites. $|\mathbf{D}_{ij}| = D$ is a constant in the numerical simulation. The K_u is the uniaxial anisotropy. In this model, the anisotropy makes the z -axis which is perpendicular to the plane of hexagonal lattice plane as an easy axis of spins. The object of introducing this interaction is to study the MnBi system. The last term in Hamiltonian is the Zeeman coupling term. B is the external magnetic system.

It has been reported that the skyrmion phase is, in principle, possible in frustrated magnets[137, 138]. However, such phase exists only at external fields B comparable to the antiferromagnetic exchange J , which is extremely large in most antiferromagnets. The Monte Carlo simulations reveal that nonzero topological charge takes place at low fields and elevated temperatures. The numerical results predicted that the experiments can be easily performed to measure the signals from the topological charge. Specially, in monolayer MnBi, the DM interaction is exceedingly large. The high field situation is also discussed in this work. Figure 4.1(b) shows the relationship between the topological charge and temperature. It is obvious that the topological charge is immune from finite size effect. The parameters are $D = 0.40J$, $K_u = 0.20J$ and $B = 0.40J$. The topological charge density is zero at very low temperature. With the increasing of the temperature, at some point, the topological charge begins to emerge and get the maximum of the absolute value at $T = 0.34J$ with $|Q_T|$ about 6.07 per 1000 spins. Then

the absolute value of the topological charge decays. At very high temperature it converges to zero. Accomplishing that, the spin textures become completely random. The configuration of the $|Q_T|$ per 1000 spins versus temperature is similar to the 2D homogeneous non-centrosymmetric ferromagnets which have been shown in Chapter[102]. Also, in this work, the Q_T versus magnitude of DM interaction D and the external magnetic field B has been done. At the high temperature $T = 1.49J$. It is

$$Q_T \propto D^2 B \quad (4.2)$$

The results are shown in Figure 4.4. And also the relationship between Q_T and

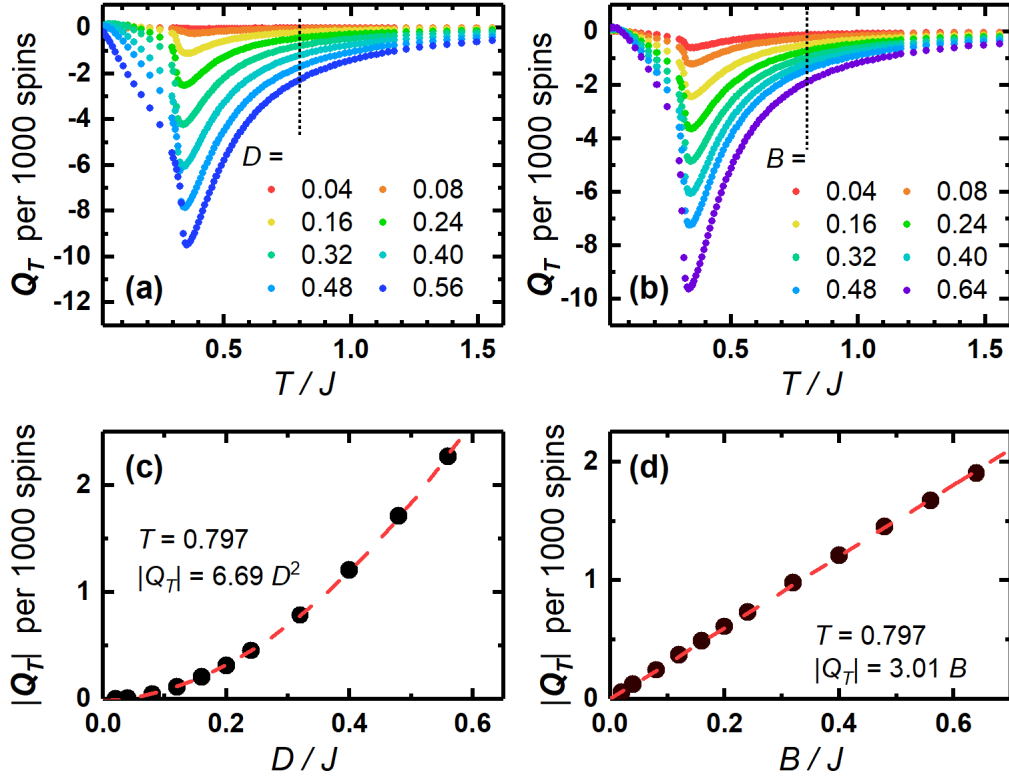


Figure 4.2: Relationship between topological charge, and DM interaction as well as external magnetic field.

the anisotropy K_u is studied in this work. The Figure 4.5 shows the results. At

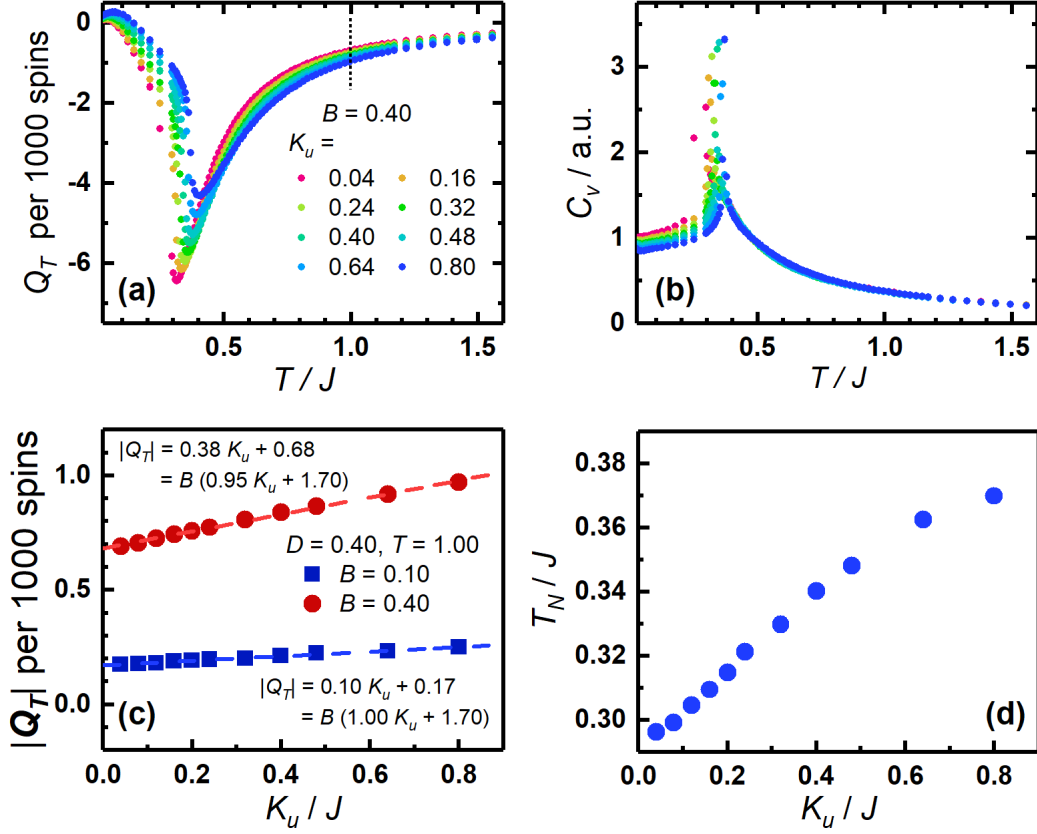


Figure 4.3: Relationship between topological charge and uniaxial magnetic anisotropy.

high temperature, it is

$$Q_T \propto D^2 B(1 + \alpha K_u), \quad \alpha > 0. \quad (4.3)$$

Here, in frustrated magnetic system with antiferromagnetic system also has the thermally driven topology.

4.2 Topological charge in antiferromagnets with staggered DM interaction.

4.2.1 Model

Here, we perform the calculation on a 2D antiferromagnetic square lattice with staggered DM interaction. There are two sublattices, A and B . The unit cell is shown in Figure 4.4(a). The position of the unit cell is chosen as the same position as A site. The primitive vectors are $\hat{a}_1 = \hat{x} + \hat{y}$ and $\hat{a}_2 = \hat{x} - \hat{y}$.

$$\begin{aligned}
H &= \sum_i \frac{J}{2} \mathbf{S}_i^A \cdot (\mathbf{S}_i^B + \mathbf{S}_{i+\hat{a}_1}^B + \mathbf{S}_{i+\hat{a}_2}^B + \mathbf{S}_{i+\hat{a}_1+\hat{a}_2}^B) \\
&\quad + \frac{D}{2} [\hat{y} \cdot \mathbf{S}_i^A \times (\mathbf{S}_i^B + \mathbf{S}_{i+\hat{a}_1+\hat{a}_2}^B) - \hat{x} \cdot (\mathbf{S}_{i+\hat{a}_1}^B + \mathbf{S}_{i+\hat{a}_2}^B)] \\
&\quad - B \sum_i (S_{iz}^A + S_{iz}^B)
\end{aligned} \tag{4.4}$$

in which $J > 0$ and $D > 0$. For site B , $A \leftrightarrow B$, $D \rightarrow -D$ is the reason why it is called staggered DM interaction. The Fourier transformation of $S(r)$ as

$$S_i^A = \frac{1}{\sqrt{N}} \sum_k S_k^A \exp(i\mathbf{k} \cdot \mathbf{R}_i) \tag{4.5}$$

$$S_i^B = \frac{1}{\sqrt{N}} \sum_k S_k^B \exp(-ik_x) \exp(i\mathbf{k} \cdot \mathbf{R}_i) \tag{4.6}$$

The Heisenberg interaction part is

$$\begin{aligned}
H_{Heisenberg} &= \frac{J}{2N} \sum_i \sum_{k'} \sum_k \mathbf{S}_{k'}^A \cdot \mathbf{S}_k^B e^{i(\mathbf{k}'+\mathbf{k}) \cdot \mathbf{R}_i} (e^{ik_x} + e^{-ik_x} + e^{ik_y} + e^{-ik_y}) \\
&= \frac{J}{N} \sum_{k'} \sum_k \mathbf{S}_{k'}^A \cdot \mathbf{S}_k^B \delta_{k+k',0} (\cos k_x + \cos k_y) \\
&= J \sum_k \mathbf{S}_{-k}^A \cdot \mathbf{S}_k^B (\cos k_x + \cos k_y).
\end{aligned}$$

The DM interaction is

$$\begin{aligned}
H_{DM} &= \frac{2D}{2N} \sum_i \sum_{k'} \sum_k (\hat{y} \cdot \mathbf{S}_{k'}^A \times \mathbf{S}_k^B \cos k_x - \hat{x} \cdot \mathbf{S}_{k'}^A \times \mathbf{S}_k^B \cos k_y) e^{i(k+k') \cdot \mathbf{R}_i} \\
&= D \sum_k (\hat{y} \cdot \mathbf{S}_{-k}^A \times \mathbf{S}_k^B \cos k_x - \hat{x} \cdot \mathbf{S}_{-k}^A \times \mathbf{S}_k^B \cos k_y)
\end{aligned}$$

The total energy has the form



Figure 4.4: (a)The unit cell and primitive vectors. (b)The smallest cell of staggered DM situation.

$$H = \frac{1}{2} \sum_k (\mathbf{S}_{-k}^{AT}, \mathbf{S}_{-k}^{BT}) \begin{pmatrix} 0 & M_k \\ M_k^T & 0 \end{pmatrix} \begin{pmatrix} \mathbf{S}_k^A \\ \mathbf{S}_k^B \end{pmatrix} \quad (4.7)$$

in which

$$M = \begin{pmatrix} J(\cos k_x + \cos k_y) & 0 & -D \cos k_x \\ 0 & J(\cos k_x + \cos k_y) & -D \cos k_y \\ D \cos k_x & D \cos k_y & J(\cos k_x + \cos k_y) \end{pmatrix}, \quad (4.8)$$

and $\mathbf{S}_k = \begin{pmatrix} \mathbf{S}_k^A \\ \mathbf{S}_k^B \end{pmatrix}$. Next is to determine the ground state of the system.

4.2.2 Ground state

4.2.2.1 Situation without the external magnetic field

We add the Lagrangian multiplier to make sure the length of the spins $\mathbf{S}_{A,k}$ and $\mathbf{S}_{B,k}$ are the same, $H_\lambda = \lambda(\mathbf{S}_{-k}^A \cdot \mathbf{S}_k^A - \mathbf{S}_{-k}^B \cdot \mathbf{S}_k^B)$. So

$$H = \frac{1}{2} \sum_k (\mathbf{S}_{-k}^{AT}, \mathbf{S}_{-k}^{BT}) \begin{pmatrix} 0 & M_k \\ M_k^T & 0 \end{pmatrix} \begin{pmatrix} \mathbf{S}_k^A \\ \mathbf{S}_k^B \end{pmatrix} \quad (4.9)$$

Solving the equation $\frac{\delta H}{\delta \mathbf{S}_{-k}} = 0$ will get the minimum value of the energy which corresponds to the ground state of the system. The equations are

$$\begin{pmatrix} \lambda I_{3 \times 3} & M_k \\ M_k^T & -\lambda I_{3 \times 3} \end{pmatrix} \begin{pmatrix} \mathbf{S}_k^A \\ \mathbf{S}_k^B \end{pmatrix} = 0. \quad (4.10)$$

Then $\mathbf{S}_k^A = -\frac{M_k M_k^T}{\lambda^2} \mathbf{S}_k^A$ and $\mathbf{S}_k^B = -\frac{M_k^T M_k}{\lambda^2} \mathbf{S}_k^B$. The matrix is

$$M_k M_k^T = M_k^T M_k = \begin{pmatrix} A_k^2 + D^2 \cos^2 k_y & -D^2 \cos k_x \cos k_y & 0 \\ -D^2 \cos k_x \cos k_y & A_k^2 + D^2 \cos^2 k_x & 0 \\ 0 & 0 & A_k^2 + D^2 (\cos^2 k_x + \cos^2 k_y) \end{pmatrix}, \quad (4.11)$$

in which $A_k = J(\cos k_x + \cos k_y)$. The eigenvalues are $E_1^2 = J^2(\cos k_x + \cos k_y)^2$, $E_{2,3}^2 = J^2(\cos k_x + \cos k_y)^2 + D^2(\cos^2 k_x + \cos^2 k_y)$. So $E_{1\pm} = \pm J|\cos k_x + \cos k_y|$, $E_{2,3\pm} = \pm \sqrt{J^2(\cos k_x + \cos k_y)^2 + D^2(\cos^2 k_x + \cos^2 k_y)}$. When $k_x = k_y = 0$, E can get its

minimum $E_{\min} = -2\sqrt{J^2 + \frac{D^2}{2}}$. So we have $\begin{pmatrix} 0 & M_0 \\ M_0^T & 0 \end{pmatrix} \mathbf{S}_0 = -2\sqrt{J^2 + \frac{D^2}{2}} \mathbf{S}_0$.

The $k_x = k_y = 0$ means, for the sublattice A, the ground state is the ferromagnetic

state, and either for sublattice B. Then, we have

$$\begin{pmatrix} 2J & 0 & -D \\ 0 & 2J & -D \\ D & D & 2J \end{pmatrix} \begin{pmatrix} S_x^B \\ S_y^B \\ S_z^B \end{pmatrix} = -2\sqrt{J^2 + \frac{D^2}{2}} \begin{pmatrix} S_x^A \\ S_y^A \\ S_z^A \end{pmatrix}, \quad (4.12)$$

we define $\cos \theta = \frac{J}{\sqrt{J^2 + \frac{D^2}{2}}}$, $\tan \theta = \frac{D}{\sqrt{2}J}$ and

$$\begin{pmatrix} S_x^A \\ S_y^A \\ S_z^A \end{pmatrix} = - \begin{pmatrix} \cos \theta & 0 & \frac{\sin \theta}{\sqrt{2}} \\ 0 & \cos \theta & -\frac{\sin \theta}{\sqrt{2}} \\ -\frac{\sin \theta}{\sqrt{2}} & \frac{\sin \theta}{\sqrt{2}} & \cos \theta \end{pmatrix} \begin{pmatrix} S_x^B \\ S_y^B \\ S_z^B \end{pmatrix}. \quad (4.13)$$

Here $S_i^c = S_{i,k=0}^c$ and

$$M' = - \begin{pmatrix} \cos \theta & 0 & \frac{\sin \theta}{\sqrt{2}} \\ 0 & \cos \theta & -\frac{\sin \theta}{\sqrt{2}} \\ -\frac{\sin \theta}{\sqrt{2}} & \frac{\sin \theta}{\sqrt{2}} & \cos \theta \end{pmatrix}. \quad (4.14)$$

Then

$$\begin{aligned} M' M'^T = M'^T M' &= \begin{pmatrix} \cos \theta & 0 & \frac{\sin \theta}{\sqrt{2}} \\ 0 & \cos \theta & -\frac{\sin \theta}{\sqrt{2}} \\ -\frac{\sin \theta}{\sqrt{2}} & \frac{\sin \theta}{\sqrt{2}} & \cos \theta \end{pmatrix} \begin{pmatrix} \cos \theta & 0 & -\frac{\sin \theta}{\sqrt{2}} \\ 0 & \cos \theta & \frac{\sin \theta}{\sqrt{2}} \\ \frac{\sin \theta}{\sqrt{2}} & -\frac{\sin \theta}{\sqrt{2}} & \cos \theta \end{pmatrix} \\ &= \begin{pmatrix} \cos^2 \theta + \frac{1}{2} \sin^2 \theta & -\frac{1}{2} \sin^2 \theta & 0 \\ -\frac{1}{2} \sin^2 \theta & \cos^2 \theta + \frac{1}{2} \sin^2 \theta & 0 \\ 0 & 0 & \cos^2 \theta + \frac{1}{2} \sin^2 \theta \end{pmatrix}. \end{aligned} \quad (4.15)$$

The equation is

$$\mathbf{S}^A = M'^T M' \mathbf{S}^A \quad (4.16)$$

$$\mathbf{S}^B = M' M'^T \mathbf{S}^B \quad (4.17)$$

By solving the equations, we can get $S_x^c = S_y^c$, $S_z^c = 0$ where $c = A, B$ which means the spins of sublattice A and sublattice B are parallel to the diagonal direction of the square lattice.

4.2.2.2 The situation with external magnetic field

When turning on a small external magnetic field perpendicular to the 2D plane, intuitively speaking, the component at the direction of the magnetic moments will not be zero. Following the results of ground state without the external magnetic field, we can make the ansatz as

$$\mathbf{S}_A = \left(\frac{1}{\sqrt{2}} \sin \theta_A, \frac{1}{\sqrt{2}} \sin \theta_A, \cos \theta_A \right), \quad (4.18)$$

which is for sublattice A and for sublattice B, it is

$$\mathbf{S}_B = \left(\frac{1}{\sqrt{2}} \sin \theta_B, \frac{1}{\sqrt{2}} \sin \theta_B, \cos \theta_B \right), \quad (4.19)$$

With this ansatz, the energy of one unit cell is

$$H = 2J \cos(\theta_A - \theta_B) - \sqrt{2}D \sin(\theta_A - \theta_B) - B(\cos \theta_A + \cos \theta_B). \quad (4.20)$$

Then we minimize the energy by solving the following equations,

$$\frac{\partial H}{\partial \theta_A} = -2J \sin(\theta_A - \theta_B) - \sqrt{2}D \cos(\theta_A - \theta_B) + B \sin \theta_A = 0, \quad (4.21)$$

$$\frac{\partial H}{\partial \theta_B} = 2J \sin(\theta_A - \theta_B) + \sqrt{2}D \cos(\theta_A - \theta_B) + B \sin \theta_A = 0. \quad (4.22)$$

Then the solution is

$$\sin \theta_A = -\sin \theta_B, \quad (4.23)$$

with $\theta_A, \theta_B \in [-\pi, \pi]$. So we can get $\theta_A = -\theta_B$. And

$$2J \sin 2\theta_A + \sqrt{2}D \cos 2\theta_A = B \sin \theta_A. \quad (4.24)$$

This results match the Monte Carlo simulation at almost zero temperature. The ground state is that the in-plane components are parallel to the diagonal direction of the square lattice but for sublattice A and sublattice B, the in-plane components are antiparallel. And the sublattice A and sublattice B have the same component perpendicular to the plane. This is a canted antiferromagnetic phase.

4.2.3 Spin chirality at high temperature

Inspired by the work of the chiral magnets, we investigate the topological charge of the smallest cell. We use the spin chirality of the triangle to replace the solid angle which is the triple product of the tree spins on this triangle. The smallest unit cell in staggered DM system is shown by Figure4.6(b). The energy is

$$E = -j\mathbf{S}_0 \cdot \sum_{i=1}^4 \mathbf{S}_i + d\mathbf{S}_0 \cdot [\hat{x} \times (\mathbf{S}_1 + \mathbf{S}_3) + \hat{y} \times (\mathbf{S}_2 + \mathbf{S}_4)] - h \sum_{i=0}^4 S_{iz}, \quad (4.25)$$

where $j > 0$ is the Heisenberg antiferromagnetic interaction, d is the magnitude of DM interaction and h is the external magnetic field. The topological charge Q is

$$4\pi Q = \mathbf{S}_0 \cdot (\mathbf{S}_1 \times \mathbf{S}_2 + \mathbf{S}_2 \times \mathbf{S}_3 + \mathbf{S}_3 \times \mathbf{S}_4 + \mathbf{S}_4 \times \mathbf{S}_1). \quad (4.26)$$

The thermal average is

$$\langle Q \rangle = \int \prod_i d\mathbf{S}_i Q \exp(-\frac{H}{T}). \quad (4.27)$$

With high temperature limit,

$$\langle Q \rangle = \int \prod_i d\mathbf{S}_i Q (1 - \frac{H}{T} + \frac{1}{2!}(\frac{H}{T})^2 - \frac{1}{3!}(\frac{H}{T})^3 + \frac{1}{4!}(\frac{H}{T})^4 + \dots). \quad (4.28)$$

Employing the same method from Ref[102], we can get the first non-zero value as the order of $\frac{1}{T}$. Now we need to do an analysis first. The notation is $i = 0 \sim 4$, $\alpha = x, y, z$. The solid angle part $4\pi Q$ gives 3 components of spins. If we want to get the paired components, the total number of components should be even. The Heisenberg term will provide two components and also the DM term. The Zeeman coupling term just provides one component. So it is required that nonzero terms in the polynomial form of $\langle Q \rangle$ should include the odd orders of h . The terms without DM interaction d can be ignored because it is identical to $d = 0$ situation which it is just ferromagnetic phase with an external magnetic field, from the physical picture, the topological charge cannot emerge. Also, the terms with odd orders of d can be ignored because of the binary system, for example, the sublattice A has positive d and B has the negative d . If we sum over all the lattice, the terms of the two different sites will be cancelled with each other. They will not contribute to the net topological charge. The summation of the selecting rules is

1. Odd order of h (even number of the components),

2. Contain d (DM interaction induces the topological charge),
3. the order of d should be even(Terms with odd orders will be canceled with two kinds of sites with opposite DM interaction.)

Then we do it order by order,

- $(\frac{1}{T})^0$: None,
- $(\frac{1}{T})^1$: None,
- $(\frac{1}{T})^2$: None,
- $(\frac{1}{T})^3$: d^2h (proved no contribution),
- $(\frac{1}{T})^4$: jd^2h (proved no contribution).
- $(\frac{1}{T})^5$: j^2d^2h (no contribution), d^2h^3 (no contribution), d^4h (no contribution),

... . We use the *Mathematica* to pick up the terms we want and then pick up all the terms have the even orders of the $s_{i\alpha}$. Our algorithm is

1. Compute $QH^n(n \geq 3)$ which corresponds to the order $\frac{1}{T^n}$,
2. Array $s[j](j = 0 \sim 15)$, replace $\{s_{0x}, s_{0y}, s_{0z}\} \rightarrow \{s[1], s[2], s[3]\}, \dots, \{s_{4x}, s_{4y}, s_{4z}\} \rightarrow \{s[13], s[14], s[15]\}$,
3. Pick up the coefficient of unique combination of j, d and h , for example,
 $Q_3 = \text{coefficient}[QH^3, d^2h]$,
4. For $j = 0, j < 16, j = j + 1, Q_3 = \frac{1}{2}[Q_3 + Q_3(s[j] \rightarrow -s[j])]$. Use this iterative method to eliminate the terms have odd orders of $s_{i\alpha}$,
5. Analyze the left terms.

The way to analyze the left terms is direct forward, just representing the components of spins in spherical coordinate.

1. $\{s[1], s[2], s[3]\} \rightarrow \{\sin \theta_1 \cos \phi_1, \sin \theta_1 \sin \phi_1, \cos \theta_1\}, \dots, \{s[13], s[14], s[15]\} \rightarrow \{\sin \theta_5 \cos \phi_5, \sin \theta_5 \sin \phi_5, \cos \theta_5\}.$
2. $\langle Q \rangle = \int \prod_i d\mathbf{S}_i Q \exp(-\frac{H}{T}), \int \prod_i d\mathbf{S}_i \rightarrow \int \prod_i d\Omega_i = \int \prod_i \sin \theta_i d\theta_i d\phi_i$
3. Then integrate over all the θ_i, ϕ_i . (The Mathematica code will be added as an appendice.)

With the results arrive at $(\frac{1}{T})^5$, at high temperature limit, there is no nonzero contribution terms to the spin chirality. From the view of the symmetry, it is not hard to get the average of the spin chirality is zero. If we change the spin S_1 and S_3 .

$$\begin{aligned}
4\pi Q' &= \mathbf{S}_0 \cdot (\mathbf{S}_3 \times \mathbf{S}_2 + \mathbf{S}_2 \times \mathbf{S}_1 + \mathbf{S}_1 \times \mathbf{S}_4 + \mathbf{S}_4 \times \mathbf{S}_3) \\
&= -\mathbf{S}_0 \cdot (\mathbf{S}_2 \times \mathbf{S}_3 + \mathbf{S}_1 \times \mathbf{S}_2 + \mathbf{S}_1 \times \mathbf{S}_4 + \mathbf{S}_4 \times \mathbf{S}_3) = -4\pi Q. \quad (4.29)
\end{aligned}$$

But from Eqn.(4.24), the energy does not change. It is to prove that the thermal average of chirality is zero. In antiferromagnetic case, it is not proper to use the spin chirality to replace the solid angle. The solid angle need to be calculated by the Berg formula which has been used in the numerical simulation. We did a Metropolis calculation on this five spins system, searching for the explanation based on a simple physical picture as we did in 2D chiral magnets. But no converge results is achieved. The program written by *Mathematica* is attached in Appendix B. It motivated us to investigate the topological charge in a finite size lattice with staggered DM interaction.

4.2.4 Topological charge in antiferromagnetic square lattice with staggered DM interaction

The procedure is similar to the pervious works of calculating the average topological charges in various magnetic systems. The Metropolis method[105] is used

to generate Markov chain of spins to construct the spin lattice. The Berg formula is employed to calculate the solid angle of nearest three spins. Then after summing over all the solid angles, the thermal average of the topological charge is achieved by employing the Boltzmann distribution. The results have been shown as Figure 4.5. The left one of Figure 4.5 shows relationship between topological

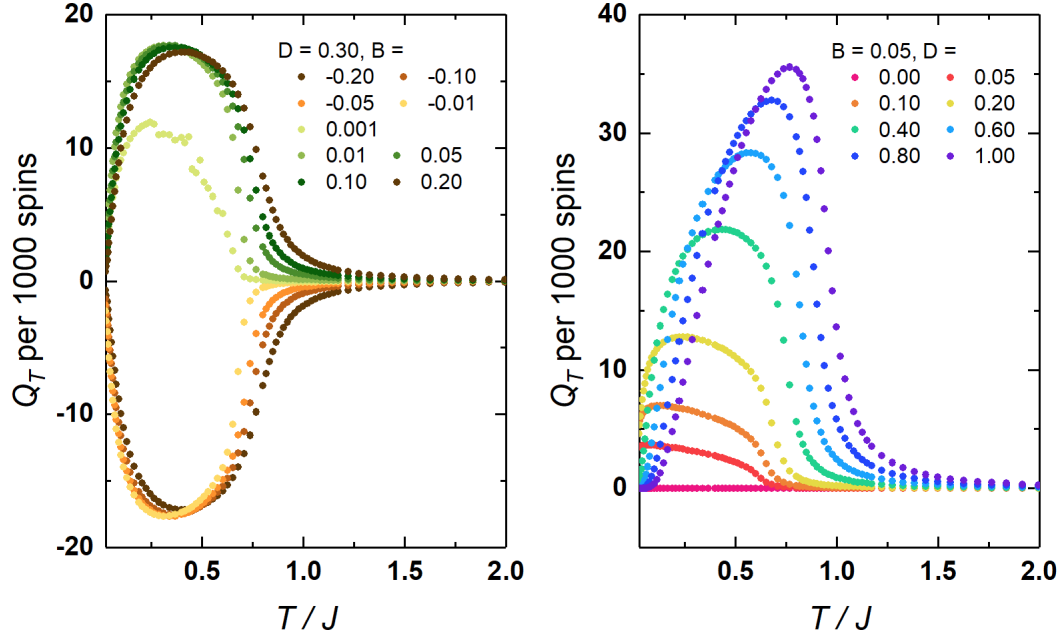


Figure 4.5: The topological charge of antiferromagnetic system with staggered DM interaction

charge density and temperature with fixed DM interaction and various magnetic fields. Comparing to the chiral magnetic system, the topological charge starts to emerge at a very low temperature. Another difference is that when the external magnetic field is along $+z$ direction, the absolute values of topological charge density is positive and the value is large comparing to the chiral magnetic system. When the external magnetic field is along $-z$ direction, the topological charge density is negative. The right picture in Figure 4.5 shows the relationship between topological charge density and temperature with fixed magnetic field and various

DM interaction.

In this system, each site of the lattice is an inversion center. It means the system is centrosymmetric. The giant topological charge density at low temperature need to be further investigated. The ground state without the external magnetic is that the spins are parallel to the diagonal of the square lattice. The nearest three spins are projected on the sphere as shown in Figure 4.6(a) and (b). At

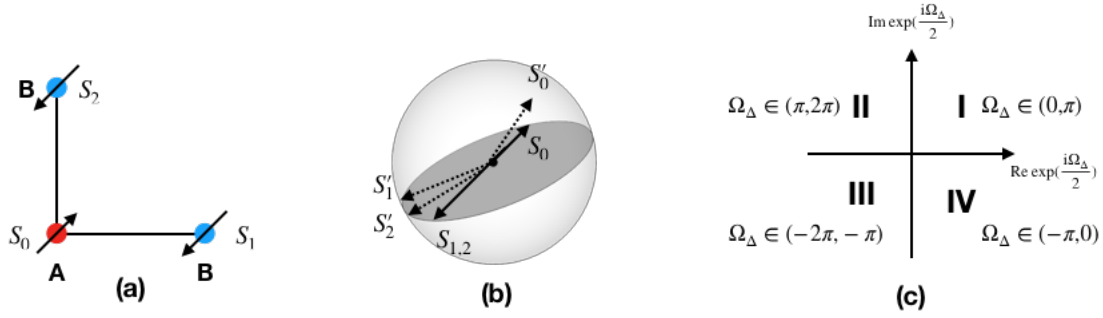


Figure 4.6: (a) Three spins on one triangle.(b)The projection for the three spins on the shpere.(c)The value of solid angle Ω_Δ by Berg formula.

zero temperature, if there is no external magnetic field, they are coplanar. After turning on the external magnetic field along $+z$ direction, they will get a nonzero component of z direction. With increasing the temperature, the \mathbf{S}_1 and \mathbf{S}_2 will no be parallel by the thermal fluctuation. The three spins are no longer coplanar. There will be a spin configurations of the three spins shown by \mathbf{S}'_0 , \mathbf{S}'_1 and \mathbf{S}'_2 as shown in Figure 4.8(b). The solid angle surrounded by them three is almost 2π . A jump of solid angle from zero to almost 2π (or -2π when magnetic field is along $-z$ direction) is induced by the thermal fluctuation. The Berg formula[104] can be written in another form,

$$\begin{aligned} \exp(\frac{i\Omega_{\Delta_1}}{2}) &= \cos(\frac{\Omega_{\Delta_1}}{2}) + i \sin(\frac{\Omega_{\Delta_2}}{2}) \\ &= \frac{1}{\rho} [(1 + \mathbf{S}_0 \cdot \mathbf{S}_1 + \mathbf{S}_1 \cdot \mathbf{S}_2 + \mathbf{S}_2 \cdot \mathbf{S}_0) + i\mathbf{S}_0 \cdot (\mathbf{S}_1 \times \mathbf{S}_2)]. \end{aligned} \quad (4.30)$$

How to determine the value of Ω_{Δ} is shown in Figure 4.8(c). This phenomenon happens around the ground state. When the temperature becomes higher, the topological charge will be zero because of the randomness of spin textures. The $B - T$ diagram of topological charge is shown in Figure 4.7. It shows a symmetric

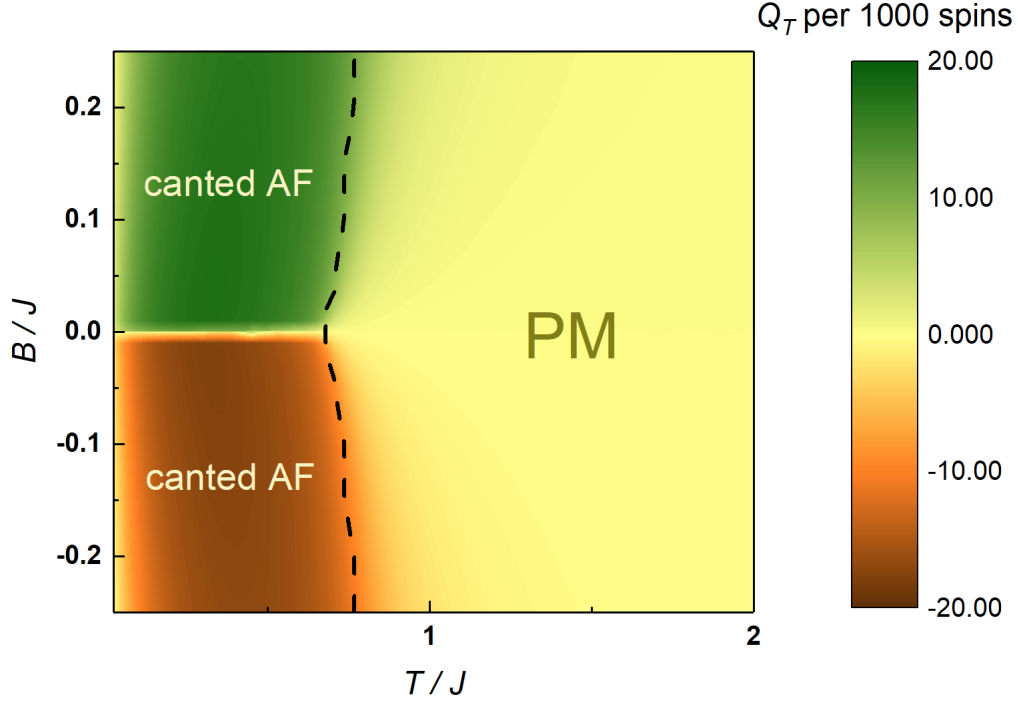


Figure 4.7: $B - T$ diagram of topological charge in staggered DM system.

pattern about $B = 0$. The topological charge in paramagnetic phase is zero due to the totally random spin textures. Also several points at different temperatures are selected to capture the snapshots to investigate the spin textures, shown in Figure 4.8. The DM interaction is $D = 0.20J$ and external magnetic field is $B = 0.10J$.

In this system, whether the topological hall effect is still connected to the topological charge is doubted. The topological hall effect can be explained by the adiabatic motion of electrons in magnetic system when the spin textures vary gradually. In this kind of system, the nonzero topological charge exists at the canted antiferromagnetic phase which has a staggered spin textures, the nearest

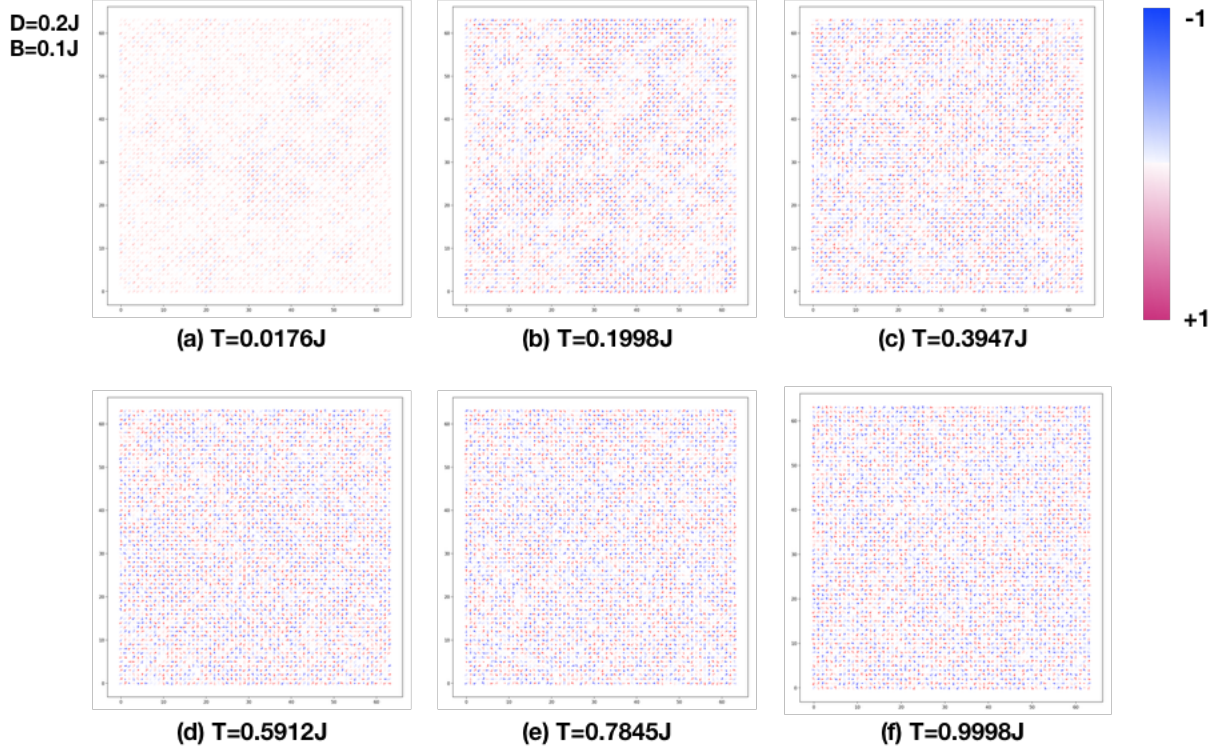


Figure 4.8: Snapshots of spin textures (a) $T = 0.0176J$. (b) $T = 0.1998J$. (c) $T = 0.3947J$. (d) $T = 0.5912J$. (e) $T = 0.7845J$. (f) $T = 0.9998J$. And $D = 0.2J, B = 0.1J$.

spins are almost antiparallel. We look forward to the experiments to investigate the relationship of topological charge and topological Hall effect in the antiferromagnetic systems. Another is that in this system, the difference of the topological charge and spin chirality is significant. The relationship between topological Hall conductivity, spin chirality and topological charge need to be further investigated

CHAPTER V

Proximity effect between skyrmion material and Type-II superconductor

As mentioned in the introduction, the magnetic skyrmion is a vortex like structure and the skyrmion crystal phase has the triangle lattice arrangement. In type-II superconductor, there is a vortex phase. At this vortex phase, the arrangement of the vortices is a triangular lattice. This triangular lattice is called by Abrikosov lattice. With the similarity of the vortex structure and the triangular arrangement, the interaction of the skyrmions and vortices in type-II superconductors[139, 140] intrigued our interest. Our investigation based on a system contains two thin films contacted together. One of the two films is the type-II superconductor and another is skyrmion material. The type-II superconductor is in the vortex phase and skyrmion material is in the SkX phase. The proximity effect of electrons in the interface of the two films is studied by perturbative calculation. The behavior of the vortices is described by the copper pairs . The direct way to understand the interaction between vortices and skyrmions is to study the interaction between the copper pairs and magnetization of the skyrmion materials.

5.1 Model

We consider a 2D system consists of skyrmion material and superconductor thin films. The superconductor is s-wave, so the copper pair is described by a scalar field. The wave function of electrons is written in Nambu space[141] as

$$\Psi = (\psi_{\uparrow}, \psi_{\downarrow}, \psi_{\downarrow}^{\dagger}, -\psi_{\uparrow}^{\dagger})^T \quad (5.1)$$

The Hamiltonian of the model is

$$\mathcal{H} = \frac{1}{2}\Psi^{\dagger}\tau_z\left(\frac{p^2}{2m} - \mu + \alpha\mathbf{p}\cdot\sigma\right)\Psi - \frac{1}{2}J_H\Psi^{\dagger}\mathbf{M}\cdot\sigma\Psi - g(\Delta\psi_{\uparrow}^{\dagger}\psi_{\downarrow}^{\dagger} + h.c.), \quad (5.2)$$

hich can describe the non-centrosymmetric superconductor and the skyrmion materials. $\mathbf{M} = (M_x, M_y, M_z)$ is used to describe the ferromagnetism. The Δ is the field of the Cooper pair for the s-wave superconductor, the coupling constant is g . α is the strength of Dresselhaus spin orbit coupling. For simplicity, we set Hund's coupling $J_H = 1$ and $g = 1$. The motions of the conducting electrons and holes are confined in a two-dimensional(2D) plane, so $p_z = 0$. The action can be written as

$$S = \int_0^{\beta} d\tau \int_0^L d^2r \left\{ \frac{1}{2}\Psi^{\dagger}[\partial_{\tau} + \tau_z\left(\frac{(-i\nabla)^2}{2m} - i\alpha\nabla\cdot\sigma - \mu\right)]\Psi - \frac{1}{2}\Psi^{\dagger}\mathbf{M}\cdot\sigma\Psi - (\Delta\psi_{\uparrow}^{\dagger}\psi_{\downarrow}^{\dagger} + h.c.) \right\}. \quad (5.3)$$

Turning to the frequency and momentum space, the Grassmann fields are

$$\psi_{\sigma,n,p} = \frac{1}{L^2\beta} \int_0^{\beta} d\tau \int_0^L d^2r \psi_{\sigma}(r, \tau) e^{i(\omega_n\tau - p\cdot r)}, \quad (5.4)$$

$$\psi_{\sigma,n,-p}^{\dagger} = \frac{1}{L^2\beta} \int_0^{\beta} d\tau \int_0^L d^2r \psi_{\sigma}^{\dagger}(r, \tau) e^{i(\omega_n\tau - p\cdot r)}. \quad (5.5)$$

So $\Psi_{n,p} = (\psi_{\uparrow,n,p}, \psi_{\downarrow,n,p}, \psi_{\downarrow,n,-p}^\dagger, -\psi_{\uparrow,n,-p}^\dagger)^T$. The order parameter,

$$\Delta_k = \frac{1}{L^2} \int_0^L d^2r \Delta(r) e^{-ik \cdot r}, \quad (5.6)$$

$$\bar{\Delta}_{-k} = (\Delta_k)^\dagger = \frac{1}{L^2} \int_0^L d^2r \bar{\Delta}(r) e^{ik \cdot r}. \quad (5.7)$$

The action in momentum space is

$$\begin{aligned} S(\omega_n, p, k) &= \frac{1}{2} \sum_{\omega_n, p} \Psi_p^\dagger \begin{pmatrix} -i\omega_n + \xi_p + \alpha p \cdot \sigma & 0 \\ 0 & -i\omega_n - \xi_{-p} - \alpha p \cdot \sigma \end{pmatrix} \Psi_p \\ &\quad - \frac{1}{2} \frac{T}{L^2} \sum_{p,k} \Psi_{p+\frac{k}{2}}^\dagger \begin{pmatrix} M_k \cdot \sigma & \Delta_k \\ \bar{\Delta}_{-k} & M_k \cdot \sigma \end{pmatrix} \Psi_{p-\frac{k}{2}} \\ &= \frac{1}{2} \left[\sum_{n,p} \Psi_p^\dagger \begin{pmatrix} -i\omega_n + \xi_p + \alpha p \cdot \sigma & 0 \\ 0 & -i\omega_n - \xi_{-p} - \alpha p \cdot \sigma \end{pmatrix} \Psi_p \right. \\ &\quad \left. - \frac{T}{L^2} \sum_{p,k} \Psi_{p+\frac{k}{2}}^\dagger \begin{pmatrix} M_k \cdot \sigma & \Delta_k \\ \bar{\Delta}_{-k} & M_k \cdot \sigma \end{pmatrix} \Psi_{p-\frac{k}{2}} \right] \quad (5.8) \end{aligned}$$

with $\xi_p = \frac{p^2}{2m}$ and $\xi_p = \xi_{-p}$. The interaction part can be defined as

$$\Sigma_k = \frac{T}{L^2} \begin{pmatrix} M_k \cdot \sigma & \Delta_k \\ \bar{\Delta}_{-k} & M_k \cdot \sigma \end{pmatrix} \quad (5.9)$$

The spinor in momentum space can be represented as $\Psi_p = (\psi_{\uparrow,p}, \psi_{\downarrow,p}, \psi_{\downarrow,-p}^\dagger, -\psi_{\uparrow,-p}^\dagger)^T$ and $\Psi_p^\dagger = (\psi_{\uparrow,-p}^\dagger, \psi_{\downarrow,-p}^\dagger, \psi_{\downarrow,p}, -\psi_{\uparrow,p})$. The Green function of electrons and holes

is read as

$$\begin{aligned}
g_p^{(e)} &= \frac{1}{-i\omega_n + \xi_p + \alpha \mathbf{p} \cdot \boldsymbol{\sigma}} \\
&= \frac{-i\omega_n + \xi_p - \alpha \mathbf{p} \cdot \boldsymbol{\sigma}}{(-i\omega_n + \xi_p)^2 - \alpha^2 p^2}, \tag{5.10}
\end{aligned}$$

$$\begin{aligned}
g_{-p}^{(h)} &= \frac{1}{-i\omega_n - \xi_{-p} - \alpha \mathbf{p} \cdot \boldsymbol{\sigma}} \\
&= \frac{-i\omega_n - \xi_{-p} + \alpha \mathbf{p} \cdot \boldsymbol{\sigma}}{(-i\omega_n - \xi_{-p})^2 - \alpha^2 p^2}. \tag{5.11}
\end{aligned}$$

And

$$\begin{aligned}
g_p^{(e)\dagger} &= \frac{i\omega_n + \xi_p - \alpha \mathbf{p} \cdot \boldsymbol{\sigma}}{(i\omega_n + \xi_p)^2 - \alpha^2 p^2} \\
&= -\frac{-i\omega_n - \xi_{-p} + \alpha \mathbf{p} \cdot \boldsymbol{\sigma}}{(-i\omega_n - \xi_{-p})^2} = -g_{-p}^{(h)} \tag{5.12}
\end{aligned}$$

$$\begin{aligned}
g_{-p}^{(h)\dagger} &= \frac{i\omega_n - \xi_p + \alpha \mathbf{p} \cdot \boldsymbol{\sigma}}{(i\omega_n - \xi_p)^2 - \alpha^2 p^2} \\
&= -\frac{-i\omega_n + \xi_p - \alpha \mathbf{p} \cdot \boldsymbol{\sigma}}{(-i\omega_n - \xi_p)^2 - \alpha^2 p^2} = -g_p^{(e)} \tag{5.13}
\end{aligned}$$

Further,

$$\begin{aligned}
g_{p+\frac{k}{2}}^{(e)} &= \frac{-i\omega_n + \frac{(p+\frac{k}{2})^2}{2m} - \alpha(\mathbf{p} + \frac{\mathbf{k}}{2}) \cdot \boldsymbol{\sigma}}{[-i\omega_n - \frac{(p+\frac{k}{2})^2}{2m}]^2 - \alpha^2(p + \frac{k}{2})^2} \\
&= \frac{-i\omega_n + \frac{1}{2m}(p^2 + \mathbf{p} \cdot \mathbf{k} + \frac{k^2}{4}) - \alpha(\mathbf{p} + \frac{\mathbf{k}}{2}) \cdot \boldsymbol{\sigma}}{[-i\omega_n - \frac{1}{2m}(p^2 + \mathbf{p} \cdot \mathbf{k} + \frac{k^2}{4})]^2 - \alpha^2(p^2 + \mathbf{p} \cdot \mathbf{k} + \frac{k^2}{4})}. \tag{5.14}
\end{aligned}$$

5.2 Effective action and Its Expansion

Here, we set the Boltzmann constant $k_B = 1$. So, $F = -T \ln Z$ and $-S = -\beta F = \ln Z$ with $\beta = \frac{1}{T}$ where Z is the partition function. And $Z = Tr(e^{-\beta F})$.

The partion function in path integral is

$$\begin{aligned}
Z &= \int \mathcal{D}\Psi^\dagger \mathcal{D}\Psi \exp(-S) \\
&= \int \mathcal{D}\Psi^\dagger \mathcal{D}\Psi \exp\left(-\int_0^\beta d\tau \int_0^L d^2r \frac{1}{2} \Psi^\dagger \mathcal{G} \Psi\right)
\end{aligned} \tag{5.15}$$

.By Summing (Intergrating) over Ψ , $S = -\ln Z = -Tr \ln \mathcal{G}^{-1}$. The minus sign is from the exchage

$$\begin{aligned}
S = -Tr \ln \mathcal{G}^{-1} &= -Tr \ln(\mathcal{G}_0^{-1} + \mathcal{G}_1^{-1}) \\
&= -Tr \ln[\mathcal{G}_0^{-1}(1 + \mathcal{G}_0 \mathcal{G}_1^{-1})] \\
&= -Tr \ln \mathcal{G}_0^{-1} - Tr \ln(1 - \mathcal{G}_0 \Sigma)
\end{aligned} \tag{5.16}$$

. The first term is a constant. After expanding the second term,

$$\begin{aligned}
S = -Tr \ln(1 - \mathcal{G}_0 \Sigma) &= Tr(\mathcal{G}_0 \Sigma) + \frac{1}{2} Tr(\mathcal{G}_0 \Sigma \mathcal{G}_0 \Sigma) + \frac{1}{3} Tr(\mathcal{G}_0 \Sigma \mathcal{G}_0 \Sigma \mathcal{G}_0 \Sigma) \\
&\quad + \frac{1}{4} Tr(\mathcal{G}_0 \Sigma \mathcal{G}_0 \Sigma \mathcal{G}_0 \Sigma \mathcal{G}_0 \Sigma) + \mathcal{O}(\Sigma^5)
\end{aligned} \tag{5.17}$$

and $tr(\mathcal{G}_0 \Sigma) = 0$. We study the free energy for the system, $F = -T \ln Z = TS$.

5.2.1 Second Order Calculation of Free Energy

The second order of the action is

$$\begin{aligned}
S_2 &= \frac{T^2}{2} \sum_n \int \frac{d^2 p}{(2\pi)^2} \int \frac{d^2 q}{(2\pi)^2} \text{Tr}(\mathcal{G}_{0,p+\frac{q}{2}} \Sigma_q \mathcal{G}_{0,p-\frac{q}{2}} \Sigma_{-q}) \\
&= \frac{T^2}{2} \sum_n \int \frac{d^2 p}{(2\pi)^2} \int \frac{d^2 q}{(2\pi)^2} \text{Tr} \begin{pmatrix} g_{p+\frac{k}{2}}^e & 0 \\ 0 & g_{-p-\frac{k}{2}}^h \end{pmatrix} \begin{pmatrix} \mathbf{M}_q \cdot \boldsymbol{\omega} & \Delta_q \\ \bar{\Delta}_{-q} & \mathbf{M}_{-q} \cdot \boldsymbol{\omega} \end{pmatrix} \\
&\cdot \begin{pmatrix} g_{p-\frac{q}{2}}^e & 0 \\ 0 & g_{-p+\frac{q}{2}}^h \end{pmatrix} \begin{pmatrix} \mathbf{M}_{-q} \cdot \boldsymbol{\sigma} & \Delta_{-q} \\ \bar{\Delta}_q & \mathbf{M}_q \cdot \boldsymbol{\sigma} \end{pmatrix} \\
&= \frac{T^2}{2} \sum_n \int \frac{d^2 p}{(2\pi)^2} \int \frac{d^2 q}{(2\pi)^2} \text{Tr} \begin{pmatrix} g_{p+\frac{q}{2}}^e \mathbf{M}_q \cdot \boldsymbol{\sigma} & g_{p+\frac{q}{2}}^e \Delta_q \\ g_{-p-\frac{q}{2}}^h \bar{\Delta}_{-q} & g_{-p-\frac{q}{2}}^h \mathbf{M}_{-q} \cdot \boldsymbol{\sigma} \end{pmatrix} \\
&\cdot \begin{pmatrix} g_{p-\frac{q}{2}}^e \mathbf{M}_{-q} \cdot \boldsymbol{\sigma} & g_{p-\frac{q}{2}}^e \Delta_{-q} \\ g_{-p+\frac{q}{2}}^h \bar{\Delta}_q & g_{-p+\frac{q}{2}}^h \mathbf{M}_q \cdot \boldsymbol{\sigma} \end{pmatrix} \\
&= \frac{T^2}{2} \sum_n \int \frac{d^2 p}{(2\pi)^2} \int \frac{d^2 q}{(2\pi)^2} \text{tr}(g_{p+\frac{q}{2}}^e \Delta_q g_{-p+\frac{q}{2}}^h \bar{\Delta}_q + g_{-p-\frac{q}{2}}^h \bar{\Delta}_{-q} g_{p-\frac{q}{2}}^e \Delta_{-q} \\
&+ g_{p+\frac{q}{2}}^e \mathbf{M}_q \cdot \boldsymbol{\sigma} g_{p-\frac{q}{2}}^e \mathbf{M}_{-q} \cdot \boldsymbol{\sigma} + g_{-p-\frac{q}{2}}^h \mathbf{M}_{-q} \cdot \boldsymbol{\sigma} g_{-p+\frac{q}{2}}^h \mathbf{M}_q \cdot \boldsymbol{\sigma}) = S_{2\Delta} + S_{2M}, \quad (5.18)
\end{aligned}$$

where

$$\begin{aligned}
S_{2\Delta} &= \frac{T^2}{2} \int \frac{d^2 p}{(2\pi)^2} \int \frac{d^2 q}{(2\pi)^2} \text{tr}(g_{p+\frac{q}{2}}^e \Delta_q g_{-p+\frac{q}{2}}^h \bar{\Delta}_q + g_{-p-\frac{q}{2}}^h \bar{\Delta}_{-q} g_{p-\frac{q}{2}}^e \Delta_{-q}) \\
&= \frac{T^2}{8} \int \frac{d^2 p}{(2\pi)^2} \int \frac{d^2 q}{(2\pi)^2} \text{tr}(g_{p+\frac{q}{2},+}^e P_{p+\frac{q}{2},+} + g_{p+\frac{q}{2},-}^e P_{p+\frac{q}{2},-}) \Delta_q \\
&\quad \times (g_{-p+\frac{q}{2},+}^h P_{-p+\frac{q}{2},+} + g_{-p+\frac{q}{2},-}^h P_{-p+\frac{q}{2},-}) \bar{\Delta}_q + h.c. \\
&= \frac{T^2}{4} \int \frac{d^2 p}{(2\pi)^2} \int \frac{d^2 q}{(2\pi)^2} [(g_{p+\frac{q}{2},+}^e + g_{p+\frac{q}{2},-}^e)(g_{-p+\frac{q}{2},+}^h + g_{-p+\frac{q}{2},-}^h) \Delta_q \bar{\Delta}_q \\
&\quad + (g_{p+\frac{q}{2},+}^e - g_{p+\frac{q}{2},-}^e)(g_{-p+\frac{q}{2},+}^h - g_{-p+\frac{q}{2},-}^h) \frac{-p^2 + \frac{q^2}{4}}{|\mathbf{p} + \frac{\mathbf{q}}{2}| |\mathbf{p} - \frac{\mathbf{q}}{2}|} \Delta_q \bar{\Delta}_q] \\
&\quad + h.c. \quad (5.19)
\end{aligned}$$

and

$$\begin{aligned}
S_{2M} &= \frac{T^2}{2} \int \frac{d^2p}{(2\pi)^2} \int \frac{d^2q}{(2\pi)^2} \text{tr}(g_{p+\frac{q}{2}}^e \mathbf{M}_q \cdot \sigma g_{p-\frac{q}{2}}^e \mathbf{M}_{-q} \cdot \sigma + g_{-p-\frac{q}{2}}^h \mathbf{M}_{-q} \cdot \sigma g_{-p+\frac{q}{2}}^h \mathbf{M}_q \cdot \sigma) \\
&= \frac{T^2}{8} \int \frac{d^2p}{(2\pi)^2} \int \frac{d^2q}{(2\pi)^2} \text{tr}[(g_{p+\frac{q}{2},+}^e P_{p+\frac{q}{2},+} + g_{p+\frac{q}{2},-}^e P_{p+\frac{q}{2},-}) \mathbf{M}_q \cdot \sigma \\
&\quad \times (g_{p-\frac{q}{2},+}^e P_{p-\frac{q}{2},+} + g_{p-\frac{q}{2},-}^e P_{p-\frac{q}{2},-}) \mathbf{M}_{-q} \cdot \sigma] + h.c. \\
&= \frac{T^2}{8} \int \frac{d^2p}{(2\pi)^2} \int \frac{d^2q}{(2\pi)^2} \text{tr}[(g_{p+\frac{q}{2},+}^e + g_{p+\frac{q}{2},-}^e) \mathbf{M}_q \cdot \sigma (g_{p-\frac{q}{2},+}^e + g_{p-\frac{q}{2},-}^e) \mathbf{M}_{-q} \cdot \sigma \\
&\quad + (g_{p+\frac{q}{2},+}^e - g_{p+\frac{q}{2},-}^e)(g_{p-\frac{q}{2},+}^e - g_{p-\frac{q}{2},-}^e) \frac{(\mathbf{p} + \frac{\mathbf{q}}{2}) \cdot \sigma \mathbf{M}_q \cdot \sigma (\mathbf{p} - \frac{\mathbf{q}}{2}) \cdot \sigma \mathbf{M}_{-q} \cdot \sigma}{|\mathbf{p} + \frac{\mathbf{q}}{2}| |\mathbf{p} - \frac{\mathbf{q}}{2}|} \\
&\quad + (g_{p+\frac{q}{2},+}^e + g_{p+\frac{q}{2},-}^e)(g_{p-\frac{q}{2},+}^e - g_{p-\frac{q}{2},-}^e) \frac{\mathbf{M}_q \cdot \sigma (\mathbf{p} - \frac{\mathbf{q}}{2}) \cdot \sigma \mathbf{M}_{-q} \cdot \sigma}{|\mathbf{p} - \frac{\mathbf{q}}{2}|} \\
&\quad + (g_{p+\frac{q}{2},+}^e - g_{p+\frac{q}{2},-}^e)(g_{p-\frac{q}{2},+}^e + g_{p-\frac{q}{2},-}^e) \frac{(\mathbf{p} + \frac{\mathbf{q}}{2}) \cdot \sigma (\mathbf{M}_q \cdot \sigma) \mathbf{M}_{-q} \cdot \sigma}{|\mathbf{p} + \frac{\mathbf{q}}{2}|}] + h.c. \\
&= \frac{T^2}{4} \int \frac{d^2p}{(2\pi)^2} \int \frac{d^2q}{(2\pi)^2} [(g_{p+\frac{q}{2},+}^e + g_{p+\frac{q}{2},-}^e)(g_{p-\frac{q}{2},+}^e + g_{p-\frac{q}{2},-}^e) \mathbf{M}_q \cdot \mathbf{M}_{-q} \\
&\quad + (g_{p+\frac{q}{2},+}^e - g_{p+\frac{q}{2},-}^e)(g_{p-\frac{q}{2},+}^e - g_{p-\frac{q}{2},-}^e) \frac{(\delta_{ij}\delta_{kl} - \delta_{ik}\delta_{jl} + \delta_{il}\delta_{jk})}{|\mathbf{p} + \frac{\mathbf{q}}{2}| |\mathbf{p} - \frac{\mathbf{q}}{2}|} \\
&\quad \times (p + \frac{q}{2})_i M_{q,j} (p - \frac{q}{2})_k M_{-q,l} \\
&\quad + (g_{p+\frac{q}{2},+}^e + g_{p+\frac{q}{2},-}^e)(g_{p-\frac{q}{2},+}^e - g_{p-\frac{q}{2},-}^e) \frac{i\varepsilon_{ijk} M_{q,i} (p - \frac{q}{2})_j M_{-q,k}}{|\mathbf{p} - \frac{\mathbf{q}}{2}|} \\
&\quad + (g_{p+\frac{q}{2},+}^e - g_{p+\frac{q}{2},-}^e)(g_{p-\frac{q}{2},+}^e + g_{p-\frac{q}{2},-}^e) \frac{i\varepsilon_{ijk} (p + \frac{q}{2})_i M_{q,j} M_{-q,k}}{|\mathbf{p} + \frac{\mathbf{q}}{2}|}] + h.c. \\
&= \frac{T^2}{4} \int \frac{d^2p}{(2\pi)^2} \int \frac{d^2q}{(2\pi)^2} [(g_{p+\frac{q}{2},+}^e + g_{p+\frac{q}{2},-}^e)(g_{p-\frac{q}{2},+}^e + g_{p-\frac{q}{2},-}^e) \mathbf{M}_q \cdot \mathbf{M}_{-q} \\
&\quad + \frac{(g_{p+\frac{q}{2},+}^e - g_{p+\frac{q}{2},-}^e)(g_{p-\frac{q}{2},+}^e - g_{p-\frac{q}{2},-}^e)}{|\mathbf{p} + \frac{\mathbf{q}}{2}| |\mathbf{p} - \frac{\mathbf{q}}{2}|} [2(\mathbf{p} \cdot \mathbf{M}_q)(\mathbf{p} \cdot \mathbf{M}_{-q}) \\
&\quad - \frac{(\mathbf{q} \cdot \mathbf{M}_q)(\mathbf{q} \cdot \mathbf{M}_{-q})}{2} - (p^2 - \frac{q^2}{4})(\mathbf{M}_q \cdot \mathbf{M}_{-q})]. \tag{5.20}
\end{aligned}$$

Firstly, we consider the dynamic parts of the order parameters. Here, for the purpose to estimate the coefficient before the $\partial \bar{\Delta} \partial \Delta$, we just consider the $\mathcal{O}(\frac{k^2}{m})$ term.

$$F_{\bar{\Delta}\Delta} = \int d^2r [c \partial \bar{\Delta} \partial \Delta + a |\bar{\Delta} \Delta| + \frac{b}{2} |\bar{\Delta} \Delta|^2 + \dots] \tag{5.21}$$

The term $-\frac{T^2}{L^4} \sum_{n,p,k} \frac{\xi_p}{(\omega_n^2 + \xi_p^2)^2} \frac{k^2}{4m} (\Delta_k \bar{\Delta}_{-k} + h.c.)$ corresponds to the the term $\int d^2 r c \partial \bar{\Delta} \partial \Delta$

,

$$\begin{aligned}
& \frac{T^2}{4mL^4} \sum_{n,p,k} \frac{\xi_p}{(\omega_n^2 + \xi_p^2)^2} (\Delta_k \bar{\Delta}_k + h.c.) \\
& \approx - \sum_n \frac{T^2}{8m} \int \frac{d^2 p}{(2\pi)^2} \partial_{\xi_p} \frac{1}{\omega_n^2 + \xi_p^2} \int \frac{d^2 k}{(2\pi)^2} k^2 (\Delta_k \bar{\Delta}_k + h.c.) \\
& = - \sum_n \frac{T^2}{8m} \int \frac{2\pi p dp}{4\pi^2} \partial_{\xi_p} \frac{1}{\omega_n^2 + \xi_p^2} \int \frac{d^2 k}{(2\pi)^2} k^2 (\Delta_k \bar{\Delta}_k + h.c.) \\
& = - \frac{T^2}{8m} \sum_n \int \frac{2md(p^2/2m - \mu)}{4\pi} \partial_{\xi_p} \frac{1}{\omega_n^2 + \xi_p^2} \int \frac{d^2 k}{(2\pi)^2} k^2 (\Delta_k \bar{\Delta}_k + h.c.) \\
& = - \frac{T^2}{16\pi} \int d\xi_p \partial_{\xi_p} \frac{1}{\omega_n^2 + \xi_p^2} \int \frac{d^2 k}{(2\pi)^2} k^2 (\Delta_k \bar{\Delta}_k + h.c.) \\
& = \frac{T^2}{16\pi} \sum_n \frac{1}{\omega_n^2} \int \frac{d^2 k}{(2\pi)^2} k^2 (\Delta_k \bar{\Delta}_k + h.c.) \\
& = \frac{T^2}{16\pi} \sum_n \frac{\beta^2}{\pi^2} \frac{1}{(2n+1)^2} \int \frac{d^2 k}{(2\pi)^2} k^2 (\Delta_k \bar{\Delta}_k + h.c.) \\
& = \frac{T^2}{16\pi} \frac{\beta^2 \pi^2}{8} \int \frac{d^2 k}{(2\pi)^2} k^2 (\Delta_k \bar{\Delta}_k + h.c.) \\
& = \frac{1}{128\pi} \int \frac{d^2 k}{(2\pi)^2} k^2 (\Delta_k \bar{\Delta}_k + h.c.) \tag{5.22}
\end{aligned}$$

In position space,

$$\begin{aligned}
\int \frac{d^2 k}{(2\pi)^2} k^2 (\Delta_k \bar{\Delta}_k + h.c.) & \rightarrow -\frac{2}{L^2} \int d^2 r \Delta \partial^2 \Delta \\
& \rightarrow \frac{2}{L^2} \int d^2 r (\partial \bar{\Delta}) \partial \Delta \tag{5.23}
\end{aligned}$$

. So in this approximation, we recover the coupling parameter g can obtain $c =$

$$\frac{g^2 T}{64\pi L^2}.$$

$$\begin{aligned}
A = ac &= -2T^3 g^2 \sum_n \int \frac{d^2p}{(2\pi)^2} \frac{1}{\omega_n^2 + \xi_p^2} \\
&= -2T^3 g^2 \sum_n \int \frac{2\pi(2m)d\xi_p}{4\pi^2} \frac{1}{\omega_n^2 + \xi_p^2} \\
&= -\frac{2mT^3}{\pi} g^2 \sum_n \int \frac{d\xi_p}{\omega_n} \frac{\omega_n}{\omega_n^2 + \xi_p^2} \\
&= -\frac{2mT^3}{\pi} g^2 \sum_n \int d\left(\frac{\xi_p}{\omega_n}\right) \frac{1}{1 + \left(\frac{\xi_p}{\omega_n}\right)^2} \frac{1}{\omega_n} \\
&= -mT^3 g^2 \sum_n \frac{\beta}{2\pi(2n+1)} \\
&= -\frac{mT^2 g^2}{2\pi} \sum_n \frac{1}{2n+1} \\
a &= -32mT \sum_n \frac{1}{2n+1} \tag{5.24}
\end{aligned}$$

For the local magnetization part, we didn't calculate that. The Ruderman-Kittel-Kasuya-Yosida(RKKY)[142, 143, 144] interaction has been studied in Ref[145], which discuss how the conducting electrons affect the local spins. The result in the reference will give a similar result for this part.

5.2.2 The Third Order Calculation

In the third order calculation

$$\begin{aligned}
S_3 &= \frac{T^3}{3} \mathbf{Tr} \sum_n \int \frac{d^2 p_1 d^2 p_2 d^2 p_3}{(2\pi)^6} \mathcal{G}_{0,p_1} \Sigma_{p_1,p_2} \mathcal{G}_{0,p_2} \Sigma_{p_2,p_3} \mathcal{G}_{0,p_3} \Sigma_{p_3,p_1} \\
&= \frac{T^3}{3} \mathbf{Tr} \sum_n \int \frac{d^2 p_1 d^2 p_2 d^2 p_3}{(2\pi)^6} \begin{pmatrix} g_1^e & 0 \\ 0 & g_{-1}^h \end{pmatrix} \begin{pmatrix} \sigma \cdot M_{12} & \Delta_{12} \\ \bar{\Delta}_{21} & \sigma \cdot M_{12} \end{pmatrix} \\
&\quad \times \begin{pmatrix} g_2^e & 0 \\ 0 & g_{-2}^h \end{pmatrix} \begin{pmatrix} \sigma \cdot M_{23} & \Delta_{23} \\ \bar{\Delta}_{32} & \sigma \cdot M_{23} \end{pmatrix} \begin{pmatrix} g_3^e & 0 \\ 0 & g_{-3}^{(h)} \end{pmatrix} \begin{pmatrix} \sigma \cdot M_{31} & \Delta_{31} \\ \bar{\Delta}_{13} & \sigma \cdot M_{31} \end{pmatrix} \\
&= \frac{T^3}{3} \mathbf{Tr} \sum_n \int \frac{d^2 p_1 d^2 p_2 d^2 p_3}{(2\pi)^6} \begin{pmatrix} g_1^{(e)} \sigma \cdot M_{12} & g_1^{(e)} \Delta_{12} \\ g_{-1}^{(h)} \bar{\Delta}_{21} & g_{-1}^{(h)} \sigma \cdot M_{12} \end{pmatrix} \\
&\quad \times \begin{pmatrix} g_2^{(e)} \sigma \cdot M_{23} & g_2^{(e)} \Delta_{23} \\ g_{-2}^{(h)} \bar{\Delta}_{32} & g_{-2}^{(h)} \sigma \cdot M_{23} \end{pmatrix} \begin{pmatrix} g_3^{(e)} \sigma \cdot M_{31} & g_3^{(e)} \Delta_{31} \\ g_{-3}^{(h)} \bar{\Delta}_{13} & g_{-3}^{(h)} \sigma \cdot M_{31} \end{pmatrix} \\
&= \frac{T^3}{3} \sum_n \int \frac{d^2 p_1 d^2 p_2 d^2 p_3}{(2\pi)^6} \mathbf{Tr} \begin{pmatrix} \mathcal{M}_{11} & \mathcal{M}_{12} \\ \mathcal{M}_{21} & \mathcal{M}_{22} \end{pmatrix}, \tag{5.25}
\end{aligned}$$

where

$$\begin{aligned}
\mathcal{M}_{11} &= g_1^{(e)} \Delta_{12} g_{-2}^{(h)} \bar{\Delta}_{32} g_3^{(e)} \sigma \cdot M_{31} + g_1^{(e)} \sigma \cdot M_{12} g_2^{(e)} \Delta_{23} g_{-3}^{(h)} \bar{\Delta}_{13} \\
&\quad + g_1^{(e)} \Delta_{12} g_{-2}^{(h)} \sigma \cdot M_{23} g_{-3}^{(h)} \bar{\Delta}_{13} + \dots, \tag{5.26}
\end{aligned}$$

$$\begin{aligned}
\mathcal{M}_{22} &= g_{-1}^{(h)} \bar{\Delta}_{21} g_2^{(e)} \sigma \cdot M_{23} g_3^{(e)} \Delta_{31} + g_{-1}^{(h)} \sigma \cdot M_{12} g_{-2}^{(h)} \bar{\Delta}_{32} g_3^{(e)} \Delta_{31} \\
&\quad + g_{-1}^{(h)} \bar{\Delta}_{21} g_2^{(e)} \Delta_{23} g_{-3}^{(h)} \sigma \cdot M_{31} + \dots \tag{5.27}
\end{aligned}$$

We just consider the leading term after expanding the Green funcion.

$$\begin{aligned}
& \text{tr}[g_1^{(e)} \Delta_{12} g_{-2}^{(h)} \bar{\Delta}_{32} g_3^{(e)} (\sigma \cdot \mathbf{M}_{31})] \\
&= \frac{1}{D(p_1, p_2, p_3)} \text{tr}[-\alpha(-i\omega_n + \xi_{p_1})(-i\omega_n - \xi_{-p_2}) \Delta_{12} \bar{\Delta}_{32} \mathbf{p}_3 \cdot \sigma (\sigma \cdot \mathbf{M}_{31}) + \dots \\
&\quad - \alpha^2(-i\omega_n + \xi_{p_3}) \mathbf{p}_1 \cdot \sigma \Delta_{12} \mathbf{p}_2 \cdot \sigma \bar{\Delta}_{32} (\sigma \cdot \mathbf{M}_{31}) \\
&\quad + \alpha^2(-i\omega_n - \xi_{-p_2}) \mathbf{p}_1 \cdot \sigma \Delta_{12} \mathbf{p}_3 \cdot \sigma \bar{\Delta}_{32} (\sigma \cdot \mathbf{M}_{31}) \\
&\quad - \alpha^2(-i\omega_n + \xi_{p_1}) \mathbf{p}_2 \cdot \sigma \Delta_{12} \mathbf{p}_3 \cdot \sigma \bar{\Delta}_{32} (\sigma \cdot \mathbf{M}_{31}) \\
&\quad - \alpha^3(\mathbf{p}_1 \cdot \sigma) \Delta_{12} (\mathbf{p}_2 \cdot \sigma) \bar{\Delta}_{32} (\mathbf{p}_3 \cdot \sigma) (\sigma \cdot \mathbf{M}_{31})]. \tag{5.28}
\end{aligned}$$

We replace the momentum $\left. \begin{matrix} p_1 \\ p_2 \end{matrix} \right\} \rightarrow \left\{ \begin{matrix} p - \frac{q_1}{2} \\ p + \frac{q_1}{2} \end{matrix} \right\}$, $\left. \begin{matrix} p_2 \\ p_3 \end{matrix} \right\} \rightarrow \left\{ \begin{matrix} p - \frac{q_2}{2} \\ p + \frac{q_2}{2} \end{matrix} \right\}$, $\left. \begin{matrix} p_3 \\ p_1 \end{matrix} \right\} \rightarrow$

$\left\{ \begin{matrix} p - \frac{q_3}{2} \\ p + \frac{q_3}{2} \end{matrix} \right\}$ and just focus on the dynamic term of order parameter which means

$q \cdot M_q = 0$ and $M_q = M_0$. Also $q_1 + q_2 + q_3 = 0$ can be obtained from $p_1 + p_2 + p_3 = 0$

and

$$\begin{aligned}
& \text{tr}[g_1^e \Delta_{12} g_{-2}^h \bar{\Delta}_{32} g_3^e (\boldsymbol{\sigma} \cdot \mathbf{M}_{31})] \\
&= \text{tr}[g_{p-\frac{q_1}{2}}^e \Delta_{q_1} g_{-p+\frac{q_2}{2}}^h \bar{\Delta}_{-q_2} g_3^e (\boldsymbol{\sigma} \cdot \mathbf{M}_{q_3})] \\
&= \frac{\text{tr}}{8} [(g_{p-\frac{q_1}{2},+}^e P_{p-\frac{q_1}{2},+} + g_{p-\frac{q_1}{2},-}^e P_{p-\frac{q_1}{2},-}) \Delta_{q_1} (g_{-p+\frac{q_2}{2},+}^h P_{-p+\frac{q_2}{2},+} + g_{p-\frac{q_1}{2},+}^e P_{p-\frac{q_1}{2},-}) \bar{\Delta}_{-q_2} \\
&\quad \times (g_{p-\frac{q_3}{2},+}^e P_{p-\frac{q_3}{2},+} + g_{p-\frac{q_3}{2},-}^e P_{p-\frac{q_3}{2},-}) (\boldsymbol{\sigma} \cdot \mathbf{M}_{q_3})] \\
&= \frac{\text{tr}}{8} \{ [g_{p-\frac{q_1}{2},+}^e (1 + \frac{(\mathbf{p} - \frac{\mathbf{q}_1}{2}) \cdot \boldsymbol{\sigma}}{|\mathbf{p} - \frac{\mathbf{q}_1}{2}|}) + g_{p-\frac{q_1}{2},-}^e (1 - \frac{(\mathbf{p} - \frac{\mathbf{q}_1}{2}) \cdot \boldsymbol{\sigma}}{|\mathbf{p} - \frac{\mathbf{q}_1}{2}|})] \Delta_{q_1} \\
&\quad \times [g_{-p+\frac{q_2}{2},+}^h (1 - \frac{(\mathbf{p} - \frac{\mathbf{q}_2}{2}) \cdot \boldsymbol{\sigma}}{|\mathbf{p} - \frac{\mathbf{q}_2}{2}|}) + g_{-p+\frac{q_2}{2},-}^h (1 + \frac{(\mathbf{p} - \frac{\mathbf{q}_2}{2}) \cdot \boldsymbol{\sigma}}{|\mathbf{p} - \frac{\mathbf{q}_2}{2}|})] \bar{\Delta}_{-q_2} \\
&\quad \times [g_{p-\frac{q_3}{2},+}^e (1 + \frac{(\mathbf{p} - \frac{\mathbf{q}_3}{2}) \cdot \boldsymbol{\sigma}}{|\mathbf{p} - \frac{\mathbf{q}_3}{2}|}) + g_{p-\frac{q_3}{2},-}^e (1 - \frac{(\mathbf{p} - \frac{\mathbf{q}_3}{2}) \cdot \boldsymbol{\sigma}}{|\mathbf{p} - \frac{\mathbf{q}_3}{2}|})] (\mathbf{M}_{q_3} \cdot \boldsymbol{\sigma}) \} \\
&= \frac{\text{tr}}{8} \{ [(g_{p-\frac{q_1}{2},+}^e + g_{p-\frac{q_1}{2},-}^e) + (g_{p-\frac{q_1}{2},+}^e - g_{p-\frac{q_1}{2},-}^e) \frac{(\mathbf{p} - \frac{\mathbf{q}_1}{2}) \cdot \boldsymbol{\sigma}}{|\mathbf{p} - \frac{\mathbf{q}_1}{2}|}] \Delta_{q_1} \\
&\quad \times [(g_{-p+\frac{q_2}{2},+}^h + g_{-p+\frac{q_2}{2},-}^h) - (g_{-p+\frac{q_2}{2},+}^h - g_{-p+\frac{q_2}{2},-}^h) \frac{(\mathbf{p} - \frac{\mathbf{q}_2}{2}) \cdot \boldsymbol{\sigma}}{|\mathbf{p} - \frac{\mathbf{q}_2}{2}|}] \bar{\Delta}_{-q_2} \\
&\quad \times [(g_{p-\frac{q_3}{2},+}^e + g_{p-\frac{q_3}{2},-}^e) + (g_{p-\frac{q_3}{2},+}^e - g_{p-\frac{q_3}{2},-}^e) \frac{(\mathbf{p} - \frac{\mathbf{q}_3}{2}) \cdot \boldsymbol{\sigma}}{|\mathbf{p} - \frac{\mathbf{q}_3}{2}|}] (\mathbf{M}_{q_3} \cdot \boldsymbol{\sigma}) \}
\end{aligned}$$

$$\begin{aligned}
&= \frac{\text{tr}}{4} \{ [(g_{p-\frac{q_1}{2},+}^e + g_{p-\frac{q_1}{2},-}^e)(g_{-p+\frac{q_2}{2},+}^h + g_{-p+\frac{q_2}{2},-}^h)(g_{p-\frac{q_3}{2},+}^e - g_{p-\frac{q_3}{2},-}^e) \Delta_{q_1} \bar{\Delta}_{q_2} \frac{(\mathbf{p} - \frac{\mathbf{q}_3)}{2}) \cdot \mathbf{M}_{q_3}}{|\mathbf{p} - \frac{\mathbf{q}_3}{2}|} \\
&\quad - (g_{p-\frac{q_1}{2},+}^e + g_{p-\frac{q_1}{2},-}^e)(g_{-p+\frac{q_2}{2},+}^h - g_{-p+\frac{q_2}{2},-}^h)(g_{p-\frac{q_3}{2},+}^e + g_{p-\frac{q_3}{2},-}^e) \Delta_{q_1} \bar{\Delta}_{q_2} \frac{(\mathbf{p} - \frac{\mathbf{q}_2)}{2}) \cdot \mathbf{M}_{q_3}}{|\mathbf{p} - \frac{\mathbf{q}_2}{2}|} \\
&\quad + (g_{p-\frac{q_1}{2},+}^e - g_{p-\frac{q_1}{2},-}^e)(g_{-p+\frac{q_2}{2},+}^h + g_{-p+\frac{q_2}{2},-}^h)(g_{p-\frac{q_3}{2},+}^e + g_{p-\frac{q_3}{2},-}^e) \Delta_{q_1} \bar{\Delta}_{q_2} \frac{(\mathbf{p} - \frac{\mathbf{q}_1)}{2}) \cdot \mathbf{M}_{q_3}}{|\mathbf{p} - \frac{\mathbf{q}_1}{2}|} \\
&\quad - (g_{p-\frac{q_1}{2},+}^e - g_{p-\frac{q_1}{2},-}^e)(g_{-p+\frac{q_2}{2},+}^h - g_{-p+\frac{q_2}{2},-}^h)(g_{p-\frac{q_3}{2},+}^e + g_{p-\frac{q_3}{2},-}^e) \\
&\quad \times \frac{i\varepsilon_{ijk}(p - \frac{q_1}{2})_i \Delta_{q_1} (p - \frac{q_2}{2})_j \bar{\Delta}_{-q_2} \mathbf{M}_{q_3,k}}{|\mathbf{p} - \frac{\mathbf{q}_1}{2}| |\mathbf{p} - \frac{\mathbf{q}_2}{2}|} \\
&\quad - (g_{p-\frac{q_1}{2},+}^e + g_{p-\frac{q_1}{2},-}^e)(g_{-p+\frac{q_2}{2},+}^h - g_{-p+\frac{q_2}{2},-}^h)(g_{p-\frac{q_3}{2},+}^e - g_{p-\frac{q_3}{2},-}^e) \\
&\quad \times \frac{i\varepsilon_{ijk} \Delta_{q_1} (p - \frac{q_2}{2})_i \bar{\Delta}_{-q_2} (p - \frac{q_3}{2})_j \mathbf{M}_{q_3,k}}{|\mathbf{p} - \frac{\mathbf{q}_1}{2}| |\mathbf{p} - \frac{\mathbf{q}_2}{2}|} \\
&\quad + (g_{p-\frac{q_1}{2},+}^e - g_{p-\frac{q_1}{2},-}^e)(g_{-p+\frac{q_2}{2},+}^h + g_{-p+\frac{q_2}{2},-}^h)(g_{p-\frac{q_3}{2},+}^e - g_{p-\frac{q_3}{2},-}^e) \\
&\quad \times \frac{i\varepsilon_{ijk}(p - \frac{q_1}{2})_i \Delta_{q_1} \bar{\Delta}_{-q_2} (p - \frac{q_3}{2})_j \mathbf{M}_{q_3,k}}{|\mathbf{p} - \frac{\mathbf{q}_1}{2}| |\mathbf{p} - \frac{\mathbf{q}_3}{2}|} \\
&\quad - (g_{p-\frac{q_1}{2},+}^e - g_{p-\frac{q_1}{2},-}^e)(g_{-p+\frac{q_2}{2},+}^h - g_{-p+\frac{q_2}{2},-}^h)(g_{p-\frac{q_3}{2},+}^e - g_{p-\frac{q_3}{2},-}^e) \\
&\quad \times \frac{(\delta_{ij}\delta_{kl} - \delta_{ik}\delta_{jl} + \delta_{il}\delta_{jk}) \Delta_{q_1} \bar{\Delta}_{-q_2} (p - \frac{q_1}{2})_i (p - \frac{q_2}{2})_j (p - \frac{q_3}{2})_k M_{q_3,l}}{|\mathbf{p} - \frac{\mathbf{q}_1}{2}| |\mathbf{p} - \frac{\mathbf{q}_2}{2}| |\mathbf{p} - \frac{\mathbf{q}_3}{2}|} \quad (5.29)
\end{aligned}$$

Then

$$\begin{aligned}
&(\delta_{ij}\delta_{kl} - \delta_{ik}\delta_{jl} + \delta_{il}\delta_{jk}) \Delta_{q_1} \bar{\Delta}_{-q_2} (p - \frac{q_1}{2})_i (p - \frac{q_2}{2})_j (p - \frac{q_3}{2})_k M_{q_3,l} \\
&= \Delta_{q_1} \bar{\Delta}_{-q_2} [(\mathbf{p} - \frac{\mathbf{q}_1}{2}) \cdot (\mathbf{p} - \frac{\mathbf{q}_2}{2})][(\mathbf{p} - \frac{\mathbf{q}_3}{2}) \cdot \mathbf{M}_{q_3}] \\
&\quad - \Delta_{q_1} \bar{\Delta}_{-q_2} [(\mathbf{p} - \frac{\mathbf{q}_1}{2}) \cdot (\mathbf{p} - \frac{\mathbf{q}_3}{2})][(\mathbf{p} - \frac{\mathbf{q}_2}{2}) \cdot \mathbf{M}_{q_3}] \\
&\quad + \Delta_{q_1} \bar{\Delta}_{-q_2} [(\mathbf{p} - \frac{\mathbf{q}_2}{2}) \cdot (\mathbf{p} - \frac{\mathbf{q}_3}{2})][(\mathbf{p} - \frac{\mathbf{q}_1}{2}) \cdot \mathbf{M}_{q_3}]. \quad (5.30)
\end{aligned}$$

We do summation over p . It is easy to prove that the gauge violent term is equal to zero(One method is just from the notation we choose, another is $\nabla \cdot (\nabla \times \vec{A}_M) = 0$.

) The Hermite conjugate term is

$$\begin{aligned} \text{tr}[g_{-1}^{(h)} \bar{\Delta}_{21} g_2^{(e)} \Delta_{23} g_{-3}^{(h)} (\sigma \cdot M_{13})] &\rightarrow -\frac{i}{2} \alpha^2 [2g_{0,p}^{(e)2} g_{0,-p}^{(h)3} \varepsilon_{ijk} q_{1,i} \bar{\Delta}_{-q_1} q_{2,j} \Delta_{q_2} M_{q_3,k} \\ &+ g_{0,-p}^{(h)4} g_{0,p}^{(e)} q_{1,i} \bar{\Delta}_{-q_1} q_{2,j} \Delta_{q_2} M_{q_3,k}]. \end{aligned} \quad (5.31)$$

By the permutation $1 \rightarrow 2 \rightarrow 3 \rightarrow 1$, the free energy $F_{\bar{\Delta}\Delta M}$ is

$$\begin{aligned} S_3 &= \beta F_{\bar{\Delta}\Delta M} \\ &= -\frac{T^3}{L^6} \sum_{n,p,\{q_i\}} \frac{i}{2} \alpha^2 \varepsilon_{ijk} (2g_{0,p}^{(e)3} g_{0,-p}^{(h)2} + g_{0,p}^{(e)4} g_{0,-p}^{(h)}) q_{1,i} \Delta_{q_1} q_{2,j} \bar{\Delta}_{-q_2} M_{q_3,k} + h.c.) \\ &\quad \times \delta(q_1 + q_2 + q_3). \end{aligned} \quad (5.32)$$

In position space,

$$F_{\bar{\Delta}\Delta M} = \int d^2r [i\gamma (\vec{\partial} \bar{\Delta} \times \vec{\partial} \Delta) \cdot M] \quad (5.33)$$

where,

$$\begin{aligned}
\gamma &= T \frac{\alpha^2 T^3}{2} \sum_n \int \frac{d^2 p}{(2\pi)^2} [2(g_{0,p}^{(e)3} g_{0,-p}^{(h)2} - g_{0,-p}^{(h)3} g_{0,p}^{(e)2}) \\
&\quad + (g_{0,p}^{(e)4} g_{0,-p}^{(h)} - g_{0,-p}^{(h)4} g_{0,p}^{(e)})] \\
&= \frac{\alpha^2 T^4}{2} \sum_n \int \frac{\pi dp^2}{4\pi^2} \left[\frac{4\xi_p}{(\omega_n^2 + \xi_p^2)^3} + \frac{2\xi_p(3\omega_n^2 - \xi_p^2)}{(\omega_n^2 + \xi_p^2)^4} \right] \\
&= \frac{2m\alpha^2 T^4}{8\pi} \sum_n \int_0^\infty d\xi_p \left[\frac{4\xi_p}{(\omega_n^2 + \xi_p^2)^3} + \frac{2\xi_p(3\omega_n^2 - \xi_p^2)}{(\omega_n^2 + \xi_p^2)^4} \right] \\
&= \frac{m\alpha^2 T^4}{4\pi} \sum_n \int_0^\infty d\xi_p^2 \left[\frac{2}{(\omega_n^2 + \xi_p^2)^3} + \frac{(3\omega_n^2 - \xi_p^2)}{(\omega_n^2 + \xi_p^2)^4} \right] \\
&= \frac{m\alpha^2 T^4}{4\pi} \sum_n \int_0^\infty d\xi_p^2 \frac{5\omega_n^2 + \xi_p^2}{(\omega_n^2 + \xi_p^2)^4} \\
&= \frac{m\alpha^2 T^4}{4\pi} \sum_n \frac{7}{6\omega_n^2} \\
&= \frac{m\alpha^2 T^4}{4\pi} \sum_n \frac{7\beta^2}{6(2\pi)^2} \frac{1}{(2n+1)^2} = \frac{7m\alpha^2 T^2}{768\pi L^6}. \tag{5.34}
\end{aligned}$$

With this approximation, if we rescale the Free energy and get J back,

$$F = \int d^2 r [(\partial \bar{\Delta})(\partial \Delta) + a(\bar{\Delta} \Delta) + \frac{b}{2}(\bar{\Delta} \Delta)^2 + i\gamma'(\vec{\partial} \bar{\Delta} \times \vec{\partial} \Delta) \cdot M] \tag{5.35}$$

where $\gamma' = \frac{\gamma}{c} = \frac{7L^2 m \alpha^2 J T}{12}$.

5.2.3 The fourth order perturbation

Fourth order perturbative calculation will give us the quadratic term of Δ and the term $(\bar{\Delta}\Delta)(M \cdot M)$.

$$\begin{aligned}
S_4 &= \frac{1}{4} \frac{T^4}{L^8} \text{Tr}(\mathcal{G}_0 \Sigma \mathcal{G}_0 \Sigma \mathcal{G}_0 \Sigma \mathcal{G}_0 \Sigma) \\
&= \frac{1}{4} \frac{T^4}{L^8} \text{Tr} \begin{pmatrix} g_1^{(e)} & 0 \\ 0 & g_{-1}^{(h)} \end{pmatrix} \begin{pmatrix} \sigma \cdot M_{12} & \Delta_{12} \\ \bar{\Delta}_{21} & \sigma \cdot M_{12} \end{pmatrix} \\
&\quad \cdot \begin{pmatrix} g_2^{(e)} & 0 \\ 0 & g_{-1}^{(h)} \end{pmatrix} \begin{pmatrix} \sigma \cdot M_{23} & \Delta_{23} \\ \bar{\Delta}_{32} & \sigma \cdot M \end{pmatrix} \\
&\quad \cdot \begin{pmatrix} g_3^{(e)} & 0 \\ 0 & g_{-3}^{(h)} \end{pmatrix} \begin{pmatrix} \sigma \cdot M_{34} & \Delta_{34} \\ \bar{\Delta}_{43} & \sigma \cdot M_{34} \end{pmatrix} \\
&\quad \cdot \begin{pmatrix} g_4^{(e)} & 0 \\ 0 & g_{-4}^{(h)} \end{pmatrix} \begin{pmatrix} \sigma \cdot M_{41} & \Delta_{41} \\ \bar{\Delta}_{14} & \sigma \cdot M_{41} \end{pmatrix} \\
&= \frac{1}{4} \frac{T^4}{L^8} \text{Tr} \begin{pmatrix} g_1^{(e)} \sigma \cdot M_{12} & g_1^{(e)} \Delta_{12} \\ g_{-1}^{(h)} \bar{\Delta}_{21} & g_{-1}^{(h)} \sigma \cdot M_{12} \end{pmatrix} \begin{pmatrix} g_2^{(e)} \sigma \cdot M_{23} & g_2^{(e)} \Delta_{23} \\ g_{-2}^{(h)} \bar{\Delta}_{32} & g_{-2}^{(h)} \sigma \cdot M_{23} \end{pmatrix} \\
&\quad \cdot \begin{pmatrix} g_3^{(e)} \sigma \cdot M_{34} & g_3^{(e)} \Delta_{34} \\ g_{-3}^{(h)} \bar{\Delta}_{43} & g_{-3}^{(h)} \sigma \cdot M_{34} \end{pmatrix} \begin{pmatrix} g_4^{(e)} \sigma \cdot M_{41} & g_4^{(e)} \Delta_{41} \\ g_{-4}^{(h)} \bar{\Delta}_{14} & g_{-4}^{(h)} \sigma \cdot M_{41} \end{pmatrix}
\end{aligned} \tag{5.36}$$

We use mean field theory $J^2(\bar{\Delta}\Delta)\langle M \cdot M \rangle$ to replace $J^2(\bar{\Delta}\Delta)(M \cdot M)$. The fourth order is

$$F_4 = \frac{7mT^2g^4}{256\pi^3c} \zeta(3) \int d^2r (\bar{\Delta}\Delta)^2 \tag{5.37}$$

So, $b = \frac{7mT^2g^4}{128\pi^3} \zeta(3) \frac{64\pi L^2}{g^2T} = \frac{7mg^2TL^2}{2\pi^2} \zeta(3)$. With the assumption $\alpha \ll J \sim g < 1$, γ' term can be treated as the perturbative interaction.

5.3 Ginzburg-Landau equations

The improminent parts of the free energy of order parameter and skyrmion spin textures is $F_2 + F_3$,

$$F_{\bar{\Delta}\Delta M} = \int d^2r [c(\partial_i \bar{\Delta})(\partial_i \Delta) + a(\bar{\Delta}\Delta) + \frac{b}{2}(\bar{\Delta}\Delta)^2] + i\gamma[(\vec{\partial} \bar{\Delta} \times \vec{\partial} \Delta) \cdot \mathbf{M}] + \dots \quad (5.38)$$

To get the equation of motion of Δ , $\frac{\delta F}{\delta \Delta} = 0$. Then

$$-\partial^2 \Delta + a\Delta + b(\bar{\Delta}\Delta)\Delta + i\gamma' \varepsilon_{ijk} \partial_i \Delta \partial_j M_k = 0 \quad (5.39)$$

where $\partial^2 = \partial_x^2 + \partial_y^2$ and $\Delta = \Delta(x, y)$. For further simplifying,

$$-\partial^2 \Delta + a\Delta + b(\bar{\Delta}\Delta)\Delta + i \frac{4\gamma' R^2}{(r^2 + R^2)^2} (y\partial_x \Delta - x\partial_y \Delta) = 0. \quad (5.40)$$

To the off center situation

$$-\partial^2 \Delta + a\Delta + b(\bar{\Delta}\Delta)\Delta + i \frac{4\gamma' R^2}{(r^2 + R^2)^2} [(y - r_0)\partial_x \Delta - (x - r_0)\partial_y \Delta] = 0. \quad (5.41)$$

By defining $\eta = x + iy$, $\bar{\eta} = x - iy$, it is easy to get $\partial_x = \partial_\eta + \partial_{\bar{\eta}}$, $\partial_y = i(\partial_\eta - \partial_{\bar{\eta}})$ and $x = \frac{1}{2}(\eta + \bar{\eta})$, $y = \frac{1}{2i}(\eta - \bar{\eta})$. So the Eqn of motion can be rewritten as

$$-\frac{4\partial^2}{\partial\eta\partial\bar{\eta}} \Delta + a\Delta + b(\bar{\Delta}\Delta)\Delta + \frac{4\gamma' R^2}{(\bar{\eta}\eta + R^2)^2} (\eta \frac{\partial}{\partial\eta} - \bar{\eta} \frac{\partial}{\partial\bar{\eta}}) \Delta = 0. \quad (5.42)$$

Turning to polar coordinates,

$$-\frac{1}{r} \frac{\partial}{\partial r} (r \frac{\partial}{\partial r} \Delta) - \frac{1}{r^2} \frac{\partial^2}{\partial \theta^2} \Delta + a\Delta + b(\bar{\Delta}\Delta)\Delta - \frac{8i\gamma' R^2}{(r^2 + R^2)^2} \frac{\partial}{\partial \theta} \Delta = 0. \quad (5.43)$$

The off center situation is

$x = r \cos \theta$, $y = r \sin \theta$, $r'^2 = (r \cos \theta - r_0)^2 + (r \sin \theta - r_0)^2 = r^2 + r_0^2 - 2rr_0(\cos \theta + \sin \theta)$ So

$$-\frac{1}{r} \frac{\partial}{\partial r} \left(r \frac{\partial}{\partial r} \Delta \right) - \frac{1}{r^2} \frac{\partial^2}{\partial \theta^2} \Delta + a\Delta + b(\bar{\Delta}\Delta)\Delta - \frac{8i\gamma'R^2}{(r'^2 + R^2)^2} \frac{\partial}{\partial \theta} \Delta = 0. \quad (5.44)$$

By solving the equations, how the skyrmions affect the vortex can be achieved.

5.4 Discussion

The proximity effect between superconductors and magnetic materials has been studied in various combinations[146, 147, 148, 149]. The interaction between vortices in Type-II superconductor and skyrmions is studied in some special situations[150, 151]. The structural similarity of the vortices in Type-II superconductors and skyrmions[152] inspire us to study the dynamics of the vortices and skyrmions in general case. In the above calculation, we assume the skyrmions are robust. As a consequence, the spin textures of Bloch type skyrmion is introduced directly into the Ginzburg-Landau equations. We can also put the interaction $(\vec{\partial} \bar{\Delta} \times \vec{\partial} \Delta) \cdot \mathbf{M}$ into the Hamiltonian of chiral magnets and get the Landau-Lifshitz-Gilbert equation[153, 154]. By solving both Ginzburg-Landau equation and Ginzburg-Landau equation, more physical phenomena are expected. The spin-orbit coupling is considered in the calculation because the superconductor is non-centrosymmetric as we assumed. At the same time, chiral magnets which host the skyrmions also lack the inversion symmetry. This breaking inversion symmetry in 2D system makes more nontrivial topological structures expected to be found in non-centrosymmetric materials.

CHAPTER VI

Summary and future directions

In this thesis, we investigated the topological charges of several magnetic systems which have the Dzyaloshinskii–Moriya(DM) interactions. Firstly, we make a historical description of the study on chiral magnets, especially the skyrmion physics therein. Then we pointed out that the topological charge which was used to identify the skyrmions is directly relevant to the topological Hall effect. So understanding the topological charge is important to the transport properties of chiral magnets.

Then we study the two-dimensional chiral magnetic system. In this system, the Heisenberg interaction is ferromagnetic interaction. We employed Monte Carlo method to calculate the topological charge on a square lattice. A $B - T$ diagram of topological charge is shown . Several points in the $B - T$ diagram are chosen to take the snapshots to study the phases. The results show that the maximum absolute value of the topological charge does not correspond to the skyrmion crystal phases. The phase with the maximum absolute value of the topological charge is a random phase. Then we made an analysis on one triangle to understand the physics well. The analysis show the external magnetic field lifts the energy degeneracy of triangles with opposite spins on the vertices of the triangles It leads to the conclusion that the thermal average of the topological charge, which is replaced

by triple product of the three spins on the vertices, is no longer zero and the topological charge scales as $Q \propto \frac{D^2 B}{T^3}$ at high temperature, where D is the magnitude of the DM interaction, B is the strength of the external magnetic field and T is the temperature. It matches the results from the Monte Carlo simulation. At a fixed high temperature, when D is fixed $Q \propto B$ and when B is fixed, $Q \propto D^2$. Then we performed a field theoretical calculation of the topological charge through CP^1 model. In the CP^1 model, there is an emergent gauge field whose curl is the density of the topological charge. The curl of the emergent gauge field is the emergent magnetic field. We calculated the effective action of the emergent magnetic field and get the saddle point value of the emergent magnetic field to estimate the topological charge. At high temperature, the analytical result matches the analysis of the physical picture on one triangle and the numerical calculation well. An experimental work on thin film SrRuO_3 confirmed our theoretical results.

Then we extend our calculation into three-dimensional system. The Monte Carlo simulation and the field theoretical calculation through CP^1 model are performed. At high temperature, there is still nonzero topological charge. There is one more question need to be clarified is that in three-dimensional case, the thickness dependent issue. We investigated the topological charges with different thicknesses or layers in the direction of the external magnetic field. Both numerical and analytical method were used to investigate this issue. An explanation based on a physical picture of magnons in the box can explain the phenomena related to the thickness of the sample. The SrRuO_3 experiments cannot confirm our theoretical results because the effective DM interaction is induced by the interface of SrRuO_3 and SrTiO_3 , the effective DM interaction is inversely proportional to the thickness. When the sample is thick enough, the effective DM interaction is too weak to host this nontrivial topology. However, our model is used to describe the homogenous chiral magnets which have the constant DM interaction.

Here, we would like to mention that so far the topological hall effect is still regarded as the best transport signature of the skyrmions. But in the past, topological Hall effect is misused to identify the skyrmions. The value of our work is to provide a new mechanism of the topological Hall effect can be induced by the thermal fluctuation without skyrmions.

Our works are not limited to non-centrosymmetric ferromagnets. A work on the two-dimensional hexagonal frustrated magnets have been reviewed to show that the non-zero topological charge can also exist in the system with antiferromagnetic Heisenberg interaction. The DM interaction in this system breaks the inversion symmetry. The topological charge in this system has the similar pattern of the chiral magnets. Then we investigate the staggered DM interaction system which is centrosymmetric. The giant non-zero topological charge exists at very low temperature, By our analysis, the reason is from the speciality of spin textures at ground state. The linear relationship between the topological charge and topological Hall resistivity is doubted here because the adiabatic approximation may fail to describe the motion of conductive electrons with the staggered spin textures at low temperature. The work about proximity effect between type-II superconductor and skyrmion materials is introduced finally. This work gives a open question what will happen in the non-centrosymmetric systems.

As mentioned above, the relationship between the topological charge and topological resistivity in various magnetic systems is worth investigating, especially in the systems with antiferromagnetic Heisenberg interaction. Moreover, whether the breaking the inversion symmetry is necessary to the nonzero topological charge is still needed to prove. Also we hope the experiments can confirm or fight against our theoretical results.

APPENDICES

APPENDIX A

The program for calculating the Hall conductivity

The program for calculating the hall conductivity is written by Python. For a compact appearance, the program does not follow the standard indentation in Python.

```
from numba import cuda, float64, njit
import numpy as np
import math
```

```
H_T = -100.0 # hopping constant
H_J = -100.0 # Hund's coupling
ETA = 1.0
MU = -80.0 # Fermi energy
```

```
N_LX: int = 32
```

```

N_LY: int = 32
N_SPINS: int = N_LX*N_LY    #lattice size
N2_SPINS: int = 2*N_SPINS  #matrix size of the Hamiltonian

TpB: int = 256
TpB_2D = (8, 8)
NBlock: int = (N_SPINS+TpB - 1)//TpB
NBlock_2D = (N_SUB//8, N_SUB//8)
NBlock_2D_a = (N_SUB//8, N_SPINS//8) #GPU block size

Path="" #The path of the spin texture files
Temperatures=[]

@cuda.reduce
def reduce_sum(a, b):
    return a + b

cuda.jit(device=True, inline=True)
def fermi_cuda(e, t):
    return 1.0/(math.exp((e-MU)/t) + 1) #Fermi distribution function

@cuda.jit
def get_sigma_cuda(e, u, ux, uy, sxx, sxy, t):
    m, n = cuda.grid(2)
    sh_sxx = cuda.shared.array((8, 8), dtype=float64)

```

```

sh_sxy = cuda.shared.array((8, 8), dtype=float64)
tx, ty = cuda.threadIdx.x, cuda.threadIdx.y
bx, by = cuda.blockIdx.x, cuda.blockIdx.y
gx = cuda.gridDim.x
jx, jy = 0.0, 0.0
fac = 0.0
#initialization

if m != n:
    fac = (fermi_cuda(e[n], t)-fermi_cuda(e[m], t))\
        / (ETA*ETA+(e[n]-e[m])*(e[n]-e[m]))
    for iis in range(N_SPINS):
        jx += u[iis, m].conjugate()*ux[iis, n]\
            - u[iis, n]*ux[iis, m].conjugate()\
            + u[iis+N_SPINS, m].conjugate()*ux[iis+N_SPINS, n]\
            - u[iis+N_SPINS, n]*ux[iis+N_SPINS, m].conjugate()
        jy += u[iis, m].conjugate()*uy[iis, n]\
            - u[iis, n]*uy[iis, m].conjugate()\
            + u[iis+N_SPINS, m].conjugate()*uy[iis+N_SPINS, n]\
            - u[iis+N_SPINS, n]*uy[iis+N_SPINS, m].conjugate()
        sh_sxx[tx, ty] = fac*(jx.conjugate()\
            * jx/complex(e[m]-e[n], ETA)).real
        sh_sxy[tx, ty] = -fac*(jx*jy.conjugate()).imag
    else:
        sh_sxx[tx, ty] = 0.0
        sh_sxy[tx, ty] = 0.0
    cuda.syncthreads()

```

```

#GPU summation
    if ty % 2 == 0:
        sh_sxx[tx, ty] += sh_sxx[tx, ty + 1]
    else:
        sh_sxy[tx, ty] += sh_sxy[tx, ty - 1]
    cuda.syncthreads()
    if ty % 4 == 0:
        sh_sxx[tx, ty] += sh_sxx[tx, ty + 2]
    elif ty % 4 == 3:
        sh_sxy[tx, ty] += sh_sxy[tx, ty - 2]
    cuda.syncthreads()
    if tx % 2 == 0:
        sh_sxx[tx, ty] += sh_sxx[tx + 1, ty]
    else:
        sh_sxy[tx, ty] += sh_sxy[tx - 1, ty]
    cuda.syncthreads()
    if tx % 4 == 0:
        sh_sxx[tx, ty] += sh_sxx[tx + 2, ty]
    elif tx % 4 == 3:
        sh_sxy[tx, ty] += sh_sxy[tx - 2, ty]
    cuda.syncthreads()
    if (tx == 0) and (ty == 0):
        sxx[bx + gx * by] = sh_sxx[0, 0]+sh_sxx[0, 4]\
            + sh_sxx[4, 0]+sh_sxx[4, 4]
    elif (tx == 3) and (ty == 3):
        sxy[bx + gx * by] = sh_sxy[3, 3]+sh_sxy[3, 7]\
            + sh_sxy[7, 3]+sh_sxy[7, 7]

@cuda.jit

```

```

def get_un_cuda(u, nbs, ux, uy):
    i, iis = cuda.grid(2)
    nbx, nby = 0, 0
    if iis < N_SPINS:
        nbx = nbs[iis, 0]
        nby = nbs[iis, 2]
    cuda.syncthreads()
    if (i < N2_SPINS) and (iis < N_SPINS):
        if iis + 1 == nbx:
            ux[iis, i] = u[nbx, i]
            ux[iis + N_SPINS, i] = u[nbx + N_SPINS, i]
        if iis + 32 == nby:
            uy[iis, i] = u[nby, i]
            uy[iis + N_SPINS, i] = u[nby + N_SPINS, i]

@cuda.jit
def get_hamiltonian_cuda(ham, nbs, sp):
    i = cuda.grid(1)
    if i < N_SPINS:
        if i + 1 == nbs[i, 0]:
            ham[i, nbs[i, 0]] = H_T
            ham[i+N_SPINS, nbs[i, 0]+N_SPINS] = H_T
        if i - 1 == nbs[i, 1]:
            ham[i, nbs[i, 1]] = H_T
            ham[i+N_SPINS, nbs[i, 1]+N_SPINS] = H_T
        if i + NLX == nbs[i, 2]:
            ham[i, nbs[i, 2]] = H_T
            ham[i+N_SPINS, nbs[i, 2]+N_SPINS] = H_T

```

```

        if i - NLX == nbs[i,3]:
            ham[i, nbs[i, 3]] = H_T
            ham[i+N_SPINS, nbs[i, 3]+N_SPINS] = H_T
    cuda.syncthreads()
    if i < N_SPINS:
        ham[i, i] += H_J*sp[i, 5]
        ham[i+N_SPINS, i+N_SPINS] += -H_J*sp[i, 5]
        ham[i, i+N_SPINS] += H_J*complex(sp[i, 3], -sp[i, 4])
        ham[i+N_SPINS, i] += H_J*complex(sp[i, 3], sp[i, 4])

import numpy as np
from numba.cuda.cudadrv.devicearray import DeviceNDArray
from datetime import datetime
import os from THC import *

start = datetime.now() #timing
nbs_data =np.loadtxt()
# the information of spin texture files in ()

neighbors = np.zeros((N_SPINS, 4), dtype=np.int32)
for i in range(N_SPINS):
    neighbors[i] = list(map(np.float64, nbs_data[i, 1].split()))
    nbs_d = cuda.to_device(neighbors)
    print('neighbors shape = {0}'.format(neighbors.shape))
    sigma_xx_d:\
DeviceNDArray = cuda.device_array(NREDUCE)
    sigma_xy_d:\
DeviceNDArray = cuda.device_array(NREDUCE)

```

```

e_d: DeviceNDArray = cuda.device_array(N_SUB)
u_d: DeviceNDArray = cuda.device_array((N2_SPINS, N_SUB))
ux_d: DeviceNDArray = cuda.device_array((N2_SPINS, N_SUB))
uy_d: DeviceNDArray = cuda.device_array((N2_SPINS, N_SUB))

for temperature in Temperatures:
    sigma_xx_sum: float = 0.0
    sigma_xy_sum: float = 0.0
    sigma_yy_sum: float = 0.0
    sigma_xx_sq: float = 0.0
    sigma_xy_sq: float = 0.0
    sigma_xx: float = 0.0
    sigma_xy: float = 0.0
    sigma_yy: float = 0.0
    files = []
    #read the spin texture files
    n_f = len(files)
    print(temperature, n_f)

for file in files:
    # read spins
    spins_data = np.loadtxt()
    # spin texture files in ()
    spins_d = cuda.to_device(spins_data)
    ham_ = np.zeros((N2_SPINS, N2_SPINS))
    #hopping
    get_hamiltonian_cuda[NBlock, TpB]\

```

```

(ham_, nbs_d, spins_d)

e_, u_ = np.linalg.eigh(ham_)
#diagonalize the Hamiltonian
e_d = cuda.to_device(e_[LBEGIN:IEND])
u_d = cuda.to_device\
(np.ascontiguousarray(u_[:, LBEGIN:IEND]))

get_un_cuda[NBlock_2D_a, TpB_2D]\
(u_d, nbs_d, ux_d, uy_d)
get_sigma_cuda[NBlock_2D, TpB_2D]\
(e_d, u_d, ux_d, uy_d,\
sigma_xx_d, sigma_xy_d, temperature)

sigma_xx = reduce_sum(sigma_xx_d) * H.T*H.T * ETA / N_SPINS
sigma_xy = reduce_sum(sigma_xy_d) * H.T*H.T / N_SPINS
sigma_xx_sum += sigma_xx
sigma_xy_sum += sigma_xy
sigma_xx_sq += sigma_xx*sigma_xx
sigma_xy_sq += sigma_xy*sigma_xy

#output
print(sigma_xx, sigma_xy)
print(date.now()-datetime)

sigma_xx_sum /= n_f
sigma_xy_sum /= n_f

```

```
sigma_xx_sq /= n_f
sigma_xy_sq /= n_f
sigma_xx_err = sigma_xx_sq - sigma_xx_sum*sigma_xx_sum
sigma_xy_err = sigma_xy_sq - sigma_xy_sum*sigma_xy_sum
print(temperature , sigma_xx_sum , sigma_xx_err , \
      sigma_xy_sum , sigma_xy_err))
```

APPENDIX B

Metropolis program for calculating the topological charge in a staggered DM system

The program is written by *Mathematica*.

```
Array[s, 15, {1, 15}>(* spins*)
```

```
Array[EN, 1000000, {1, 1000000}];(* energy*)
```

```
Array[TC, 1000000, {1, 1000000}];(* Topological Charge*)
```

```
Array[ZW, 1000000, {1, 1000000}];(* weight :ZW=exp(-EN/T)*)
```

```
s0 = {s[1], s[2], s[3]}
```

```
s1 = {s[4], s[5], s[6]}
```

```
s2 = {s[7], s[8], s[9]}
```

```
s3 = {s[10], s[11], s[12]}
```

```
s4 = {s[13], s[14], s[15]}(* spins*)
```

```
(*T=1 j=1 d=0.5 h=0.5 max:number of steps*)
```

```

For[max = 10000, max <= 10001, max = max + 1000,
  Z = 0;(* partition function*)
  Q = 0;
  For[j = 1, j < max + 1, j++,
    For[i = 1, i < 16, i = i + 3,
      ri = 2.0;
      While[ri >= 1.0,
        rx = RandomReal[{-1, 1}];
        ry = RandomReal[{-1, 1}];
        ri = rx^2 + ry^2];
      rk = \[Sqrt](1 - ri);
      s[i] = 2*rx*rk;
      s[i + 1] = 2*ry*rk;
      s[i + 2] = 1 - 2*ri;
    ];
  ];

```

Bibliography

- [1] Michael Victor Berry. “Quantal phase factors accompanying adiabatic changes”. In: *Proceedings of the Royal Society of London. A. Mathematical and Physical Sciences* 392.1802 (1984), pp. 45–57.
- [2] K v Klitzing, Gerhard Dorda, and Michael Pepper. “New method for high-accuracy determination of the fine-structure constant based on quantized Hall resistance”. In: *Physical Review Letters* 45.6 (1980), p. 494.
- [3] Xiao-Liang Qi and Shou-Cheng Zhang. “Topological insulators and superconductors”. In: *Reviews of Modern Physics* 83.4 (2011), p. 1057.
- [4] M Zahid Hasan and Charles L Kane. “Colloquium: topological insulators”. In: *Reviews of modern physics* 82.4 (2010), p. 3045.
- [5] Naoto Nagaosa et al. “Anomalous hall effect”. In: *Reviews of modern physics* 82.2 (2010), p. 1539.
- [6] Alex Hubert and Rudolf Schäfer. *Magnetic domains: the analysis of magnetic microstructures*. Springer Science & Business Media, 2008.
- [7] T Shinjo et al. “Magnetic vortex core observation in circular dots of permalloy”. In: *Science* 289.5481 (2000), pp. 930–932.
- [8] M Tsoi, RE Fontana, and SSP Parkin. “Magnetic domain wall motion triggered by an electric current”. In: *Applied physics letters* 83.13 (2003), pp. 2617–2619.
- [9] Ulrich K Roessler, AN Bogdanov, and C Pfleiderer. “Spontaneous skyrmion ground states in magnetic metals”. In: *Nature* 442.7104 (2006), p. 797.
- [10] Sebastian Mühlbauer et al. “Skyrmion lattice in a chiral magnet”. In: *Science* 323.5916 (2009), pp. 915–919.
- [11] Albert Fert, Vincent Cros, and Joao Sampaio. “Skyrmions on the track”. In: *Nature nanotechnology* 8.3 (2013), p. 152.
- [12] Tony Hilton Royle Skyrme. “A unified field theory of mesons and baryons”. In: *Nuclear Physics* 31 (1962), pp. 556–569.
- [13] Toshiaki Tanigaki et al. “Real-space observation of short-period cubic lattice of skyrmions in MnGe”. In: *Nano letters* 15.8 (2015), pp. 5438–5442.
- [14] Adam S Ahmed et al. “Molecular beam epitaxy growth of [CrGe/MnGe/FeGe] superlattices: Toward artificial B20 skyrmion materials with tunable interactions”. In: *Journal of Crystal Growth* 467 (2017), pp. 38–46.

- [15] Shinichiro Seki et al. “Observation of skyrmions in a multiferroic material”. In: *Science* 336.6078 (2012), pp. 198–201.
- [16] AP Malozemoff and JC Slonczewski. *Magnetic Domain Walls in Bubble Materials: Advances in Materials and Device Research*. Vol. 1. Academic press, 2016.
- [17] T Garel and S Doniach. “Phase transitions with spontaneous modulation—the dipolar Ising ferromagnet”. In: *Physical Review B* 26.1 (1982), p. 325.
- [18] A Correspondent. “Solid State: Hard and Soft Bubbles”. In: *Nature* 240.5378 (1972), pp. 184–184.
- [19] N Nagaosa, XZ Yu, and Y Tokura. “Gauge fields in real and momentum spaces in magnets: monopoles and skyrmions”. In: *Philosophical Transactions of the Royal Society A: Mathematical, Physical and Engineering Sciences* 370.1981 (2012), pp. 5806–5819.
- [20] Xiuzhen Yu et al. “Magnetic stripes and skyrmions with helicity reversals”. In: *Proceedings of the National Academy of Sciences* 109.23 (2012), pp. 8856–8860.
- [21] S Heinze et al. “Real-space imaging of two-dimensional antiferromagnetism on the atomic scale”. In: *Science* 288.5472 (2000), pp. 1805–1808.
- [22] Niklas Romming et al. “Writing and deleting single magnetic skyrmions”. In: *Science* 341.6146 (2013), pp. 636–639.
- [23] Wang Kang et al. “Skyrmion-electronics: An overview and outlook”. In: *Proceedings of the IEEE* 104.10 (2016), pp. 2040–2061.
- [24] Shinichiro Seki and Masahito Mochizuki. *Skyrmions in magnetic materials*. Springer, 2016.
- [25] C Pappas et al. “Chiral paramagnetic skyrmion-like phase in MnSi”. In: *Physical review letters* 102.19 (2009), p. 197202.
- [26] Christian Pfleiderer et al. “Skyrmion lattices in metallic and semiconducting B20 transition metal compounds”. In: *Journal of Physics: Condensed Matter* 22.16 (2010), p. 164207.
- [27] T Adams et al. “Long-range crystalline nature of the skyrmion lattice in MnSi”. In: *Physical review letters* 107.21 (2011), p. 217206.
- [28] Akira Tonomura et al. “Real-space observation of skyrmion lattice in helimagnet MnSi thin samples”. In: *Nano letters* 12.3 (2012), pp. 1673–1677.
- [29] XZ Yu et al. “Near room-temperature formation of a skyrmion crystal in thin-films of the helimagnet FeGe”. In: *Nature materials* 10.2 (2011), p. 106.
- [30] Yukako Fujishiro et al. “Large magneto-thermopower in MnGe with topological spin texture”. In: *Nature communications* 9.1 (2018), p. 408.
- [31] Yukako Fujishiro et al. “Large magneto-thermopower in MnGe with topological spin texture”. In: *Nature communications* 9.1 (2018), p. 408.

- [32] Per Bak and M Høgh Jensen. “Theory of helical magnetic structures and phase transitions in MnSi and FeGe”. In: *Journal of Physics C: Solid State Physics* 13.31 (1980), p. L881.
- [33] Igor Dzyaloshinsky. “A thermodynamic theory of “weak” ferromagnetism of antiferromagnetics”. In: *Journal of Physics and Chemistry of Solids* 4.4 (1958), pp. 241–255.
- [34] Tôru Moriya. “Anisotropic superexchange interaction and weak ferromagnetism”. In: *Physical Review* 120.1 (1960), p. 91.
- [35] Alexei N Bogdanov and DA Yablonskii. “Thermodynamically stable “vortices” in magnetically ordered crystals. The mixed state of magnets”. In: *Zh. Eksp. Teor. Fiz* 95.1 (1989), p. 178.
- [36] Kazuo Kadowaki, Kiichi Okuda, and Muneyuki Date. “Magnetization and magnetoresistance of MnSi. I”. In: *Journal of the Physical Society of Japan* 51.8 (1982), pp. 2433–2438.
- [37] Muneyuki Date, Kiichi Okuda, and Kazuo Kadowaki. “Electron spin resonance in the itinerant-electron helical magnet MnSi”. In: *Journal of the Physical Society of Japan* 42.5 (1977), pp. 1555–1561.
- [38] S Kusaka et al. “Ultrasonic study of magnetic phase diagram of MnSi”. In: *Solid State Communications* 20.9 (1976), pp. 925–927.
- [39] XZ Yu et al. “Real-space observation of a two-dimensional skyrmion crystal”. In: *Nature* 465.7300 (2010), p. 901.
- [40] Y Onose et al. “Observation of the magnon Hall effect”. In: *Science* 329.5989 (2010), pp. 297–299.
- [41] Masahito Mochizuki et al. “Thermally driven ratchet motion of a skyrmion microcrystal and topological magnon Hall effect”. In: *Nature materials* 13.3 (2014), p. 241.
- [42] T Ideue et al. “Effect of lattice geometry on magnon Hall effect in ferromagnetic insulators”. In: *Physical Review B* 85.13 (2012), p. 134411.
- [43] Alexander Mook, Jürgen Henk, and Ingrid Mertig. “Magnon Hall effect and topology in kagome lattices: a theoretical investigation”. In: *Physical Review B* 89.13 (2014), p. 134409.
- [44] Oleg Janson et al. “The quantum nature of skyrmions and half-skyrmions in Cu₂OSeO₃”. In: *Nature communications* 5 (2014), p. 5376.
- [45] JS White et al. “Electric-field-induced skyrmion distortion and giant lattice rotation in the magnetoelectric insulator Cu₂OSeO₃”. In: *Physical review letters* 113.10 (2014), p. 107203.
- [46] Haifeng Du et al. “Edge-mediated skyrmion chain and its collective dynamics in a confined geometry”. In: *Nature communications* 6 (2015), p. 8504.

- [47] Fengshan Zheng et al. “Direct imaging of a zero-field target skyrmion and its polarity switch in a chiral magnetic nanodisk”. In: *Physical review letters* 119.19 (2017), p. 197205.
- [48] JC Gallagher et al. “Robust zero-field skyrmion formation in FeGe epitaxial thin films”. In: *Physical review letters* 118.2 (2017), p. 027201.
- [49] Y Tokunaga et al. “A new class of chiral materials hosting magnetic skyrmions beyond room temperature”. In: *Nature communications* 6 (2015), p. 7638.
- [50] K Karube et al. “Skyrmion formation in a bulk chiral magnet at zero magnetic field and above room temperature”. In: *Physical Review Materials* 1.7 (2017), p. 074405.
- [51] Xichao Zhang et al. “Magnetic skyrmion transistor: skyrmion motion in a voltage-gated nanotrack”. In: *Scientific reports* 5 (2015), p. 11369.
- [52] Xichao Zhang, Motohiko Ezawa, and Yan Zhou. “Magnetic skyrmion logic gates: conversion, duplication and merging of skyrmions”. In: *Scientific reports* 5 (2015), p. 9400.
- [53] Xichao Zhang et al. “Skyrmion-skyrmion and skyrmion-edge repulsions in skyrmion-based racetrack memory”. In: *Scientific reports* 5 (2015), p. 7643.
- [54] Riccardo Tomasello et al. “A strategy for the design of skyrmion racetrack memories”. In: *Scientific reports* 4 (2014), p. 6784.
- [55] Wang Kang et al. “Skyrmion-electronics: An overview and outlook”. In: *Proceedings of the IEEE* 104.10 (2016), pp. 2040–2061.
- [56] Senfu Zhang et al. “Current-induced magnetic skyrmions oscillator”. In: *New Journal of Physics* 17.2 (2015), p. 023061.
- [57] F Garcia-Sanchez et al. “A skyrmion-based spin-torque nano-oscillator”. In: *New Journal of Physics* 18.7 (2016), p. 075011.
- [58] G Finocchio et al. “Skyrmion based microwave detectors and harvesting”. In: *Applied Physics Letters* 107.26 (2015), p. 262401.
- [59] AR Fert. “Magnetic and transport properties of metallic multilayers”. In: *Materials Science Forum*. Vol. 59. Trans Tech Publ. 1990, pp. 439–480.
- [60] Stefan Heinze et al. “Spontaneous atomic-scale magnetic skyrmion lattice in two dimensions”. In: *Nature Physics* 7.9 (2011), p. 713.
- [61] Gong Chen et al. “Room temperature skyrmion ground state stabilized through interlayer exchange coupling”. In: *Applied Physics Letters* 106.24 (2015), p. 242404.
- [62] Olivier Boulle et al. “Room-temperature chiral magnetic skyrmions in ultrathin magnetic nanostructures”. In: *Nature nanotechnology* 11.5 (2016), p. 449.
- [63] Seonghoon Woo et al. “Observation of room-temperature magnetic skyrmions and their current-driven dynamics in ultrathin metallic ferromagnets”. In: *Nature materials* 15.5 (2016), p. 501.

- [64] Wanjun Jiang et al. “Blowing magnetic skyrmion bubbles”. In: *Science* 349.6245 (2015), pp. 283–286.
- [65] Vito Puliafito et al. “Scalable synchronization of spin-Hall oscillators in out-of-plane field”. In: *Applied Physics Letters* 109.20 (2016), p. 202402.
- [66] Abderrezak Belabbes et al. “Oxygen-enabled control of Dzyaloshinskii-Moriya Interaction in ultra-thin magnetic films”. In: *Scientific reports* 6 (2016), p. 24634.
- [67] Constance Moreau-Luchaire et al. “Additive interfacial chiral interaction in multilayers for stabilization of small individual skyrmions at room temperature”. In: *Nature nanotechnology* 11.5 (2016), p. 444.
- [68] Shawn D Pollard et al. “Observation of stable Néel skyrmions in cobalt/palladium multilayers with Lorentz transmission electron microscopy”. In: *Nature communications* 8 (2017), p. 14761.
- [69] SA Montoya et al. “Tailoring magnetic energies to form dipole skyrmions and skyrmion lattices”. In: *Physical Review B* 95.2 (2017), p. 024415.
- [70] L Sun et al. “Creating an artificial two-dimensional skyrmion crystal by nanopatterning”. In: *Physical review letters* 110.16 (2013), p. 167201.
- [71] Dustin A Gilbert et al. “Realization of ground-state artificial skyrmion lattices at room temperature”. In: *Nature communications* 6 (2015), p. 8462.
- [72] Jia Li et al. “Tailoring the topology of an artificial magnetic skyrmion”. In: *Nature communications* 5 (2014), p. 4704.
- [73] BF Miao et al. “Experimental realization of two-dimensional artificial skyrmion crystals at room temperature”. In: *Physical Review B* 90.17 (2014), p. 174411.
- [74] HZ Wu et al. “Hybrid magnetic skyrmion”. In: *Physical Review B* 95.17 (2017), p. 174416.
- [75] XZ Yu et al. “Biskyrmion states and their current-driven motion in a layered manganite”. In: *Nature communications* 5 (2014), p. 3198.
- [76] Wenhong Wang et al. “A centrosymmetric hexagonal magnet with superstable biskyrmion magnetic nanodomains in a wide temperature range of 100–340 K”. In: *Advanced Materials* 28.32 (2016), pp. 6887–6893.
- [77] Florian Jonietz et al. “Spin transfer torques in MnSi at ultralow current densities”. In: *Science* 330.6011 (2010), pp. 1648–1651.
- [78] Tomek Schulz et al. “Emergent electrodynamics of skyrmions in a chiral magnet”. In: *Nature Physics* 8.4 (2012), p. 301.
- [79] Yufan Li et al. “Robust formation of skyrmions and topological Hall effect anomaly in epitaxial thin films of MnSi”. In: *Physical review letters* 110.11 (2013), p. 117202.
- [80] SX Huang and CL Chien. “Extended skyrmion phase in epitaxial FeGe (111) thin films”. In: *Physical review letters* 108.26 (2012), p. 267201.

- [81] N Kanazawa et al. “Large topological Hall effect in a short-period helimagnet MnGe”. In: *Physical review letters* 106.15 (2011), p. 156603.
- [82] M Raju et al. “Chiral magnetic textures in Ir/Fe/Co/Pt multilayers: Evolution and topological Hall signature”. In: *arXiv preprint arXiv:1708.04084* (2017).
- [83] T Yokouchi et al. “Stability of two-dimensional skyrmions in thin films of Mn $1-x$ Fe x Si investigated by the topological Hall effect”. In: *Physical Review B* 89.6 (2014), p. 064416.
- [84] Yuan Tian, Li Ye, and Xiaofeng Jin. “Proper scaling of the anomalous Hall effect”. In: *Physical review letters* 103.8 (2009), p. 087206.
- [85] Edwin H Hall. “On a new action of the magnet on electric currents”. In: *American Journal of Mathematics* 2.3 (1879), pp. 287–292.
- [86] Minhyea Lee et al. “Hidden constant in the anomalous Hall effect of high-purity magnet MnSi”. In: *Physical Review B* 75.17 (2007), p. 172403.
- [87] A Neubauer et al. “Topological Hall effect in the A phase of MnSi”. In: *Physical review letters* 102.18 (2009), p. 186602.
- [88] Jiadong Zang et al. “Dynamics of skyrmion crystals in metallic thin films”. In: *Physical review letters* 107.13 (2011), p. 136804.
- [89] Tomek Schulz et al. “Emergent electrodynamics of skyrmions in a chiral magnet”. In: *Nature Physics* 8.4 (2012), p. 301.
- [90] Lingyao Kong and Jiadong Zang. “Dynamics of an insulating skyrmion under a temperature gradient”. In: *Physical review letters* 111.6 (2013), p. 067203.
- [91] Masahito Mochizuki et al. “Thermally driven ratchet motion of a skyrmion microcrystal and topological magnon Hall effect”. In: *Nature materials* 13.3 (2014), p. 241.
- [92] Frank Wilczek and Alfred Shapere. *Geometric phases in physics*. Vol. 5. World Scientific, 1989.
- [93] Ming-Che Chang and Qian Niu. “Berry phase, hyperorbits, and the Hofstadter spectrum: Semiclassical dynamics in magnetic Bloch bands”. In: *Physical Review B* 53.11 (1996), p. 7010.
- [94] Ganesh Sundaram and Qian Niu. “Wave-packet dynamics in slowly perturbed crystals: Gradient corrections and Berry-phase effects”. In: *Physical Review B* 59.23 (1999), p. 14915.
- [95] T Jungwirth, Qian Niu, and Allan H MacDonald. “Anomalous Hall effect in ferromagnetic semiconductors”. In: *Physical review letters* 88.20 (2002), p. 207208.
- [96] KS Denisov et al. “A nontrivial crossover in topological Hall effect regimes”. In: *Scientific reports* 7.1 (2017), p. 17204.

- [97] KS Denisov et al. “Electron scattering on a magnetic skyrmion in the non-adiabatic approximation”. In: *Physical review letters* 117.2 (2016), p. 027202.
- [98] Hiroaki Ishizuka and Naoto Nagaosa. “Spin chirality induced skew scattering and anomalous Hall effect in chiral magnets”. In: *Science advances* 4.2 (2018), eaap9962.
- [99] L Berger. “Side-jump mechanism for the Hall effect of ferromagnets”. In: *Physical Review B* 2.11 (1970), p. 4559.
- [100] SK Lyo and T Holstein. “Side-jump mechanism for ferromagnetic Hall effect”. In: *Physical Review Letters* 29.7 (1972), p. 423.
- [101] L Berger. “Application of the side-jump model to the Hall effect and Nernst effect in ferromagnets”. In: *Physical Review B* 5.5 (1972), p. 1862.
- [102] Wen-Tao Hou et al. “Thermally driven topology in chiral magnets”. In: *Physical Review B* 96.14 (2017), p. 140403.
- [103] Wenbo Wang et al. “Spin chirality fluctuation in two-dimensional ferromagnets with perpendicular magnetic anisotropy”. In: *Nature materials* (2019), pp. 1–6.
- [104] B Berg and Martin Lüscher. “Definition and statistical distributions of a topological number in the lattice O (3) σ -model”. In: *Nuclear Physics B* 190.2 (1981), pp. 412–424.
- [105] Nicholas Metropolis and Stanislaw Ulam. “The monte carlo method”. In: *Journal of the American statistical association* 44.247 (1949), pp. 335–341.
- [106] Su Do Yi et al. “Skyrmions and anomalous Hall effect in a Dzyaloshinskii-Moriya spiral magnet”. In: *Physical Review B* 80.5 (2009), p. 054416.
- [107] Stefan Buhrandt and Lars Fritz. “Skyrmion lattice phase in three-dimensional chiral magnets from Monte Carlo simulations”. In: *Physical Review B* 88.19 (2013), p. 195137.
- [108] Jung Hoon Han et al. “Skyrmion lattice in a two-dimensional chiral magnet”. In: *Physical Review B* 82.9 (2010), p. 094429.
- [109] Oleg A Starykh. “1/N expansion for the Schwinger-boson theory of quantum antiferromagnets”. In: *Physical Review B* 50.22 (1994), p. 16428.
- [110] Ribhu K Kaul and Subir Sachdev. “Quantum criticality of U (1) gauge theories with fermionic and bosonic matter in two spatial dimensions”. In: *Physical Review B* 77.15 (2008), p. 155105.
- [111] John Hubbard. “Calculation of partition functions”. In: *Physical Review Letters* 3.2 (1959), p. 77.
- [112] RL Stratonovich. “On a method of calculating quantum distribution functions”. In: *Soviet Physics Doklady*. Vol. 2. 1957, p. 416.
- [113] Assa Auerbach. *Interacting electrons and quantum magnetism*. Springer Science & Business Media, 2012.

- [114] Wolfgang Pauli and Felix Villars. “On the invariant regularization in relativistic quantum theory”. In: *Reviews of Modern Physics* 21.3 (1949), p. 434.
- [115] JD Bjorken, SD Drell, and Peter B Kahn. “Relativistic quantum fields”. In: *American Journal of Physics* 34 (1966), pp. 367–367.
- [116] Michael E Peskin. *An introduction to quantum field theory*. CRC Press, 2018.
- [117] Ryuichi Shindou and Naoto Nagaosa. “Orbital ferromagnetism and anomalous Hall effect in antiferromagnets on the distorted fcc lattice”. In: *Physical review letters* 87.11 (2001), p. 116801.
- [118] David J Thouless et al. “Quantized Hall conductance in a two-dimensional periodic potential”. In: *Physical review letters* 49.6 (1982), p. 405.
- [119] Yugui Yao et al. “First principles calculation of anomalous Hall conductivity in ferromagnetic bcc Fe”. In: *Physical review letters* 92.3 (2004), p. 037204.
- [120] Di Xiao, Ming-Che Chang, and Qian Niu. “Berry phase effects on electronic properties”. In: *Reviews of modern physics* 82.3 (2010), p. 1959.
- [121] Kun Jiang et al. “Chiral Spin Density Wave Order on the Frustrated Honeycomb and Bilayer Triangle Lattice Hubbard Model at Half-Filling”. In: *Physical review letters* 114.21 (2015), p. 216402.
- [122] CUDA Nvidia. “Nvidia cuda c programming guide”. In: *Nvidia Corporation* 120.18 (2011), p. 8.
- [123] Vladimir Privman. *Finite size scaling and numerical simulation of statistical systems*. World Scientific Singapore, 1990.
- [124] RR Heikes. “Magnetic transformation in MnBi”. In: *Physical Review* 99.2 (1955), p. 446.
- [125] JB Yang et al. “Magnetic properties of the MnBi intermetallic compound”. In: *Applied Physics Letters* 79.12 (2001), pp. 1846–1848.
- [126] Kenneth R Poeppelmeier et al. “Structure determination of CaMnO₃ and CaMnO₂ by X-ray and neutron methods”. In: *Journal of Solid State Chemistry* 45.1 (1982), pp. 71–79.
- [127] Z Zeng, Martha Greenblatt, and M Croft. “Large magnetoresistance in antiferromagnetic CaMnO_{3-δ}”. In: *Physical Review B* 59.13 (1999), p. 8784.
- [128] Satadeep Bhattacharjee, Eric Bousquet, and Philippe Ghosez. “Engineering multiferroism in CaMnO₃”. In: *Physical review letters* 102.11 (2009), p. 117602.
- [129] Christian Michel et al. “The atomic structure of BiFeO₃”. In: *Solid State Communications* 7.9 (1969), pp. 701–704.
- [130] JBNJ Wang et al. “Epitaxial BiFeO₃ multiferroic thin film heterostructures”. In: *science* 299.5613 (2003), pp. 1719–1722.

- [131] T Choi et al. “Switchable ferroelectric diode and photovoltaic effect in BiFeO₃”. In: *Science* 324.5923 (2009), pp. 63–66.
- [132] Kenji Ueda, Hitoshi Tabata, and Tomoji Kawai. “Ferromagnetism in LaFeO₃-LaCrO₃ superlattices”. In: *Science* 280.5366 (1998), pp. 1064–1066.
- [133] Jie-Xiang Yu, Morgan Daly, and Jiadong Zang. “Thermally driven topology in frustrated systems”. In: *Physical Review B* 99.10 (2019), p. 104431.
- [134] Stefan Heinze et al. “Spontaneous atomic-scale magnetic skyrmion lattice in two dimensions”. In: *Nature Physics* 7.9 (2011), p. 713.
- [135] Josef Grenz et al. “Probing the Nano-Skyrmion Lattice on Fe/Ir (111) with Magnetic Exchange Force Microscopy”. In: *Physical review letters* 119.4 (2017), p. 047205.
- [136] Alexandra Palacio-Morales et al. “Coupling of coexisting noncollinear spin states in the Fe monolayer on Re (0001)”. In: *Nano letters* 16.10 (2016), pp. 6252–6256.
- [137] Tsuyoshi Okubo, Sungki Chung, and Hikaru Kawamura. “Multiple-q states and the skyrmion lattice of the triangular-lattice Heisenberg antiferromagnet under magnetic fields”. In: *Physical review letters* 108.1 (2012), p. 017206.
- [138] AO Leonov and M Mostovoy. “Multiply periodic states and isolated skyrmions in an anisotropic frustrated magnet”. In: *Nature communications* 6 (2015), p. 8275.
- [139] AI Larkin and Yu N Ovchinnikov. “Pinning in type II superconductors”. In: *Journal of Low Temperature Physics* 34.3-4 (1979), pp. 409–428.
- [140] D Dew-Hughes. “Flux pinning mechanisms in type II superconductors”. In: *Philosophical Magazine* 30.2 (1974), pp. 293–305.
- [141] Liang Fu and Charles L Kane. “Superconducting proximity effect and Majorana fermions at the surface of a topological insulator”. In: *Physical review letters* 100.9 (2008), p. 096407.
- [142] Melvin A Ruderman and Charles Kittel. “Indirect exchange coupling of nuclear magnetic moments by conduction electrons”. In: *Physical Review* 96.1 (1954), p. 99.
- [143] Tadao Kasuya. “A theory of metallic ferro-and antiferromagnetism on Zener’s model”. In: *Progress of theoretical physics* 16.1 (1956), pp. 45–57.
- [144] Kei Yosida. “Magnetic properties of Cu-Mn alloys”. In: *Physical Review* 106.5 (1957), p. 893.
- [145] Jian Kang and Jiadong Zang. “Transport theory of metallic B 20 helimagnets”. In: *Physical Review B* 91.13 (2015), p. 134401.
- [146] Jak Chakhalian et al. “Magnetism at the interface between ferromagnetic and superconducting oxides”. In: *Nature Physics* 2.4 (2006), p. 244.

- [147] EK Dahl and A Sudbø. “Derivation of the Ginzburg-Landau equations for a ferromagnetic p-wave superconductor”. In: *Physical Review B* 75.14 (2007), p. 144504.
- [148] Andrew C Potter and Patrick A Lee. “Engineering a p+ ip superconductor: Comparison of topological insulator and Rashba spin-orbit-coupled materials”. In: *Physical Review B* 83.18 (2011), p. 184520.
- [149] Sergey S Pershoguba et al. “Currents induced by magnetic impurities in superconductors with spin-orbit coupling”. In: *Physical review letters* 115.11 (2015), p. 116602.
- [150] J Baumard et al. “Generation of a superconducting vortex via Néel skyrmions”. In: *Physical Review B* 99.1 (2019), p. 014511.
- [151] Samme M Dahir, Anatoly F Volkov, and Ilya M Eremin. “Interaction of skyrmions and pearl vortices in superconductor-chiral ferromagnet heterostructures”. In: *Physical review letters* 122.9 (2019), p. 097001.
- [152] CJ Olson Reichhardt et al. “Comparing the dynamics of skyrmions and superconducting vortices”. In: *Physica C: Superconductivity and its Applications* 503 (2014), pp. 52–57.
- [153] L Landau and E Lifshitz. “Phys. Z Sowjetunion 8, 153 (1935); TL Gilbert”. In: *Phys. Rev* 100 (1955), p. 1243.
- [154] Thomas L Gilbert. “A Lagrangian formulation of the gyromagnetic equation of the magnetization field”. In: *Phys. Rev.* 100 (1955), p. 1243.